

SYNTHESIS, CHARACTERIZATION AND PHOTOVOLTAIC PROPERTIES
OF BENZO[*c*][1,2,5]OXADIAZOLE BASED CONJUGATED POLYMERS FOR
ORGANIC SOLAR CELLS

A THESIS SUBMITTED TO
THE GRADUATE SCHOOL OF NATURAL AND APPLIED SCIENCES
OF
MIDDLE EAST TECHNICAL UNIVERSITY

BY

OĞUZHAN KARAKURT

IN PARTIAL FULFILLMENT OF THE REQUIREMENTS
FOR
THE DEGREE OF MASTER OF SCIENCE
IN
CHEMISTRY

JANUARY 2021

Approval of the thesis

**SYNTHESIS, CHARACTERIZATION AND PHOTOVOLTAIC
PROPERTIES OF BENZO[*c*][1,2,5]OXADIAZOLE BASED CONJUGATED
POLYMERS FOR ORGANIC SOLAR CELLS**

submitted by **OĞUZHAN KARAKURT** in partial fulfillment of the requirements
for the degree of **Master of Science in Chemistry, Middle East Technical
University** by,

Prof. Dr. Halil Kalıpçılar
Dean, Graduate School of **Natural and Applied Sciences** _____

Prof. Dr. Cihangir Tanyeli
Head of the Department, **Chemistry** _____

Prof. Dr. Ali Çırpan
Supervisor, **Chemistry, METU** _____

Assoc. Prof. Dr. Emrullah Görkem Günbaş
Co-Supervisor, **Chemistry, METU** _____

Examining Committee Members:

Prof. Dr. Levent Kamil Toppare
Chemistry, METU _____

Prof. Dr. Ali Çırpan
Chemistry, METU _____

Prof. Dr. Yasemin Arslan Udum
Technical Sciences Vocational School, Gazi University _____

Assoc. Prof. Dr. Salih Özçubukçu
Chemistry, METU _____

Assist. Prof. Dr. Çağatay Dengiz
Chemistry, METU _____

Date: 22.01.2021

I hereby declare that all information in this document has been obtained and presented in accordance with academic rules and ethical conduct. I also declare that, as required by these rules and conduct, I have fully cited and referenced all material and results that are not original to this work.

Name Last name :Oğuzhan Karakurt

Signature :

ABSTRACT

SYNTHESIS, CHARACTERIZATION AND PHOTOVOLTAIC PROPERTIES OF BENZO[*c*][1,2,5]OXADIAZOLE BASED CONJUGATED POLYMERS FOR ORGANIC SOLAR CELLS

Karakurt, Oğuzhan
Master of Science, Chemistry
Supervisor: Prof. Dr. Ali Çırpan
Co-Supervisor: Prof. Dr. Emrullah Görkem Günbaş

January 2021, 149 pages

In this thesis, six conjugated polymers were synthesized by coupling of 2,1,3-benzoxadiazole derivatives with donor groups via Stille polycondensation reactions. Moreover, the effect of molecular weight for P1 and P2, effect of position of alkyl chain for P5 and effect of π -bridge groups for P6 which are selenophene and thiophene on optical, electrochemical, and photovoltaic properties were investigated. Also, modifications on alkyl chains of P3 and P4 were performed to increase their functionalities via post-polymerization reactions. Electronic and optical band gaps of polymers were found as 1.83/1.81, 1.86/1.76, 2.03/1.74, 2.07/1.74, 1.76/1.72, and 2.10/1.71 respectively for P1, P2, P3, P4, P5, and P6. Furthermore, the effect of the addition of gold nanoparticles to the active layer of organic solar cells on photovoltaic properties was analyzed. Synthesized polymers were characterized by infrared (IR) spectroscopy, gel permeation chromatography (GPC), thermal gravimetric analysis (TGA), differential scanning calorimeter (DSC) and UV-Vis-NIR spectroscopy. Redox behaviors and electronic band gaps of polymers were investigated by the cyclic voltammetry (CV) method. Device production and

current/voltage property measurements were carried out in a nitrogen-filled glovebox system. While PC₇₁BM was the acceptor unit, synthesized polymers were donor units for the conventional type device structure of ITO/PEDOT:PSS/polymer:PC₇₁BM/LiF/Al. Photovoltaic properties of constructed devices were measured under 100 mW cm⁻² illumination (standard illumination of AM 1.5 G). Best device performances were found as 10.33% for P1, 6.43% for P2 and, 1.63% for P5. The optimization process is still in progress for P3, P4, and P6.

Keywords: Conjugated Polymers, Benzoxadiazole, Stille Polycondensation, Organic Photovoltaics, Power Conversion Efficiency

ÖZ

ORGANİK GÜNEŞ PİLİ UYGULAMALARI İÇİN BENZO[c][1,2,5]OKZADİYAZOL İÇEREN KONJÜGE POLİMERLERİN SENTEZİ, KARAKTERİZASYONU VE FOTOVOLTAİK ÖZELLİKLERİ

Karakurt, Oğuzhan
Yüksek Lisans, Kimya
Tez Yöneticisi: Prof. Dr. Ali Çırpan
Ortak Tez Yöneticisi: Doç. Dr. Emrullah Görkem Günbaş

Ocak 2021, 149 sayfa

Bu tezde 2,1,3-benzoksadiyazol türevlerinin donör gruplarla Stille polikondensasyon reaksiyonları ile birleştirilmesi ile altı konjuge polimer sentezlenmiştir. Buna ek olarak, P1 ve P2 için moleküler ağırlığının, P5 için alkil zincir pozisyonunun ve P6 için selenofen ve tiyofen olmak üzere π -köprü gruplarının optik, elektrokimyasal ve fotovoltaiik özellikler üzerindeki etkileri araştırılmıştır. Ayrıca, P3 ve P4'ün alkil zincirleri üzerinde modifikasyonlar, post-polimerizasyon yoluyla işlevselliklerini artırmak için gerçekleştirilmiştir. Polimerlerin elektronik ve optik bant boşlukları P1, P2, P3, P4, P5 ve P6 için sırasıyla 1,83 / 1,81, 1,86 / 1,76, 2,03 / 1,74, 2,07 / 1,74, 1,76 / 1,72 ve 2,10 / 1,71 olarak bulunmuştur. Ayrıca, organik güneş pillerinin aktif katmanına altın nano-partiküllerin eklenmesinin fotovoltaiik özellikler üzerindeki etkisi analiz edilmiştir. Sentezlenen polimerler, kızılötesi (IR) spektroskopisi, jel geçirgenlik kromatografisi (GPC), termal gravimetrik analiz (TGA), diferansiyel taramalı kalorimetre (DSC) ve UV-Vis-NIR spektroskopisi ile karakterize edilmiştir. Redox davranışları ve polimerlerin elektronik bant boşlukları döngüsel voltametri (CV) yöntemi ile incelenmiştir. Cihaz üretimi ve akım / voltaj özellik ölçümleri,

nitrojen dolu bir eldivenli kabin sisteminde gerekleřtirilmiřtir. Oluřturulan cihazlarda elektron akseptörü olarak PC₇₁BM kullanılmıř olup, elektron donörü olarak sentezlenen polimerler kullanılmıřtır. Gözeler geleneksel mimari olan ITO/PEDOT:PSS/polimer:PC₇₁BM/LiF/Al kullanılarak oluřturulmuřlardır. Oluřturulan cihazların fotovoltaiik özellikleri 100 mW cm⁻² aydınlatma altında ölçülmüřtür (AM 1.5 G standart aydınlatma). En iyi cihaz performansları P1 için %10,33, P2 için %6,43 ve P5 için %1,63 olarak bulunmuřlardır. P3, P4 ve P6 için optimizasyon süreci halen devam etmektedir.

Anahtar Kelimeler: Konjuge Polimerler, Benzokzadiyazol, Stille Polikondensasyon, Organik Fotovoltaiikler, Güç Dönüřtürme Verimlilięi

To my family and my friends...

ACKNOWLEDGMENTS

I would like to express my gratitude to Prof. Dr. Ali ırpan for his guidance and endless support. He is not only my supervisor but also a family member to me. He has always been patient and indulgent to me.

I would like to thank Assoc. Prof. Dr. Grkem Gnbař for helping me heartily when I run into problems. He always guides me to find solutions.

I would like to thank Berrin Ayyıldız, Prof. Dr. Yasemin Arslan Udum and Assist. Prof. Dr. řerife zdemir Hacıođlu for electrochemical and optical characterizations and also for sharing their valuable knowledge.

I would like to thank Glsm řahin, Eda Alemdar Yılmaz and Mertcan Erer for photovoltaic characterizations. Also, I would like to thank Glsm řahin especially for helping me heartily when I need it. She is not only a co-worker but also a special friend to me.

I would like to thank Assoc. Prof. Dr. Salih zubuku for his kindness and friendship. He is the best and coolest instructor ever.

I would like to express my gratitude to řafak Tekir and Esra Tekir. Categorize them as friends is not enough. We are a family without blood relation. Since 2015, I have shared every perfect and bad moment with them. Together we are strong.

I would like to thank Melike Erkilet for being just perfect to me. She is unique. There is no enough word in English to express my admiration and love to her.

I would like to thank Gizem Alkan Atakan and Kaan Demirel for their amazing friendship. Kaan, řafak, and I have always tremendous fun with the supreme leader Gizem Alkan Atakan. I am grateful to Gizem mommy. She is a special one among other research assistants.

I would like to express my gratitude to Sultan Taşkaya Aslan. She is the best boss ever. She always helps me with her valuable advice. She is always patient with me.

Special thank goes to my lab-mates Selin Gülmez, Ece Dikbıyık, Yeşim Abacıođlu, Berrin Ayyıldız, and co-lab-mate Osman Karaman. Their presence during long and messy experiments gave me strength and made them fun.

I owe my special thanks to my high school friends Uđur Burak Yanık, Anıl Atak, Alp Bostancıođlu, Rıdvan Kulaksız, Akın Mert Gümüş, and collage friends Ali Ozan Karabüber, Mehmet Burak Uzun, İlkey Yıldırım, Mustafa Şahin, Tansu Canbolat for their friendship and every moment that we share.

Last but not least, I would like to thank my amazing dad Hüseyin Karakurt, my amazing mother Fatma Karakurt and my amazing sister Şehrinaz Karakurt. I dedicated this thesis to them. I am the luckiest person ever because I have them. I owe everything to them.

This study is supported by the Scientific and Technological Research Council of TURKEY (TUBITAK) with project number 118Z738. I would also thank METU Central Laboratory, for TGA, DSC, HRMS, AFM and TEM analysis.

TABLE OF CONTENTS

ABSTRACT	v
ÖZ.....	vii
ACKNOWLEDGMENTS	x
TABLE OF CONTENTS	xii
LIST OF TABLES	xvii
LIST OF FIGURES	xviii
LIST OF ABBREVIATIONS	xxiii
LIST OF SYMBOLS.....	xxvi
1 INTRODUCTION.....	1
1.1 Polymer.....	1
1.2 Conjugated Polymers.....	2
1.2.1 Structures of Conjugated Polymers	2
1.2.2 Narrow-Band Gap Conjugated Polymers	3
1.3 Synthesis of Conjugated Polymers	6
1.3.1 Palladium Catalyst-Based Polymerization and Cross-Coupling Reactions	6
1.3.2 Stille Cross-Coupling Reactions.....	8
1.3.3 Mechanistic Approach to Stille Cross-Coupling Reactions	9
1.4 Characterization of Conjugated Polymers	11
1.5 Applications of Conjugated Polymers	12

1.6	Organic Photovoltaics	12
1.6.1	Working Principle of Organic Photovoltaics	13
1.7	Improvement of Efficiency of OPVs	18
1.7.1	Structural Improvements	19
1.7.2	Molecular Design of Polymeric Donor Unit	22
1.7.3	Non-fullerene Acceptors	23
1.7.4	Optimization of Active Layer Morphology	25
1.7.5	Introduction of Metal Nanoparticles	25
1.8	Literature Review	29
1.9	Aim of the Study	32
2	RESULTS and DISCUSSION	35
2.1	Design of Target Polymers	35
2.1.1	P1 and P2	35
2.1.2	P3 and P4	35
2.1.3	P5 and P6	36
2.2	Synthetic Pathways for the Synthesis of Monomers	37
2.2.1	Synthetic Pathway of M1	37
2.2.2	Synthetic Pathways of M2	39
2.2.3	Synthetic Pathways of M3 and M4	42
2.3	Synthesis of Target Conjugated Polymers	43
2.3.1	Characterization of Conjugated Polymers	43
2.4	Number Average Molecular Weight of Polymers	44
2.5	Thermal Stabilities of Polymers	44
2.6	Electrochemical Studies	45

2.7	Optical Studies	48
2.8	Photovoltaic Studies of the Polymers	52
2.8.1	P1 and P2	52
2.8.2	P3 and P4	59
2.8.3	P5	60
2.8.4	P6	66
3	EXPERIMENTAL	69
3.1	Materials	69
3.2	Methods and Experimental	69
3.3	Synthesis of Monomers	70
3.3.1	Synthesis of 1,2-dimethoxy-4,5-dinitrobenzene.....	70
3.3.2	Synthesis of 5,6-dimethoxybenzo[<i>c</i>][1,2,5]oxadiazole	71
3.3.3	Synthesis of 4,7-dibromo-5,6-dimethoxybenzo[<i>c</i>][1,2,5]oxadiazole	72
3.3.4	Synthesis of 4,7-dibromobenzo[<i>c</i>][1,2,5]oxadiazole-5,6-diol.....	73
3.3.5	Unsuccessful Trial of Synthesis of 4,7-dibromo-5,6- bis(octyloxy)benzo[<i>c</i>][1,2,5]oxadiazole	73
3.3.6	Synthesis of 1,2-bis(octyloxy)benzene.....	74
3.3.7	Synthesis of 1,2-dinitro-4,5-bis(octyloxy)benzene	75
3.3.8	Synthesis of 5,6-bis(octyloxy)benzo[<i>c</i>][1,2,5]oxadiazole.....	76
3.3.9	Synthesis of 4,7-dibromo-5,6-bis(octyloxy)benzo[<i>c</i>][1,2,5]oxadiazole 77	
3.3.10	Synthesis of tributyl(thiophen-2-yl)stannane	78
3.3.11	Synthesis of 5,6-bis(octyloxy)-4,7-di(thiophen-2- yl)benzo[<i>c</i>][1,2,5]oxadiazole.....	79

3.3.12	Synthesis of 4,7-bis(5-bromothiophen-2-yl)-5,6-bis(octyloxy)benzo[<i>c</i>][1,2,5]oxadiazole	80
3.3.13	Synthesis of 5,6-dimethoxy-4,7-di(thiophen-2-yl)benzo[<i>c</i>][1,2,5]oxadiazole	81
3.3.14	Synthesis of 4,7-bis(5-bromothiophen-2-yl)-5,6-bis(octyloxy)benzo[<i>c</i>][1,2,5]oxadiazole	82
3.3.15	Unsuccessful Trials of Synthesis of 4,7-bis(5-bromothiophen-2-yl)benzo[<i>c</i>][1,2,5]oxadiazole-5,6-diol	83
3.3.16	Synthesis of benzo[<i>c</i>][1,2,5]oxadiazole-5,6-diol	85
3.3.17	Synthesis of 5,6-bis((8-bromooctyl)oxy)benzo[<i>c</i>][1,2,5]oxadiazole	86
3.3.18	Synthesis of 4,7-dibromo-5,6-bis((8-bromooctyl)oxy)benzo[<i>c</i>][1,2,5]oxadiazole.....	87
3.3.19	Synthesis of 5,6-bis((8-bromooctyl)oxy)-4,7-di(thiophen-2-yl)benzo[<i>c</i>][1,2,5]oxadiazole	88
3.3.20	Synthesis of 5,6-bis((8-bromooctyl)oxy)-4,7-bis(5-bromothiophen-2-yl)benzo[<i>c</i>][1,2,5]oxadiazole	89
3.3.21	Synthesis of trimethyl(4-hexylthiophen-2-yl)stannane.....	90
3.3.22	Synthesis of trimethyl(4-hexylthiophen-2-yl)stannane.....	90
3.3.23	Synthesis of 4,7-bis(4-hexylthiophen-2-yl)-5,6-dimethoxybenzo[<i>c</i>][1,2,5]oxadiazole.....	91
3.3.24	Synthesis of 5,6-bis(octyloxy)-4,7-di(selenophen-2-yl)benzo[<i>c</i>][1,2,5]oxadiazole	92
3.3.25	Synthesis of 4,7-bis(5-bromo-4-hexylthiophen-2-yl)-5,6-dimethoxybenzo[<i>c</i>][1,2,5]oxadiazole.....	93
3.3.26	Synthesis of 4,7-bis(5-bromo-4-octylthiophen-2-yl)-5,6-dimethoxybenzo[<i>c</i>][1,2,5]oxadiazole.....	94

3.4	Synthesis of Polymers.....	95
3.4.1	Synthesis of P1	95
3.4.2	Synthesis of P2	96
3.4.3	Synthesis of P3	97
3.4.4	Synthesis of P4	98
3.4.5	Trials of Synthesis of P3-SH and P4-SH.....	99
3.4.6	Synthesis of P5	101
3.4.7	Synthesis of P6	102
3.5	Organic Solar Cell Device Fabrication of P1, P2, P3, P4, P5 and P6	103
3.5.1	General Procedure for Preparing Devices	103
3.5.2	Procedures for Preparing Best Devices	104
4	CONCLUSION	107
	REFERENCES	109
A.	Spectra	119

LIST OF TABLES

TABLES

Table 1.1 Performance comparisons of ternary blend OPVs at different PTB7-Th: PBDT-T ratios in terms of photovoltaic parameters	20
Table 1.2 Performance comparisons of conventional and inverted cell structure in terms of photovoltaic parameters	22
Table 1.3 Detailed photovoltaic parameters of the PBDBTF: PC ₇₁ BM and PBDBTF:IT-4F devices	24
Table 1.4 Detailed photovoltaic parameters of the PBDTTBO: PC ₇₁ BM, PBDTBO: PC ₆₁ BM, PBDTTSBO: PC ₇₁ BM and PP6DHTBT: PC ₇₁ BM devices	30
Table 1.5 Device characterization of OPVs with NPs dispersed in the photoactive layer.....	31
Table 2.1 Results of polymerizations and thermal data of polymers.....	44
Table 2.2 Detailed electrochemical properties of the polymers.....	47
Table 2.3. Optical properties of the polymers.....	50
Table 2.4 Comparison of absorption spectra of P1 and P2 with literature analogues. (Jiang et al. 2011 and Jiang et al. 2014 respectively)	51
Table 2.5 Comparison of photovoltaic properties of P1 and P2 with PBDTTBO and PBDTBO	53
Table 2.6 Summary of the photovoltaic properties for devices with ternary blend active layer	58
Table 2.7 Summary of the photovoltaic properties for devices with an inverted device structure	58
Table 2.8 Summary of the pre-photovoltaic studies for polymers P3 and P4	59
Table 2.9 Summary of the photovoltaic properties for polymer P5	61
Table 2.10 Summary of the photovoltaic properties for polymer P6	66
Table 2.11 Effect of addition of Au NPs on photovoltaic properties of P6	68

LIST OF FIGURES

FIGURES

Figure 1.1. Structures of common conjugated polymers.....	3
Figure 1.2. Structures of 2,3,1-benzoxadiazole and benzodithiophene.....	3
Figure 1.3. Structure of PffBX4T-2DT	4
Figure 1.4. Structure of PBDTFQ-TT	5
Figure 1.5. A general mechanism for Pd catalyzed cross-coupling reactions.....	7
Figure 1.6. General reaction conditions for Stille cross-coupling reactions	8
Figure 1.7. Mechanism of oxidative addition step	9
Figure 1.8. Mechanism of transmetallation step	10
Figure 1.9. Proposed mechanisms of reductive elimination step	10
Figure 1.10. The general device structure of an OPV	14
Figure 1.11. Schematic illustration of the energy conversion process of OPVs	14
Figure 1.12. General Current vs Voltage graph of an OPV	17
Figure 1.13. Detailed Current vs Voltage graph of an OPV	18
Figure 1.14. Structures of SFBRCN, PBDB-T and PTB7-Th.....	20
Figure 1.15. Device constructions of A. conventional and B. inverted solar cells .	21
Figure 1.16. Structures of PBDB-TF, PC ₇₁ BM and IT-4F.....	24
Figure 1.17. Structures of DIO, TPA and ODT	25
Figure 1.18. Representation of improved structural stability of an OPV device with NPs	26
Figure 1.19. Representation of NPs insertion to OPV device	27
Figure 1.20. Representation of thiol functionalized Au NPs.....	27
Figure 1.21. Representation of thiol modification-controlled distribution of Au NPs	28
Figure 1.22. Structures of PBDTTBO, PBDTBO, PBDTTSBO and PP6DHTBT .	29
Figure 1.23. Schematic representation of target polymers design principl	33
Figure 2.1. Synthetic pathway to obtain M1	37
Figure 2.2. Unsuccessful synthetic pathway to obtain M2	39

Figure 2.3. Successful synthetic pathway to obtain M2	41
Figure 2.4. Synthetic pathway of M3 and M4	42
Figure 2.5. Cyclic voltammograms of the polymers at 100 mV/s scan rate	45
Figure 2.6. Normalized absorption spectra of polymers in solution and solid form.....	49
Figure 2.7. Energy level diagram of P1 and P2 based OSC with conventional device architecture	52
Figure 2.8. EQE curves of organic solar cells of polymer:PC ₇₁ BM blends	54
Figure 2.9. TEM images of P1: PC ₇₁ BM (1:2, w/w) and P2: PC ₇₁ BM (1:2, w/w) blends	55
Figure 2.10. Topographic AFM images of P1: PC ₇₁ BM (1:2, w/w) and P2: PC ₇₁ BM blends	56
Figure 2.11. J-V curves of P1 and P2 for their best device performances	57
Figure 2.12. Energy level diagram of P3 and P4 based OSC with conventional device architecture	59
Figure 2.13. Energy level diagram of P5 based OSC with conventional device architecture.....	60
Figure 2.14. J-V curves that summarize the photovoltaic performance of P5	63
Figure 2.15. TEM images of P5: PC ₇₁ BM (1:2, w/w) blend	64
Figure 2.16. Topographic AFM images of P5: PC ₇₁ BM (1:2, w/w) blend.....	65
Figure 2.17. Energy level diagram of P6 based OSC with conventional device architecture.....	66
Figure 2.18. J-V curves of P6 after Au NPs treatment with different concentrations	68
Figure 3.1. Synthetic route of compound 2	70
Figure 3.2. Synthetic route of compound 3	71
Figure 3.3. Synthetic route of compound 4	72
Figure 3.4. Synthetic route of compound 5	73
Figure 3.5. Unsuccessful synthetic trial of compound 10	73
Figure 3.6. Synthetic route of compound 7	74
Figure 3.7. Synthetic route of compound 8	75

Figure 3.8. Synthetic route of compound 9	76
Figure 3.9. Synthetic route of compound 10	77
Figure 3.10. Synthetic route of compound 12	78
Figure 3.11. Synthetic route of compound 13	79
Figure 3.12. Synthetic route of compound M1	80
Figure 3.13. Synthetic route of compound 14	81
Figure 3.14. Synthetic route of compound 15	82
Figure 3.15. Unsuccessful trials to obtain product 16	83
Figure 3.16. Synthetic route of compound 17	85
Figure 3.17. Synthetic route of compound 18	86
Figure 3.18. Synthetic route of compound 20	87
Figure 3.19. Synthetic route of compound 20	88
Figure 3.20. Synthetic route of compound M2	89
Figure 3.21. Synthetic route of compound 22	90
Figure 3.22. Synthetic route of compound 24	90
Figure 3.23. Synthetic route of compound 25	91
Figure 3.24. Synthetic route of compound 26	92
Figure 3.25. Synthetic route of compound M3	93
Figure 3.26. Synthetic route of compound M4	94
Figure 3.27. Synthetic route of P1	95
Figure 3.28. Synthetic route of P2	96
Figure 3.29. Synthetic route of P3	97
Figure 3.30. Synthetic route of P4	98
Figure 3.31. Trial of synthesis of P3-SH	99
Figure 3.32. Trial of synthesis of P4-SH	100
Figure 3.33. Synthetic route of P5	101
Figure 3.34. Synthetic route of P6	102
Figure A.1. ¹ H NMR spectrum of compound 2 in CDCl ₃	119
Figure A.2. ¹³ C NMR spectrum of compound 2 in CDCl ₃	120
Figure A.3. ¹ H NMR spectrum of compound 3 in CDCl ₃	120

Figure A.4. ^{13}C NMR spectrum of compound 3 in CDCl_3	121
Figure A.5. ^1H NMR spectrum of compound 4 in CDCl_3	121
Figure A.6. ^{13}C NMR spectrum of compound 4 in CDCl_3	122
Figure A.7. ^1H NMR spectrum of compound 5 in CD_3OD	122
Figure A.8. ^{13}C NMR spectrum of compound 5 in CD_3OD	123
Figure A.9. ^1H NMR spectrum of compound 7 in CDCl_3	123
Figure A.10. ^{13}C NMR spectrum of compound 7 in CDCl_3	124
Figure A.11. ^1H NMR spectrum of compound 8 in CDCl_3	124
Figure A.12. ^{13}C NMR spectrum of compound 8 in CDCl_3	125
Figure A.13. ^1H NMR spectrum of compound 9 in CDCl_3	125
Figure A.14. ^{13}C NMR spectrum of compound 9 in CDCl_3	126
Figure A.15. ^1H NMR spectrum of compound 10 in CDCl_3	126
Figure A.16. ^{13}C NMR spectrum of compound 10 in CDCl_3	127
Figure A.17. ^1H NMR spectrum of compound 13 in CDCl_3	127
Figure A.18. ^{13}C NMR spectrum of compound 13 in CDCl_3	128
Figure A.19. ^1H NMR spectrum of compound M1 in CDCl_3	128
Figure A.20. ^{13}C NMR spectrum of compound M1 in CDCl_3	129
Figure A.21. ^1H NMR spectrum of compound 14 in CDCl_3	129
Figure A.22. ^{13}C NMR spectrum of compound 14 in CDCl_3	130
Figure A.23. ^1H NMR spectrum of compound 15 in CDCl_3	130
Figure A.24. ^{13}C NMR spectrum of compound 15 in CDCl_3	131
Figure A.25. ^1H NMR spectrum of compound 17 in $(\text{CD}_3)_2\text{CO}$	131
Figure A.26. ^{13}C NMR spectrum of compound 17 in $(\text{CD}_3)_2\text{CO}$	132
Figure A.27. ^1H NMR spectrum of compound 18 in CDCl_3	132
Figure A.28. ^{13}C NMR spectrum of compound 18 in CDCl_3	133
Figure A.29. ^1H NMR spectrum of compound 19 in CDCl_3	133
Figure A.30. ^{13}C NMR spectrum of compound 19 in CDCl_3	134
Figure A.31. ^1H NMR spectrum of compound 20 in CDCl_3	134
Figure A.32. ^{13}C NMR spectrum of compound 20 in CDCl_3	135
Figure A.33. ^1H NMR spectrum of compound M2 in CDCl_3	135

Figure A.34. ^{13}C NMR spectrum of compound M2 in CDCl_3	136
Figure A.35. ^1H NMR spectrum of compound 25 in CDCl_3	136
Figure A.36. ^{13}C NMR spectrum of compound 25 in CDCl_3	137
Figure A.37. ^1H NMR spectrum of compound 26 in CDCl_3	137
Figure A.38. ^{13}C NMR spectrum of compound 26 in CDCl_3	138
Figure A.39. ^1H NMR spectrum of compound M3 in CDCl_3	138
Figure A.40. ^{13}C NMR spectrum of compound M3 in CDCl_3	139
Figure A.41. ^1H NMR spectrum of compound M4 in CDCl_3	139
Figure A.42. ^{13}C NMR spectrum of compound M4 in CDCl_3	140
Figure A.43. HRMS spectrum of compound 2	140
Figure A.44. HRMS spectrum of compound 3	141
Figure A.45. HRMS spectrum of compound 17	141
Figure A.46. HRMS spectrum of compound 18	141
Figure A.47. HRMS spectrum of compound 19	142
Figure A.48. HRMS spectrum of compound 20	142
Figure A.49. HRMS spectrum of compound M2	142
Figure A.50. HRMS spectrum of compound 25	143
Figure A.51. HRMS spectrum of compound M3	143
Figure A.52. IR-spectrum of P1	143
Figure A.53. IR-spectrum of P2	144
Figure A.54. IR-spectrum of P3	144
Figure A.55. IR-spectrum of P4	145
Figure A.56. IR-spectrum of P5	145
Figure A.57. IR-spectrum of P6	146
Figure A.58. Themogram of P1	146
Figure A.59. Themogram of P2	147
Figure A.60. Themogram of P3	147
Figure A.61. Themogram of P4	148
Figure A.62. Themogram of P5	148
Figure A.63. Themogram of P6	149

LIST OF ABBREVIATIONS

ABBREVIATIONS

OPV	organic photovoltaic
OSC	organic solar cell
OLED	organic light emitting diodes
IPV	inorganic photovoltaic
PSC	polymer solar cell
PPV	poly(<i>p</i> -phenylene vinylene)
PPP	poly(<i>p</i> -phenylene)
PT	poly(thiophene)
PA	poly(acetylene)
PEMRG	plastic europe market research group
BO	benzoxadiazole
BDT	benzodithiophene
HOMO	highest occupied molecular orbital
LUMO	lowest unoccupied molecular orbital
D	donor
A	acceptor
PEDOT:PSS	poly(3,4-ethylenedioxythiophene)-poly(styrenesulfonate)
PCBM	[6,6]-Phenyl-C ₇₁ -butyric acid methyl ester

NFA	non-fullerene acceptor
P3HT	Poly(3-hexylthiophene-2,5-diyl)
DIO	diiodooctane
TPA	triphenylamine
ITO	indium tin oxide
LiF	lithium fluoride
ZnO	zinc oxide
BHJ	bulk heterojunction
TCO	transparent conductive oxides
HTL	hole transport layer
ETL	electron transport layer
J-V	current density vs applied voltage
SAM	self-assembled monolayer
SMW	source measurement unit
NP	nano-particle
EL	electro luminance
EQE	external quantum efficiency
NMR	nuclear magnetic resonance
TMS	trimethyl silyl
FTIR	fourier transform infrared
RID	refractive index detector
TGA	thermogravimetric analysis

DSC	differential scanning calorimeter
HRMS	high resolution mass spectrometer
PDI	polydispersity index
M _n	number average molecular weight
M _w	weight average molecular weight
GPC	gel permeation chromatography
CE	counter electrode
WE	working electrode
RE	reference electrode
CV	cyclic voltammeter
ACN	acetonitrile
<i>o</i> -DCB	<i>ortho</i> -dichlorobenzene
SCE	standard calomel electrode
PL	photoluminescence
NIR	near infrared

LIST OF SYMBOLS

SYMBOLS

δ	chemical shift
J	coupling constant
λ_{max}	maximum wavelength
$E_{\text{onset}}^{\text{ox}}$	oxidation onset potential
$E_{\text{onset}}^{\text{red}}$	reduction onset potential

CHAPTER 1

INTRODUCTION

1.1 Polymer

Greek words poly and meros which mean many parts, are ancestors of the term that we are using as polymer today. Basically, a polymer can be defined as a molecule that is formed by repeating subunits. Macromolecule is also a useful term, which refers to large molecules made up of a vast amount of covalently bonded atoms. Although all polymers are macromolecules, all macromolecules are not polymers (Jenkins et al., 1996). There are several types of polymers; natural polymers (cotton, cellulose, DNA, etc.) synthetic polymers (polyethylene, polystyrene, nylon, etc.) and semi-synthetic polymers (cellulose derivatives such as cellulose nitrate).

The rational story of polymer starts with Thomas Graham who was defined polymers as the aggregation of small molecules by unknown forces. In 1920 Hermann Staudinger was defined polymers as long chains where the atoms are connected by covalent bonding. He was awarded the Nobel Prize in 1953 “for his discoveries in the field of macromolecular chemistry”. After the 1920s polymer industry has accelerated and synthetic polymers have started to replace nature based materials. The academic community supported the development of the polymer industry with the synthesis of cheap raw material, new techniques and polymerization processes (Feldman, 2008). Karl Ziegler and Giulio Natta were awarded Nobel Prize in 1963 due to the discovery of the Ziegler-Natta catalyst. Besides the Nobel Prize, the world is achieved a powerful industry and academic research area by the discovery of the transition metal-catalyzed polymerization. That discovery has facilitated the industrial-scale production of synthetic polymers (Claverie & Schaper, 2013).

Today, polymers are used in almost all the fields of industry and demand for them is very high. Every year, more than 330 million tons of polymer are produced. (PlasticsEurope Market Research Group (PEMRG) and ConversioMarket & Strategy GmbH)

Among all the academic research fields which are related to polymers, this thesis focuses on conjugated polymers.

1.2 Conjugated Polymers

Conjugated polymers are defined as organic macromolecules that have their own delocalization along the backbone due to alternating single and double bonds (J. Liu et al., 2014) The history of conductive polymers was started with the discovery of conjugated conducting polyacetylene. Heeger, Shirakawa and MacDiarmid discovered that halogen (bromine and iodine) doped acetylene monomers conduct electricity 10 times higher than the undoped monomers (Shirakawa et al., 1977). After their discovery, undoped (neutral), and doped (charged) states of polyconjugated systems, their physical and chemical aspects became the center of attraction. These three intelligent scientists who are known as founders of conducting conjugated polymers have been awarded Nobel Prize in 2000. The perspective of scientists has changed for polymers in terms of application and research. After 1977, according to SciFinder, almost 40.000 scientific papers were published in the related fields of conjugated polymers (Harun et al., 2007).

1.2.1 Structures of Conjugated Polymers

Materials can be classified into three main groups which are insulators, semiconductors, and conductors (or metals). This differentiation comes from their ability to conduct current. Although some conductive polymers conduct electricity as well as metals like polyacetylene (Figure 1.1), they generally classify as semi-conductors (Harun et al., 2007).

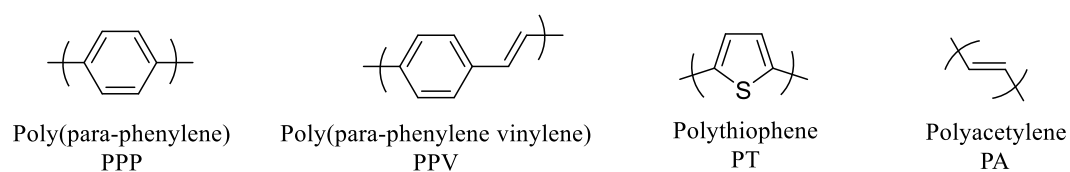


Figure 1.1. Structures of common conjugated polymers

Nowadays, conjugated polymers that have much more complex structures have been synthesized. In this master study, repeating units of synthesized polymers were selected as benzoxadiazole (BO) and benzodithiophene (BDT) (Figure 1.2) to obtain narrow-band gap polymers. Some modifications are applied to them such as the addition of alkyl groups at various locations to increase solubility. Alkyl groups are different in size and have different functional groups at the tip. Also, aromatic units are added to increase conjunction and absorption spectra (B. Liu et al., 2013). Differences that come from these modifications both electronically and morphologically were investigated.

1.2.2 Narrow-Band Gap Conjugated Polymers

Polymers which have absorption in the visible and near-infrared region are attracted by the scientific community in the field of organic photovoltaics (OPVs). Narrow-band gap polymers can satisfy this specialty (Liang et al., 2017). The strategy behind to obtain narrow-band gap polymers is polymerization of electron-deficient (acceptors) and electron-rich units (donors). Donor (D) and acceptor (A) hybridization in the polymer backbone increases the electron delocalization which will result in a decreased optical band gap. Also, this optical band gap can be manipulated by choosing different acceptor and donor units (Zhang & Wang, 2012).

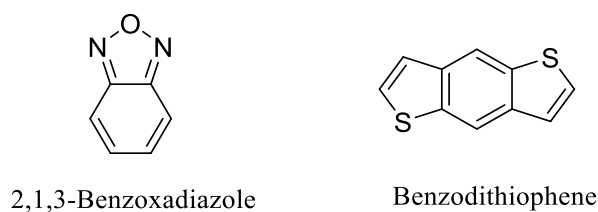


Figure 1.2. Structures of 2,3,1-benzoxadiazole and benzodithiophene

1.2.2.1 Benzoxadiazole as Acceptor Unit

Benzoxadiazole is a strong nominee as an acceptor unit for the synthesis of narrow band gap polymers for OPVs because of two key properties. The first one is strong electron-withdrawing ability due to high butadiene character and presence of electron-withdrawing atoms (Nitrogen and Oxygen). The second property is good planarity which facilitates electron delocalization (B. Liu et al., 2013). Conjugated polymers that include BO as acceptor unit are candidates to have low optical band-gap, high hole mobility, and deep HOMO levels. These three specialties can result in obtaining high fill factor (FF), open-circuit voltage (V_{oc}), and short circuit current density (J_{sc}) which are directly correlating with power conversion efficiency (PCE) of OPVs (Blouin et al., 2008). To illustrate, Yan et al. reported PCE of 9.4% with the copolymer that benzoxadiazole was used as an electron-withdrawing unit in the polymer backbone (PffBX4T-2DT, Figure 1.3) in 2015 (Zhao et al., 2016). In that period, the record was 10.3% which was achieved in 2014 (Y. Liu et al., 2014).

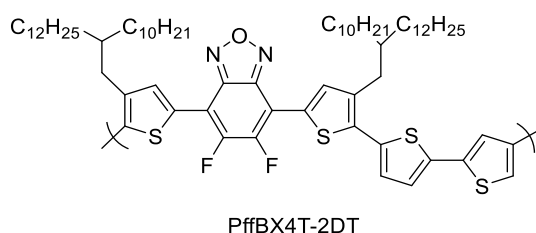


Figure 1.3. Structure of PffBX4T-2DT

1.2.2.2 Benzodithiophene as Donor Unit

Among all the donor units, BDT is one of the most studied donor units for D-A type conjugated polymers. Some properties of the BDT unit such as planarity, rigidity, favorable interchain π - π stacking, and long π -conjugation length make it a favorable electron-rich monomer. Also, the ease of introducing functional groups to BDT core provides easily functionalized polymers. To illustrate, the addition of alkyl groups can promote solubility of polymer, or the addition of aromatic groups such as

benzene, thiophane, etc... can expand plane-conjugation (Gedefaw et al., 2016). From the literature, Gedefaw et al. reported PCE of 5.60% with the copolymer that benzodithiophene core was used as an electron-acceptor unit in the polymer backbone (PBDTFQ-TT, Figure 1.4) in 2013 (Gedefaw et al., 2014).

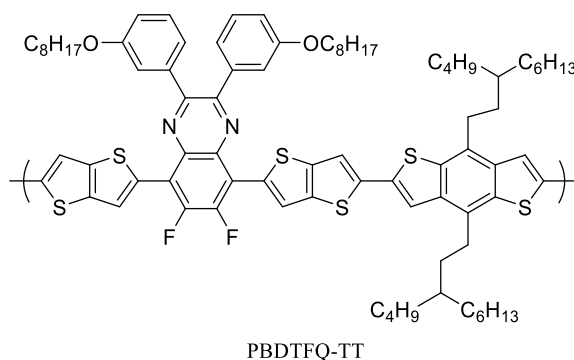


Figure 1.4. Structure of PBDTFQ-TT

1.2.2.3 Modifications Based on Aromatic and Alkyl Groups

Modifications on monomers for D-A type polymers are significantly important. One of the drawbacks of conjugated polymers is poor solubility with the increasing of polymer chain length. As known, the electronic and mechanical properties of polymers are strongly correlated with molecular weight. Polymers with smaller molecular weights could show a decrease in their electronic and mechanical properties. To prevent this, the introduction of alkyl chains with different shapes and sizes to monomers of D-A type polymers is popular. Not only solubility, but also crystallinity, interchain packing, and absorption coefficient manipulate electronic and mechanical properties and the introduction of alkyl chains regulates them (C. H. Cho et al., 2012).

Another popular modification is the addition of aromatic groups such as thiophene, selenophene, and benzene at various positions. These positions can be between monomers or on monomers as side groups. This is the most popular strategy to increase plane conjugation. Aromatic groups have the ability to regulate energy gaps,

HOMO and LUMO levels, and absorption spectra (Gedefaw et al., 2016; L. Liu et al., 2019).

1.3 Synthesis of Conjugated Polymers

Three methods are proposed for the synthesis of conjugated polymers. These are chemical oxidation polymerization, electrochemical polymerization, and transition metal-catalyzed polycondensation. Among these three polymerization methods, the transition metal-catalyzed polycondensation method comes forward with its unique features. This method results in high molecular weight, low imperfection content, and high purity. Polycondensation has been the most followed method to obtain conjugated polymers since high material quality, molecular structure and high molecular weight of conjugated polymers with enhanced electrical, optical, and mechanical properties (Heeger, 2010; J. Liu et al., 2014).

1.3.1 Palladium Catalyst-Based Polymerization and Cross-Coupling Reactions

Carbon-carbon bond formation reactions have a crucial role in chemical synthesis. Grignard, Diels Alder, Wittig and their related reactions are some of the most important examples of carbon-carbon bond formation reactions. This kind of reaction gives us the ability to synthesize complex carbon-rich compounds. After the 1975s new carbon-carbon bond formation reactions which are based on transition-metal catalysis have changed the game for organic chemists. This new way of constructing carbon-carbon bond provides new opportunities in total synthesis (Nicolaou et al., 2005).

Among these transition metal catalysts, palladium (Pd) is the most used catalyst. Pd-based catalysts are widely used in the field of conjugated polymer syntheses. They are used for both constructing monomers as a cross-coupling reaction catalyst and as a polymerization catalyst for forming a carbon-carbon bond between the monomers.

Stille, Suzuki, Heck, Sonogashira, and Negishi reactions are some of the most widely used palladium-catalyzed carbon-carbon bond constructing reactions (Nicolaou et al., 2005). General catalytic cycles for the Pd-catalyzed reactions were illustrated in the Figure 1.5. In this thesis study, the Stille cross-coupling reaction was the only method that was used to obtain monomers and polymers.

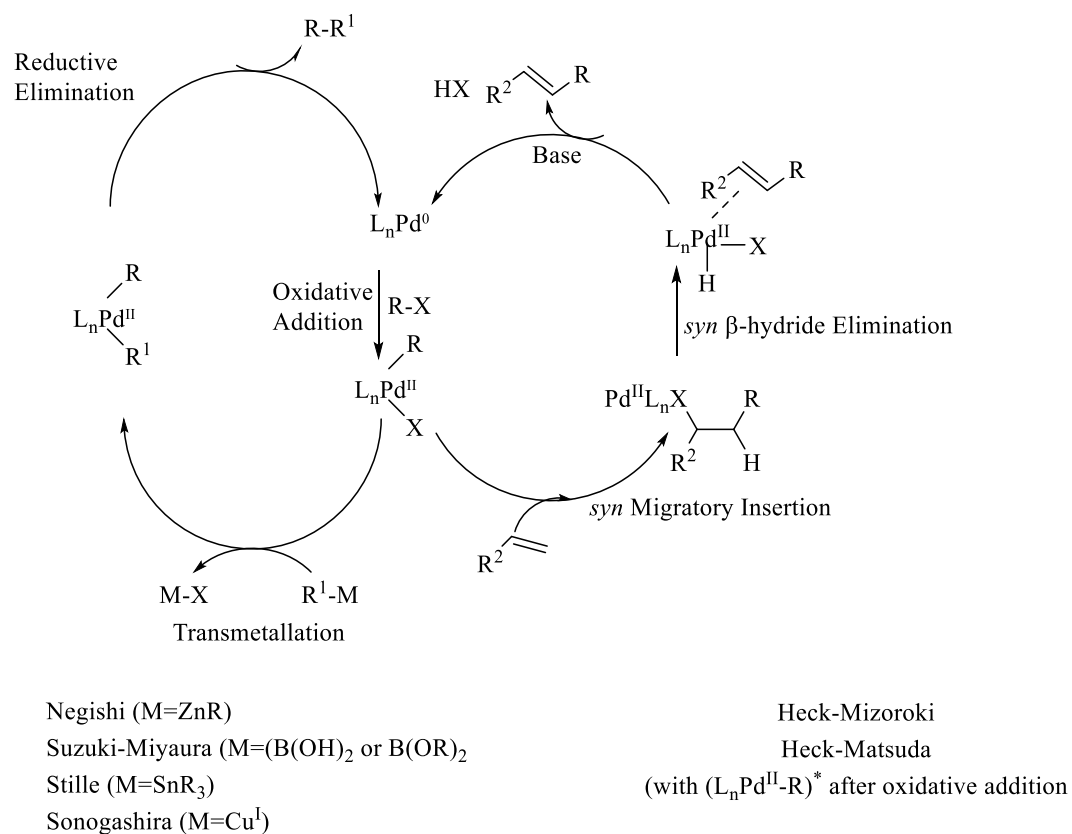
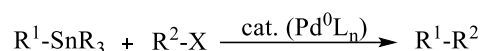


Figure 1.5. A general mechanism for Pd catalyzed cross-coupling reactions

1.3.2 Stille Cross-Coupling Reactions

Stille cross-coupling reaction, which is a strong carbon-carbon bond formation process, was developed by Prof. J. K. Stille in 1978. Stille reaction can be basically defined as cross-coupling of organotin compounds with organic electrophiles through palladium catalyst (Milstein & Stille, 1979). This reaction still one of the most used palladium-catalyzed carbon-carbon bond formation methods due to mild reaction conditions, an extensive range of coupling partners and tolerance to a wide variety of sensitive functional groups (Dunston & Pattenden, 1999). Also, Stille coupling generally gives a high yield at moderate conditions which makes it one of the favorable methods for polymerization reactions (Bao et al., 1993; Farina et al., 1997; Milstein & Stille, 1979).



R¹= alkyl, alkynyl, aryl, vinyl

R²= acyl, alkynyl, allyl, aryl, benzyl, vinyl

X= Br, Cl, OAc, OP(=O)(OR)₂, OTf

Figure 1.6. General reaction conditions for Stille cross-coupling reactions

Coupling partners of Stille coupling are organostannanes (or organotin) and organic electrophiles. As shown in the Figure 1.6, the R¹ group which was attached to the trimethyltin or tributyltin is generally sp² hybridized aryl and vinyl groups. For alkynes, Sonogashira coupling is generally preferred. Carbon groups which are sp³ hybridized usually fail or require harsh conditions (Kürti & Czakó, 2005). In organotin molecules, carbon-tin bonds are relatively stable with a bond dissociation energy of around 50 kcal/mol (Kosar et al., 2018). This relative stability allows performing a variety of reactions on other functional groups without disturbing the carbon-tin bond. Also, this relative stability makes organotin compounds air and moisture stable (Cordovilla et al., 2015). (Functional groups should also be air and moisture stable).

The other coupling partner which is an organic electrophile is typically connected with a halide such as I, Br, and or Cl also, sometimes a pseudo halide such as phosphates. Iodides and bromides generally react at moderate temperatures with organotin compounds but most of the time chlorides require electron-withdrawing groups as a substituent on the compound (Vikse et al., 2013).

1.3.3 Mechanistic Approach to Stille Cross-Coupling Reactions

Stille reaction shares common mechanistic steps with other palladium-catalyzed coupling reactions. It consists of 3 main steps which are oxidative addition, transmetallation, and reductive elimination (Espinete & Echavarren, 2004).

1.3.3.1 Oxidative Addition

The first step of the mechanism is oxidative addition. As shown in the Figure 1.7, organic electrophile binds to Pd⁰ by oxidative addition and forms cis square planar product but the trans product is thermodynamically more stable due to the presence of bulky groups as ligands on palladium. Therefore, a more stable trans product will occur in a fast equilibrium. As an alternative mechanism, the S_N2 type mechanism could take place to form a trans-intermediate (Espinete & Echavarren, 2004).

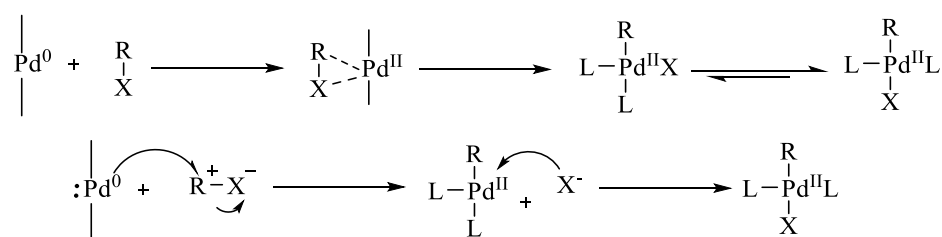


Figure 1.7. Mechanism of oxidative addition step

1.3.3.2 Transmetallation

As mentioned before, organotin compounds are used as trans coupling reagents for the Stille reaction. The R² group which is connected to tin is usually allyl, alkenyl, or aryl groups. As shown in Figure 1.8, halide containing Pd^{II} center forms a four-membered ring with the stannylated R¹ group. This results in an 18-electron transition state. R² group stays bonded to the palladium center after leaving of tin halide (Braga et al., 2013).

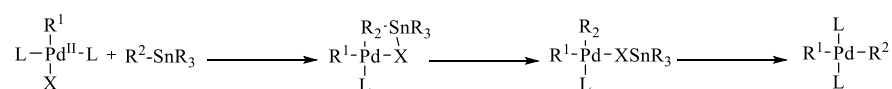


Figure 1.8. Mechanism of transmetallation step

1.3.3.3 Reductive Elimination

There are three proposed mechanisms which are illustrated in the Figure 1.9 for the reductive elimination step. The first approach is that two trans-R groups must be in trans conformation than, the complex can undergo a reductive elimination. Another approach is forming 18-electron with an extra ligand and result in trigonal-pyramidal geometry. Formation of trigonal-pyramidal structure forces R groups to move equatorial location and formation of C-C bond will be promoted. The last proposed mechanism is the formation of 14-electron containing T shape geometry. It starts with the dissociation of ligand and results in reductive elimination (Braga et al., 2013; Espinet & Echavarren, 2004).

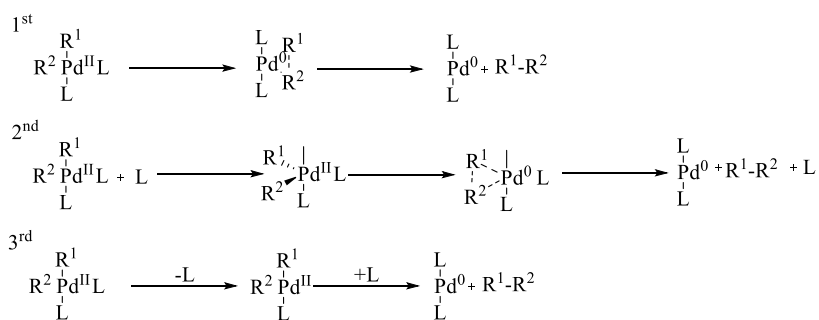


Figure 1.9. Proposed mechanisms of reductive elimination step

1.4 Characterization of Conjugated Polymers

There are several analytical techniques to characterize conjugated polymers. The list of some common techniques is:

- Gel Permeation Chromatography (GPC): It is widely used for the determination of the molecular weight of polymers. M_n , M_w , and PDI values can be obtained from this technique. Components of polymers are separated according to their weight by GPC column. Polymers (or components) move according to their size and weight. Small analytes hold on to porous gel beads and their retention time is higher than large analytes.
- Nuclear Magnetic Resonance (NMR): Due to the lack of high solubility of polymers, getting an NMR spectrum is not possible all the time. Also, NMR spectra of polymers are not clear because of peak overleaping of repeating units. Yet, NMR gives a clue about functional groups and aromatic compounds in the polymer backbone and is used for structure conformation.
- Infrared and Raman Spectroscopy: The presence of some characteristic groups on side chains of polymers can be proven by the IR spectrum. It is generally used for the determination of functional groups on polymers. It is not giving information about polymer backbone since, repeating groups cancel dipole moment of each other. Raman is used for analyzing polymer backbone structure and conformation. Since the net dipole moment does not change over the polymer backbone, polarizability could change and Raman can detect this change. IR and Raman are complementary techniques.
- Thermal Gravimetric Analysis (TGA): Thermal stability of polymers can be measured by TGA. Decomposition temperature and thermal stability can be analyzed. Also, moisture content and purity of polymer can be measured.
- UV/Vis Spectrometry (UV/Vis-NIR): The absorption spectrum of polymers as thin film and solution can be obtained from UV/Vis-NIR spectroscopy.

- **Cyclic Voltammetry:** The redox process can be analyzed by cyclic voltammetry for conjugated polymers. HOMO and LUMO levels, optical and electronic band gaps can be predicted from the cyclic voltammogram.

1.5 Applications of Conjugated Polymers

Conjugated polymers are candidates for numerous applications since the metals are toxic and hazardous to the environment. Also, some of the metals are expensive and rare. They can be replaced with cheap, non-toxic conductive conjugated polymers. Some of the application fields of conjugated polymers are corrosion protection, sensors, electromechanical devices, batteries, electrochromic cells, selective controlled and released applications, radar applications, organic light-emitting diodes (OLEDs) and organic photovoltaics (OPVs) (Harun et al., 2007). This thesis study focuses on OPVs.

1.6 Organic Photovoltaics

Renewable energy gains importance for humans and the ecological balance of the world. Fossil fuels are not endless and cause damage to the environment seriously. The world is facing new disasters like climate change where fossil fuels take their role seriously. There are many renewable energy sources and photovoltaics are one of them. Photovoltaics, especially silicon-based photovoltaics is a proven source of the production of energy with reaching 25% power conversion efficiency. Over the last few years, attention to organic solar cells (OSCs) is increasing. OSCs have many promising practical advantages over silicon-based photovoltaics (Simon et al., 2009).

High temperature is not necessary to produce an OSC which allows the usage of plastic films as substrates. Usage of plastic films results in high flexibility, thinness, and low weight. The design of an OSC has flexibility which enables different manufacturing ways. Roll-to-roll, which is a continuous manufacturing method, reduces the production cost significantly. To summarize, the key advantages of OPVs are:

- Flexible and low-weight photovoltaic modules.
- Semi-transparency.
- Integrability of various products.
- New market opportunities i.e., wearable photovoltaics.
- Lower production cost compared to conventional silicon-based photovoltaics.
- Continuous manufacturing process.
- Short energy payback response and low-level environmental hazards during production and operation.

With all these advantages, organic photovoltaics became the center of attraction for the scientific community (M. C. Scharber & Sariciftci, 2013).

1.6.1 Working Principle of Organic Photovoltaics

A conventional type OSC which is illustrated in the Figure 1.10 is usually constructed from 5 layers. Starting with an anode which is transparent and conductive (usually indium tin oxide (ITO)), followed by an interfacial layer (usually a film of poly(ethylene-dioxythiophene): polystyrenesulfonic acid (PEDOT: PSS)), then a photoactive layer which is followed by another interfacial ultrathin layer (usually lithium fluoride (LiF)) and finally a thin cathode. The composition of the photoactive layer can be small molecules or conjugated polymers. Polymers are generally applied by various techniques like spin-coating and spray-coating.

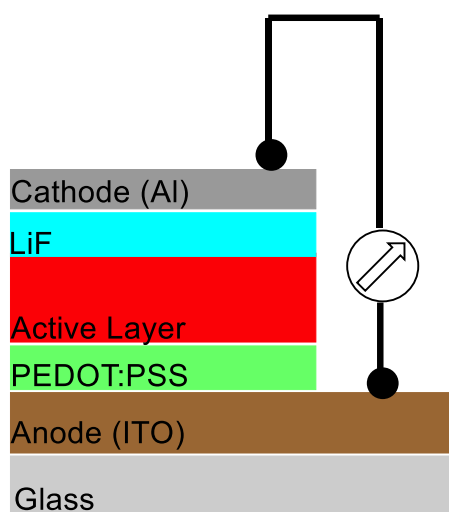


Figure 1.10. The general device structure of an OPV

In organic solar cells, the story of the conversion process begins with the creation of excitons which can define as bound electron-hole pairs. These excitons are formed by photon absorption. The binding energies of these excitons are changing in the range from 50 meV to 1 eV. To obtain free dissociated charges, excitons must diffuse. This process is called exciton dissociation (or charge separation). After the dissociation process, the charge transport step starts to finalize the energy production mechanism of an OSC. Briefly, Figure 1.11 represents the 4 steps of energy conversion process of organic photovoltaics which are absorption of light, exciton diffusion, charge separation, and charge extraction (Hafeez et al., 2018; Sekine et al., 2014).

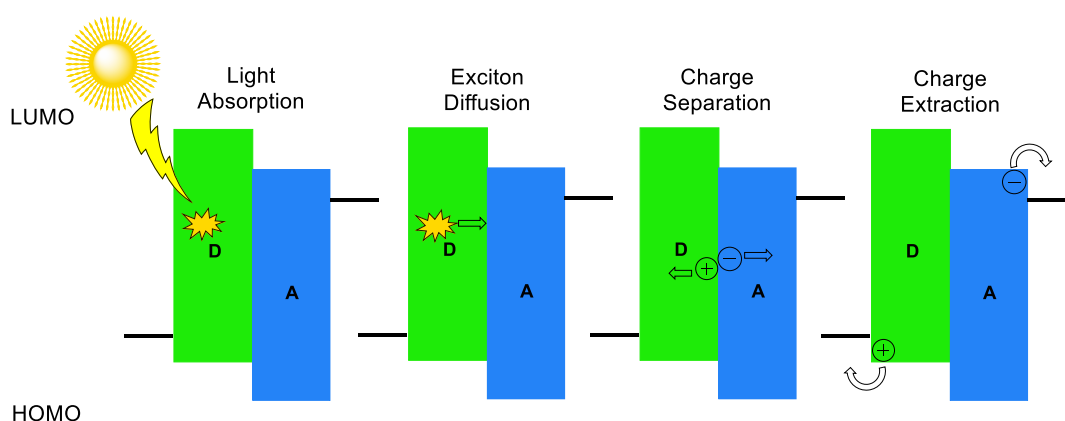


Figure 1.11. Schematic illustration of the energy conversion process of OPVs

1.6.1.1 Light Absorption

An incoming photon having energy bigger than the band gap will promote the electron from the highest occupied molecular orbital (HOMO) to the lowest unoccupied molecular orbital (LUMO) band of the donor material. The narrower band gaps provide a higher possibility of harvesting photons from solar radiation. To illustrate, silicone with a band gap of 1.1 eV can absorb 77% of incoming solar light. Organic material with a band gap of more than 2 eV can only absorb less than 30% of incoming solar light. Another important point is the thickness of the active layer. It should not be more than 150 nm because of low charge carrier mobilities. Luckily, the absorption coefficient of organic materials is superior and they are able to absorb a major part of incoming solar radiation with a thickness around 100 nm (Lin et al., 2011; Sekine et al., 2014).

1.6.1.2 Exciton Diffusion

Donor-Acceptor material interface has a local electrical field that is strong enough to separate excitons. The distance is important for an effective dissociation process. The space between the first interference and the light absorption should not exceed the exciton diffusion length (Lin et al., 2011; Sekine et al., 2014).

1.6.1.3 Charge Separation

The charge separation happens when an exciton reaches the donor-acceptor interface. The separation process occurs extremely fast with a timescale of about 45 femtoseconds. The difference between the HOMO LUMO gap of the acceptor and donor should be higher than the exciton binding energy. This is a vital requirement for effective charge separation. If this situation is satisfied, the electron transfer process to the acceptor takes place (Lin et al., 2011; Sekine et al., 2014).

1.6.1.4 Charge Extraction

The charges should reach to related device electrode to generate a voltage. Charges are not able to move freely through delocalized states like inorganic photovoltaics. Charge transportation in conjugated polymers is performed by successful hopping from one state to another state. Unfortunately, mobilities of charges in organic molecules are nominal and charges can be trapped. Charge mobilities in conjugated polymers are open to development (Lin et al., 2011; Sekine et al., 2014).

1.6.1.5 Device Engineering and Characterization of OPVs

As mentioned in the part of the working principle of an OPV, the device generally constructed from five different compartments. It can be defined as a sandwich where organic materials are placed between an anode and a cathode (electrodes). Starting with the anode part, it is a transparent oxide which is conducting. Indium Tin-Oxide (ITO) is a widely used material as an anode. The work function of ITO differs between 4.7 and 4.9 electron volt (eV) which changes according to the treatment method. Zinc Oxide (ZnO), and graphene are other examples of anode material. Not like the anode part, the cathode part is constructed from a non-transparent material. Silver (Ag), Aluminum (Al), are common examples of cathode materials. Al is generally preferred as a cathode material with a work function of 4.2 eV. To reduce the work function of cathode material, Lithium Fluoride (LiF) is commonly evaporated as an interfacial ultrathin layer at the bottom of the cathode material. The organic materials between electrodes are constructed by two different layers. One of these organic layers is a film of poly(ethylene-dioxythiophene): polystyrenesulfonic acid (PEDOT: PSS). The PEDOT: PSS is a hole transport layer, and it is coated on top of the anode to increase work function (near to 5eV). The second organic layer is named as photoactive (or active). This photoactive layer is a mixture of acceptor material such as fullerene derivatives and donor materials such as polymers, small molecules, and quantum dots. These cells can be coated on glass or plastic substrates.

The figure of the common device structure can be seen in the working principal part (Figure 1.10) (Hafeez et al., 2018).

Source measurement units (SMUs) are used to characterize the current/voltage characteristics of OPVs. SMUs scan the multiple voltage limiting levels and record responses to current values. The experiment is generally conducted under AM 1.5 illumination with an incident light power of 100 mW cm^2 . At the end of the characterization process, a current vs voltage graph is obtained for both illuminated and dark conditions (Figure 1.12) (Hafeez et al., 2018; Sekine et al., 2014).

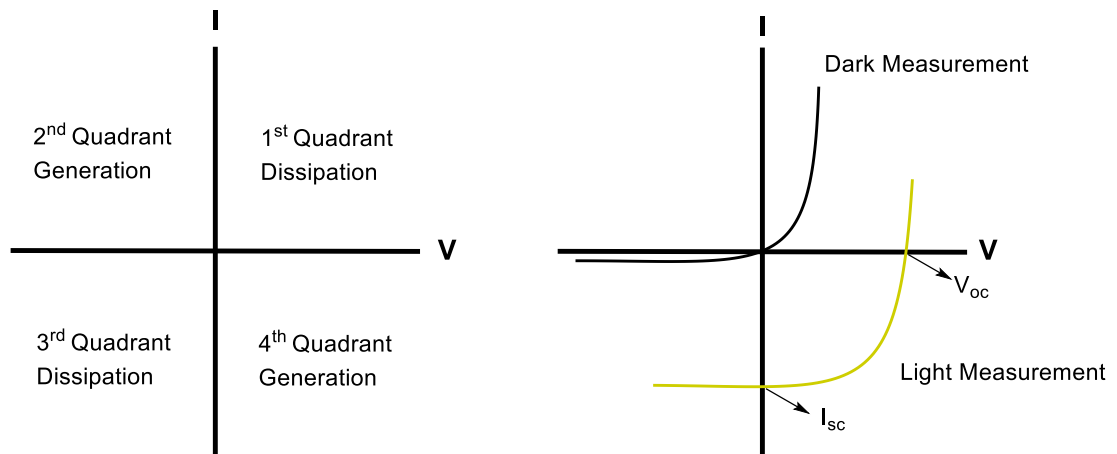


Figure 1.12. General Current vs Voltage graph of an OPV

1.7 Improvement of Efficiency of OPVs

Maximum power generation of an OPV can be calculated from the current versus voltage curve which is illustrated in Figure 1.13 in detail and the efficiency of the cell is correlated with the power generation. The mathematical formula for calculating maximum efficiency (η) is:

$$\eta = J_{sc} \times V_{oc} \times FF / P_i$$

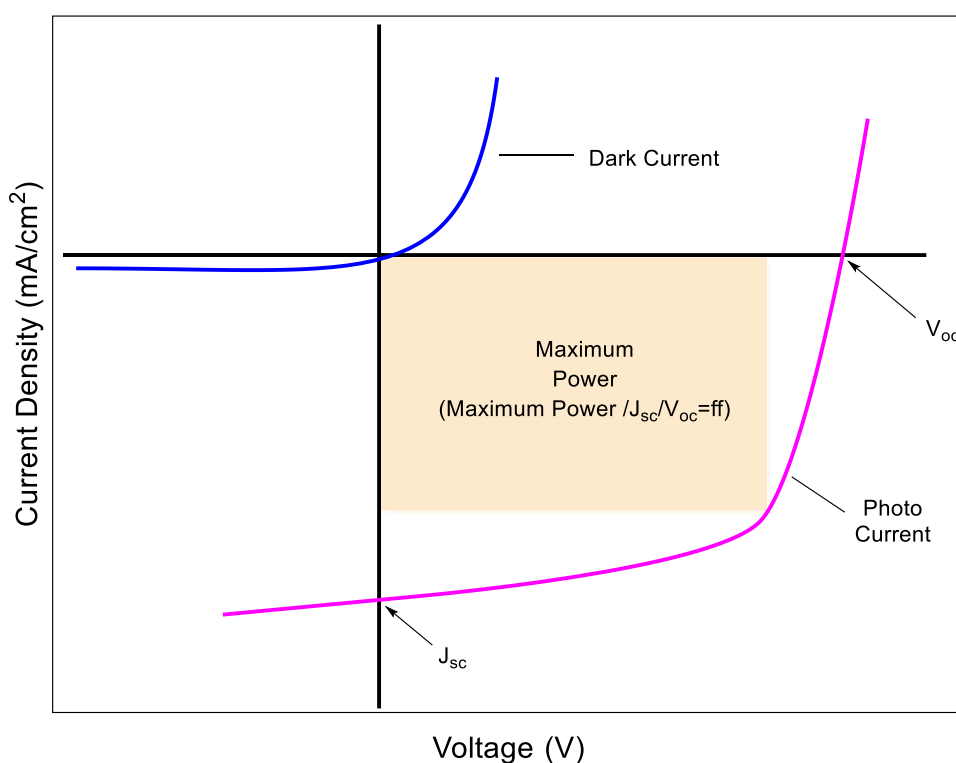


Figure 1.13. Detailed Current vs Voltage graph of an OPV

V_{oc} is the open-circuit voltage which is obtained by measuring voltage when the current density is 0 mA cm^{-2} . J_{sc} is short circuit current density and it is basically current density at 0 voltage. FF is a symbol of the fill factor which is calculated by dividing the area of the square at the current vs voltage graph by $(J_{sc} \times V_{oc})$. The last parameter P_i is input power in other words the energy of incident light. Generally, efficiency measurements are operated by a 100-mW cm^{-2} light source (Sekine et al., 2014).

From the current density versus voltage graph and mathematical formula, high values of J_{sc} , V_{oc} , and FF should be obtained in order to get high values of PCE. To summarize, high J_{sc} values can be reached by a broad light absorption spectrum. High V_{oc} value correlates with the energy band gap of donor and acceptor moieties. Lastly, FF is directly proportional to the resistance of the photovoltaic device which can be manipulated by the usage of high carrier mobility materials (M. C. Scharber & Sariciftci, 2013).

In recent years many kinds of research are being carried out to improve the J_{sc} , V_{oc} , and FF values, in other words, to increase the efficiency of organic photovoltaics. The researchers are focusing the structural improvements, optimization of active layer morphology, new molecular designs of polymeric donor units, development of non-fullerene (NF) acceptor units, and introduction of metallic nano-particle (NP) to OPVs.

1.7.1 Structural Improvements

One of the main research topics is improving morphology by developing new materials to increase the efficiency of OPVs. Also, new materials are designed to broaden the absorption spectrum which is also directly correlating with the efficiency. Light absorption is important for OPVs because unlike inorganic photovoltaics (IPVs), light absorption in OPVs results in the generation of excitons which are also known as excited bound electron-hole pairs. (Simon, André, & Lehn, 1985). The very basic technique to boost the absorption is increasing the diameter of the active layer, but this diameter is normally limited (<150 nm) by the restrained charge carrier mobility. (Simon et al., 2009). An alternative to broadening the light absorption spectrum without increasing the physical thickness is light guiding systems. When the light travels longer in the active layer, more photons are absorbed and this will result in higher efficiency (Uddin et al., 2010).

Another useful approach for structural improvement is constructing the photoactive layer of OPVs by ternary blend with one acceptor and two donor materials. This strategy can be applied for single active layer devices without the creation of more complexity like tandem cells. Two donor materials in the photoactive layer with different absorption spectra provide desirable incoming light absorption. This method comes forward as an effective way to overcome absorption bottleneck hence it becomes a good candidate to achieve better device performance (Lu et al., 2014). As an example for the performance upgrade of a device after constructing with ternary blend instead of binary, an illustrative comparison from literature is given below (Figure 1.14, Table 1.1) (Xu et al., 2017);

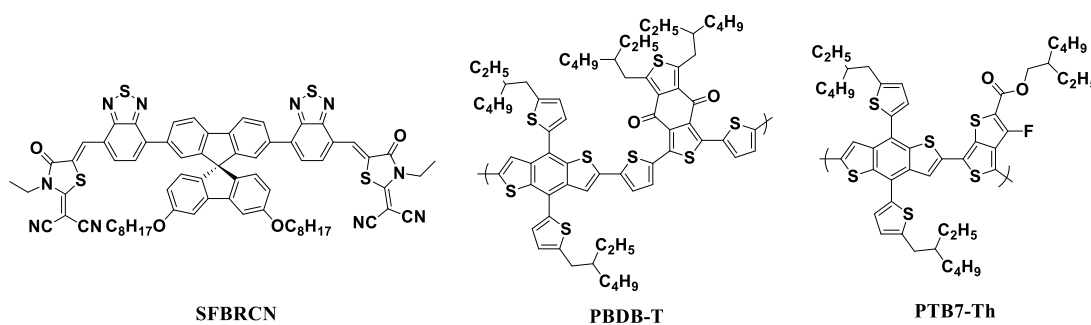


Figure 1.14. Structures of SFBRCN, PBDB-T and PTB7-Th

Table 1.1 Performance comparisons of ternary blend OPVs at different PTB7-Th: PBDB-T ratios in terms of photovoltaic parameters

Ternary Blends	Ratio (PTB7-Th: PBDB-T)	V_{oc} (V)	J_{sc} (mA cm^{-2})	FF (%)	$\text{PCE}_{\text{average}}$ (%)
Fixed the Ratio of	0.0:1.0	0.97	13.65	70.9	9.17
SFBRCN:Polymer	0.7:0.3	0.93	17.86	73.9	11.89
	1.0:0.8	0.91	17.11	64.9	9.87

Inverted device architecture is another example of structural improvements. Briefly, in this type of device architecture removal of PEDOT:PSS layer from ITO interference and metals with high work function at the top of the device is needed.

Inverted device architecture which is illustrated in the Figure 1.15 can be a good opponent of conventional device structure and gained attention from researchers due to its superior device stability and efficiency. Metals with higher work functions such as Ag and Au which are more air-resistant as top electrodes can be used in this inverted architecture since the direction of charge collection is opposite (Hau et al., 2010; Yang et al., 2012). LiF/Al layer of the conventional device is extremely unstable under Air exposure. Hau et. al. confirmed that the loss of PCE of the device is more than half of original PCE value after just 1 day and it completely degraded after 4 days due to oxidation of aluminum where inverted cells just lost 20% percent of their original value of PCE after 40 days (Hau et al., 2010). In another research, better PCE values were reached by an inverted device structure than a conventional device structure. The same polymeric material was used and efficiency was improved from 8.70 % to 10.10 % (Table 1.2). They conclude that a highly ordered crystalline polymer film structure with shorter π - π stacking distances was the major reason for that efficiency increase. They have found that the face-on orientation of polymeric donor material is more abundant on the surface on ZnO than PEDOT:PSS surface which was proposed as the major reason for increasing charge transport and decreasing charge recombination (Vohra et al., 2015).

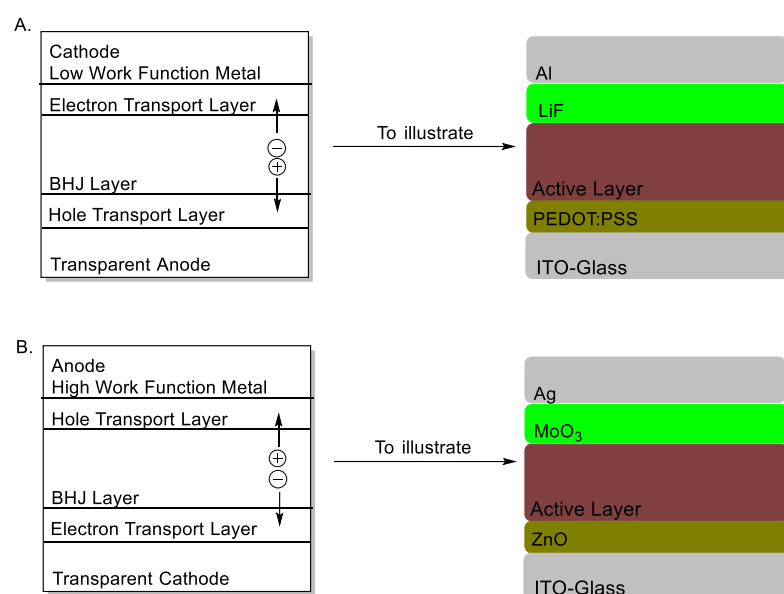


Figure 1.15. Device constructions of A. conventional and B. inverted solar cells

Table 1.2 Performance comparisons of conventional and inverted cell structure in terms of photovoltaic parameters

Cell structure	PCBM	J_{sc} (mA cm ⁻²)	V_{oc} (V)	FF (%)	PCE _{max} (%)
Conventional	PC ₆₁ BM	17.7	0.738	66.7	8.70
	PC ₇₁ BM	18.9	0.712	66.2	8.92
Inverted	PC ₆₁ BM	18.2	0.729	73.9	9.80
	PC ₇₁ BM	19.4	0.708	73.4	10.1

1.7.2 Molecular Design of Polymeric Donor Unit

The photoactive layer is one of the most vital components for an OPV. This layer plays a decisive role in the final performance of OPVs. Standard components of a bulk heterojunction (BHJ) active layer are conjugated polymers and fullerene derivatives (most recently non-fullerene derivatives are present). These components are acting as electron donor and acceptor units. While conjugated polymers acting like electron donors, fullerene (or non-fullerene) derivatives acting like electron acceptors (Gedefaw et al., 2014).

An optimum polymeric donor unit must have the following specialties:

- The donor units' frontier molecular orbitals should have appropriate energy that matching with the corresponding acceptor unit (Markus C. Scharber et al., 2006).
- It should form a good film and mix well with corresponding acceptor moiety (Beaujuge et al., 2009).
- It should have a high absorption coefficient value with a wide absorption spectrum (Yue et al., 2013).
- Hole mobility should be good (Yu et al., 2015).

To satisfy the conditions to obtain the optimum polymeric donor unit, a good strategy is forming the polymer backbone with alternating electron acceptor and electron donor groups. The idea behind this formation is creating a push and pull architecture. Also, placing a π -bridging group like selenophene, thiophene between electron acceptor and electron donor groups is a common strategy to manipulate optical and electronic properties. These π -bridging groups contribute to the electronic interaction between push and pull groups and increase the π -electron density. The structural conformation of the polymer is also affected by the π -bridging groups that increase the rigidity and planarity. Since it is known that, planarity and rigidity favors the electron delocalization along the polymer backbone (Lei et al., 2012; Sun et al., 2012)

To summarize, many different strategies are applied to have a proper polymeric donor unit. A variety of π -bridging groups have been synthesized to increase rigidity and enhance absorption spectra. New conjugate aromatic rings with electronegative heteroatoms are investigated to obtain good acceptor moieties and similarly, fused electron-rich aromatic donor units are investigated to obtain good electron donor moieties.

1.7.3 Non-fullerene Acceptors

Another major research field for improving the efficiency of OPVs is developing new non-fullerene acceptor units. Fullerene derivatives are unique due to their conjugated ball-like structure and they have been used for almost 20 years. Fullerene derivatives are promising strong electron-accepting and electron transporting features. Also, they provide efficient electron delocalization at the DONOR: ACCEPTOR (D: A) interferences (Gélinas et al., 2014). NF acceptors usually resulted in low power conversion efficiency (PCE) which correlated with difficulties in morphological control until 2015 (Hou et al., 2018). After 2015, NF acceptors are attracted much more by the scientific community, and the development of NF acceptors started to accelerate. Recently developed NF acceptors provide low

voltage losses and high photocurrent at the same time while fullerene-based acceptors presenting a trade-off between high photovoltage and photocurrent. To illustrate, the PCE of NF OPVs was found 13.1% in 2017 (W. Zhao et al., 2017) which was higher than the best fullerene-based OPVs. (Hou et al., 2018). Although many challenges still present for NF-acceptors such as inexplicit working mechanisms, many research groups work on synthetic route and material design to develop NF acceptors and try to unravel challenges.

To illustrate the performance difference between fullerene and non-fullerene acceptor, a good comparison of PC₇₁BM and IT-4F (Figure 1.16) from literature gathered in Table 1.3 (Cui et al., 2019);

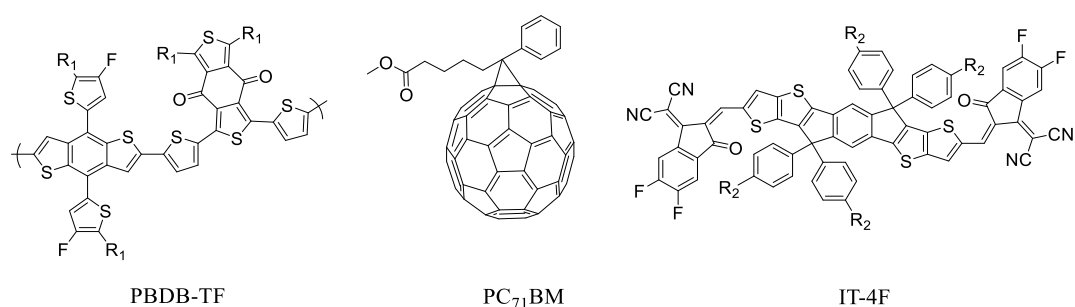


Figure 1.16. Structures of PBDB-TF, PC₇₁BM and IT-4F

Table 1.3 Detailed photovoltaic parameters of the PBDBTF: PC₇₁BM and PBDB-TF:IT-4F devices

Device	V _{oc} (V)	J _{sc} (mA cm ⁻²)	J _{sc} ^a (mA cm ⁻²)	FF (%)	PCE (%)
PBDBTF:PC ₇₁ BM	0.945	13.3	12.9	0.671	8.43
PBDB-TF:IT-4F	0.872	20.4	20.1	0.687	12.2

^a Calculated by EQE curve.

1.7.4 Optimization of Active Layer Morphology

Optimization of the active layer is also taking an important place for device performance. Not only designing new molecules but also solvent selection, solvent annealing processes and small molecular weight additives get attention from the scientific community. Basically, additives are used for morphology control. Single solvent usage often results in phase separation between the bulk heterojunction blend (BHJ) components which will disturb the order within domains and results in lower efficiency of the device (McDowell et al., 2018). Up to now, 1,8-diiodooctane (DIO) triphenylamine (TPA) and octanedithiol (ODT) which the structures are showed in the Figure 1.17 are some of the most used additives to optimize the active layer (Rodrigues et al., 2014).

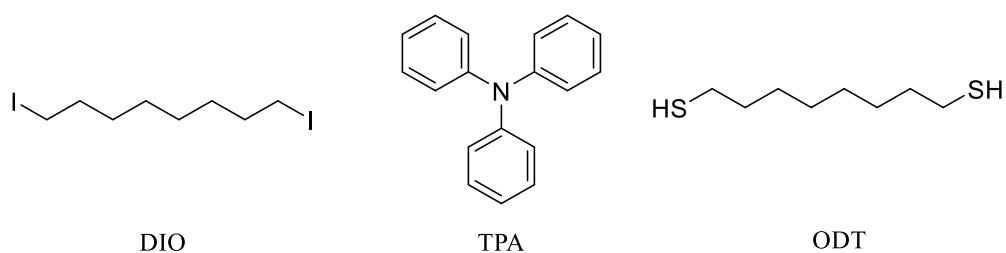


Figure 1.17. Structures of DIO, TPA and ODT

1.7.5 Introduction of Metal Nanoparticles

As mentioned in the structural improvement part, the collection of photogenerated excitons and light absorption has vital importance to achieve high PCE OPVs. Since the thickness of the active layer of OPVs is small, they absorb light poorly. This limited thickness has remained a challenge for scientists. Another research field to overcome this problem is trapping of incident light in the active layer which can be achieved by using nano-particles (Stratakis & Kymakis, 2013). Utilization of nano-particles either inside active layers or the buffer or between interfaces of OPV devices can promote absorption thus, light-harvesting is promoted by the increasing optical thickness of OPV materials (Atwater & Polman, 2010).

Another feature of using NPs is improving structural stability. They slow down the device degradation which is represented in the Figure 1.18 rate upon extensive illumination (Paci et al., 2011). Overall, utilization of NPs in the active layer of OPVs can improve the device performance in two ways which are enhancement of initial cell efficiency with a light-harvesting effect and better device durability due to improved structural stability.

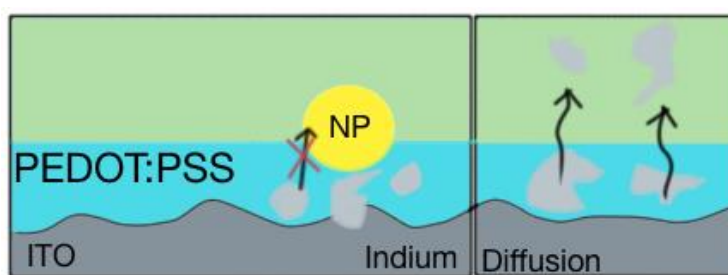


Figure 1.18. Representation of improved structural stability of an OPV device with NPs

1.7.5.1 Insertion Process of NPs

It is confirmed that with the direct addition of metal NPs to a bulk heterojunction polymer, the efficiency was improved due to better electrical conductivity (Kim & Carroll, 2005). Since it improves the overall performance of the device, a simple method of mixing metal NPs in the active layer which is illustrated in the Figure 1.19 is inviting. The device resistance can be reduced by this method (Kim & Carroll, 2005). The reflection and scattering of incident light which passes through the active layer can be provided by the accommodated metal NPs. This will result in an increase in the optical path length of the incident light (Wang et al., 2011). Although NP addition to the active layer is proved as an effective method, there is no literature work to control the distribution of NPs in an active layer of OPVs.

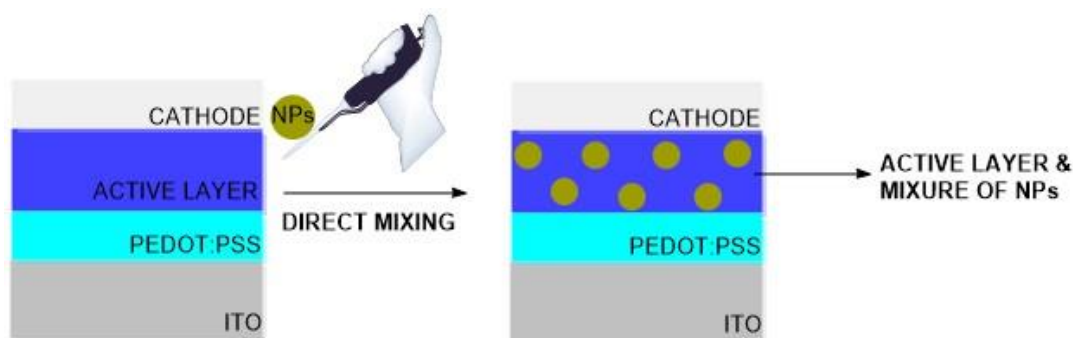


Figure 1.19. Representation of NPs insertion to OPV device

1.7.5.2 Gold NPs-Thiol Interaction

Self-assembled thiols on gold surfaces are one of the most interesting topics as self-assembling of organic molecules on metal surfaces. The assembling process based on thiol-gold NP chemistry is widely used in various fields such as chemistry, molecular biology, and materials science (Xue et al., 2014). The most entirely investigated phenomenon for Au-S binding is the generation of self-assembled monolayers (SAMs) on gold NPs and planar gold surfaces (Kind et al., 1999).

The bond length of gold monosulfide (AuS) and dissociation energy was determined as 2.156 \AA and $298 \pm 2 \text{ kJ/mol}$ respectively (Kokkin et al., 2015). Literature research of Au-S binding shows that this interaction has the potential to be used for nanoparticle-based OPVs as a regulator for the distribution of gold NPs in the active layer.

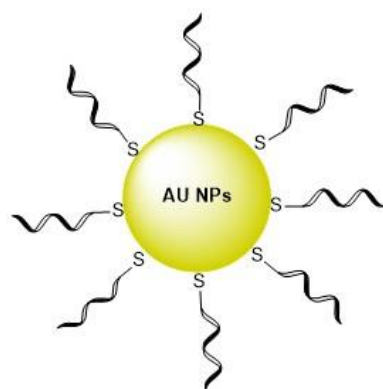


Figure 1.20. Representation of thiol functionalized Au NPs

1.7.5.3 Controlled Distribution of NPs

In other disciplines of science such as biochemistry, gold NPs-thiol interactions have been used (Boisselier & Astruc, 2009). It is believed that such interaction can be adopted in the field of OPVs as a controlling agent of the distribution of gold NPs in the active layer of devices. Also, it is believed that the regular distribution of NPs will enhance the effectiveness of the usage of NPs with better light-harvesting capability and improved structural stability.

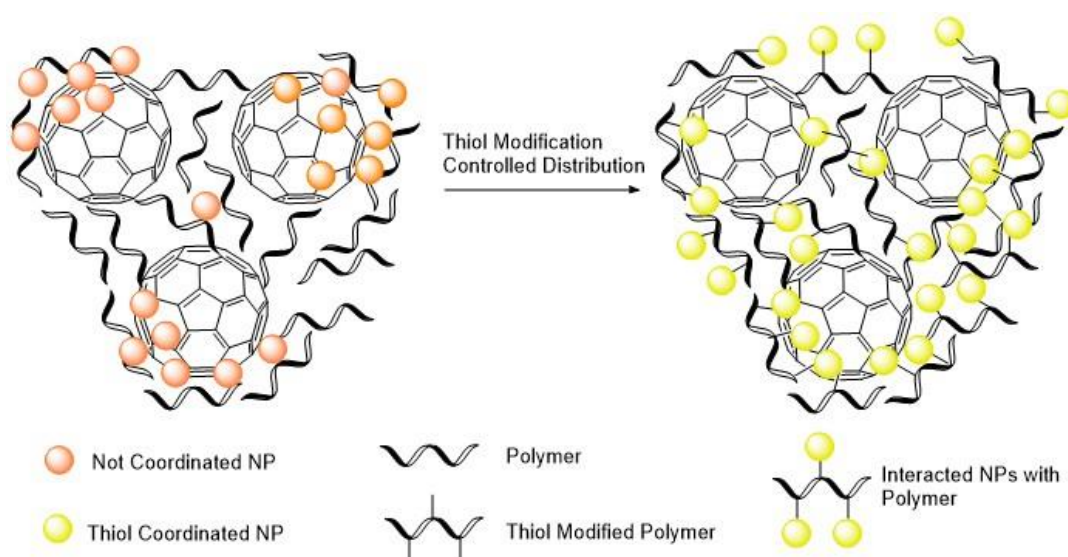


Figure 1.21. Representation of thiol modification-controlled distribution of Au NPs

1.8 Literature Review

The idea behind this thesis study was supported by various papers from the literature. The literature search is mainly focused on polymeric donor units and the effect of NPs on the photoactive layer of OPVs.

Six different polymeric donor units for the photoactive layer of OPVs were synthesized in this thesis study. Two of the synthesized polymers (P1 and P2) were already present in the literature. Although they were synthesized before, their potential is promise constructing better devices with different approaches like synthesizing the same polymer with higher molecular weight or constructing ternary blend OPVs as one of the two donor material. The remaining four polymers were new in the literature. They have similar donor and acceptor repeating units in the polymer backbone with major modifications like the different location of the alkyl chain or different π -bridging between donor and acceptor groups. Figure 1.22 shows structures of PBDTTBO, PBDTBO, PBDTTSBO and PP6DHTBT and Table 1.4 summarizes the device performances in which the inspired similar polymers were used as polymeric donor unit in the photoactive layer.

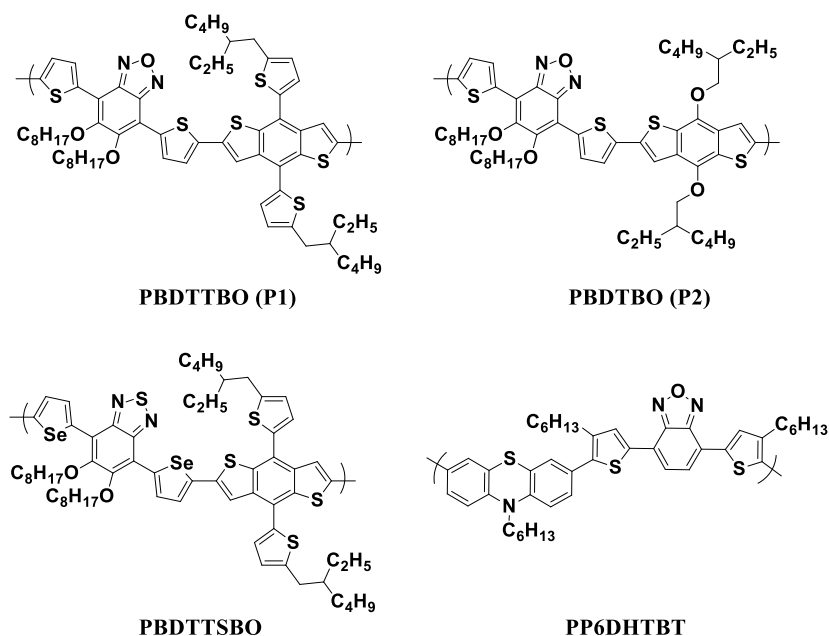


Figure 1.22. Structures of PBDTTBO, PBDTBO, PBDTTSBO and PP6DHTBT

Table 1.4 Detailed photovoltaic parameters of the PBDTTBO: PC₇₁BM, PBDTBO: PC₆₁BM, PBDTTSBO: PC₇₁BM and PP6DHTBT: PC₇₁BM devices

Polymer	Device	V _{oc} (V)	J _{sc} (mAcm ⁻²)	FF (%)	PCE _{average} (%)	Reference
PBDTTBO	Polymer: PC ₇₁ BM (1:2)	0.85	11.8	59.0	5.9	(Jiang et al., 2014)
	Polymer: PC ₇₁ BM (1:1.5)	0.84	11.45	61.3	5.9	(B.Liu et al.,2013)
PBDTBO	Polymer: PC ₆₁ BM (1:1)	0.86	10.4	64.4	5.7	(Jiang et al., 2011)
PBDTTSBO	Polymer: PC ₇₁ BM (1:2)	0.79	11.9	50	4.61	(Jiang et al., 2014)
PP6DHTBT	Polymer: PC ₇₁ BM (1:4)	0.75	4.60	35.0	1.20	(Matsumura et al., 2008)

The literature search for the effect of nano-particles was specialized to the dispersion process of NPs into the photoactive layer and the contribution of NPs to PCE of OPVs. To summarize the literature search, Table 1.5 was constructed by the information taken from a review paper ‘‘Nano-particle based plasmonic organic photovoltaic devices’’ (Stratakis & Kymakis, 2013).

Table 1.5 Device characterization of OPVs with NPs dispersed in the photoactive layer

Geometry	Photoactive Layer	η (%)	\pm (%)	Mechanism	Reference
70 nm Ag NPs	PCDTBT:PC ₇₀ BM	7.1	13	Scattering	(Wang et al., 2011)
4.8-7.4 nm Au NPs	P3OT-C ₆₀	1.9	73	Electrical	(Kim & Carroll, 2005)
4.2-6.4 nm Ag NPs		1.65	50		
3.7 nm Au NPs	P3HT:PCBM	1.5	-67	Exciton Quenching	(Shen et al., 2009)
20 nm Ag NPs	P3HT:PCBM	2.06	96	LSPR + Morphology	(Paci et al., 2011)
5-15 nm Ag NPs	P3HT:PCBM	3.3	-3	Monomolecular Recombination	(Xue et al., 2011)
1.5-20 nm Au NPs	P3HT:PCBM	3.71	41	LSPR + Scattering + Morphology	(Spyropoulos et al., 2012)

From the Table 1.5, one can understand, the various mechanisms can take place. Although NPs dispersion in the photoactive layer generally results in a mechanism that increasing efficiency, it is obvious that some type of mechanisms leads to low efficiency. Size, shape and surfactants (NPs stabilizers) of NPs are possible candidates to manipulate the mechanism. Also, the structures of the acceptor and donor unit can be decisive. Although the same polymeric donor unit (P3HT) and acceptor unit (PCBM) were used repeatedly, the results and mechanisms are not consistent. Therefore, the importance of the size, shape, and followed method for the synthesis of NPs come forward as a decisive parameter of the working mechanism.

1.9 Aim of the Study

The absorption spectra of conjugated polymers in the visible and near-infrared region can be enhanced by narrowing the optical band gap. The strategy behind to obtain narrow-band gap polymers is polymerizations of electron-deficient units (acceptors) and electron-rich (donors). Donor and acceptor hybridization in the polymer backbone could increase the electron delocalization which could result in decreasing optical band-gap. Benzoxadiazole is a strong nominee as an acceptor unit due to two properties which are strong electron-withdrawing ability and good planarity in the synthesis of narrow band gap polymers for organic photovoltaics. Furthermore, conjugated polymers that include benzoxadiazole as acceptor units are candidates to have low optical band-gap, high hole mobility, and deep HOMO levels. These three specialties could result in obtaining high fill factor, open-circuit voltage, and short circuit current density which is directly correlated with the power conversion efficiency of organic photovoltaics. In this thesis, six conjugated polymers were designed and synthesized by coupling of 2,1,3-benzoxadiazole derivatives with donor groups via Stille polycondensation reactions.

The first pair out of six polymers were already present in the literature, they were re-synthesized according to the TUBITAK project to compare their device performances with the modified versions of them (P3-SH and P4-SH). The second pair out of six polymers were constructed on examination of the effect of the π -bridge group between acceptor and donor units and position of alkyl chain since, π -bridge groups have the ability to regulate energy gaps, HOMO and LUMO levels, and absorption spectra of conjugated polymers and position of alkyl chains can manipulate crystallinity, interchain packing, and absorption coefficient which have the ability to change electronic and mechanical properties of conjugated polymers. The last pair out of six conjugated polymers were designed to increase their functionality via further post-polymerizations for various applications. Also, the functional group of these conjugated polymers was planned to replace with the thiol group in order to activate with gold NPs to increase absorption spectra of organic

photovoltaics. The designed and synthesized conjugated polymers **P1**, **P2**, **P3**, **P4**, **P5** and **P6** were used for the construction of organic photovoltaics with conventional device architecture as polymeric donor units. In addition to that inverted device architecture and ternary blend, approaches were studied with **P1** and **P2**. All in all, designed six conjugated polymers were synthesized, characterized and mechanical-electronic properties were investigated. Also, with these six conjugated polymers, OSCs were fabricated and studied to reach maximum efficiencies.

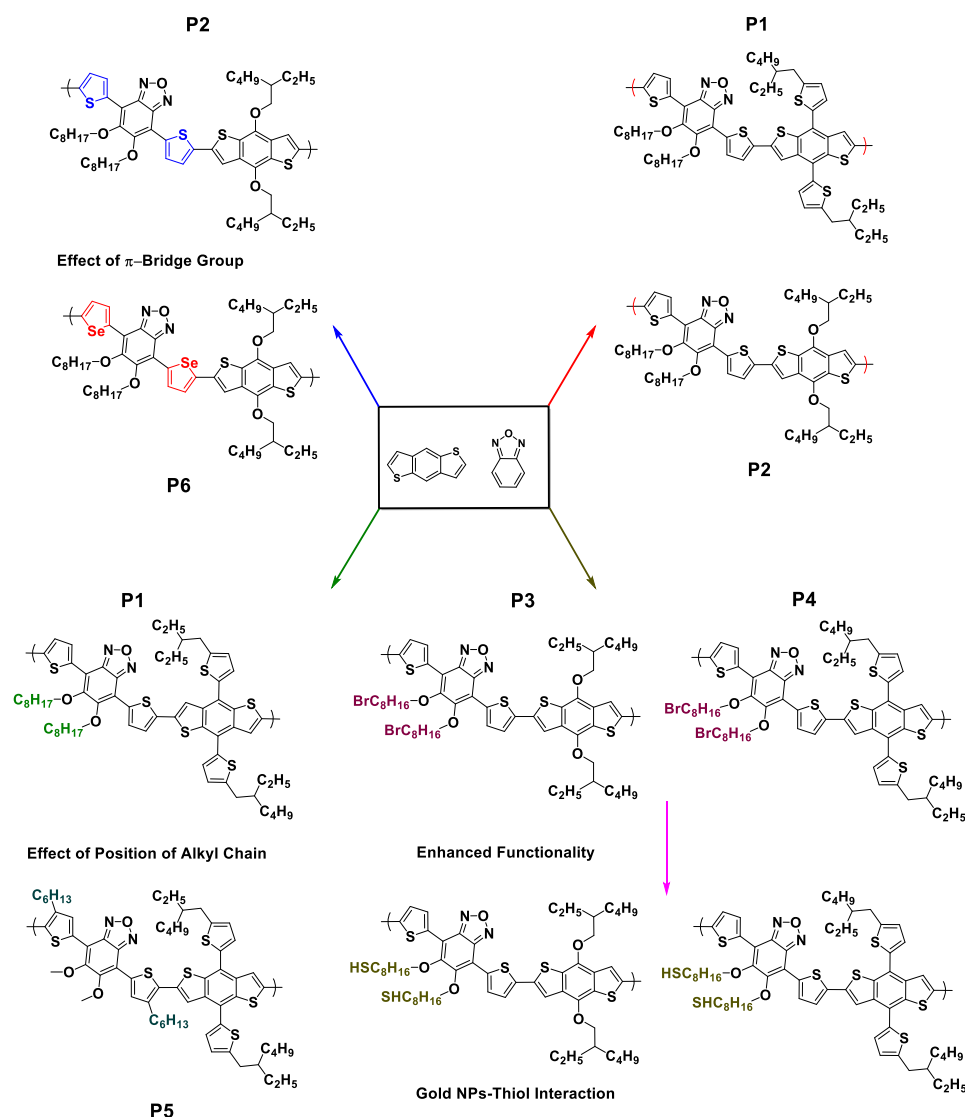


Figure 1.23. Schematic representation of target polymers design principle

CHAPTER 2

RESULTS and DISCUSSION

2.1 Design of Target Polymers

2.1.1 P1 and P2

Two conjugated polymers PBDTTBO and PBDTBO (Jiang et al., 2014; Jiang et al., 2011) were already present in the literature, they were re-synthesized during to course of TUBITAK project to compare their device performances with the modified versions of them (P3-SH and P4-SH). Nowadays, formerly synthesized polymers are considered moderately efficient polymers for organic solar cells (5.9% and 5.7% PCE respectively). Newly synthesized polymers which were renamed as PBDTTBOv2 (**P1**) and PBDTBOv2 (**P2**) respectively, have higher molecular weight than their literature analogues. The effect of molecular weight on photovoltaic properties were also investigated.

2.1.2 P3 and P4

P3 and **P4** are new conjugated polymers in the literature which was aimed to be synthesized to increase functionalities of **P1** and **P2**. The two-alkyl chain (octane) on benzoxadiazole core were planned to replace with (bromooctane) for **P3** and **P4**. The 1° bromine group on the tip of the alkyl chain is open for basic chemical reactions since bromine is considered as a good leaving group. This feature enabled polymers **P3** and **P4** for further post-polymerizations. As future work, this bromine group is planned to be replaced with thiol group and then will be activated by gold

NPs to increase absorption spectra of polymeric solar cells which will be constructed by **P3-S-AuNPs** and **P4-S-AuNPs**.

2.1.3 P5 and P6

2.1.3.1 P5

P5 is a new conjugated polymer for literature which was designed to compare possible effects of repositioned alkyl chain on electronic and mechanic properties of conjugated polymers. The alkyl group was planned to be repositioned from benzoxadiazole core to π -bridge group (thiophene). As known, the position of alkyl chains can manipulate crystallinity, interchain packing, and absorption coefficient which changes the electronic and mechanical properties of conjugated polymers (C. H. Cho et al., 2012).

2.1.3.2 P6

P6 is a new conjugated polymer for literature which was aimed to compare possible effects of π -bridge groups on electronic properties of conjugated polymers. The thiophene group from the literature polymer PBDTBO was planned to replace it with the selenophene group to construct a new conjugated polymer **P6**. Usage of different π -bridge groups is a proven strategy to manipulate plane conjugation since aromatic groups have the ability to regulate energy gaps, HOMO and LUMO levels, and absorption spectra of conjugated polymers (Gedefaw et al., 2016; L. Liu et al., 2019).

2.2 Synthetic Pathways for the Synthesis of Monomers

In this thesis study, six different conjugated polymers were synthesized. To obtain these polymers four different monomer units were synthesized. In this section, successful and unsuccessful synthetic attempts of monomers were discussed.

2.2.1 Synthetic Pathway of M1

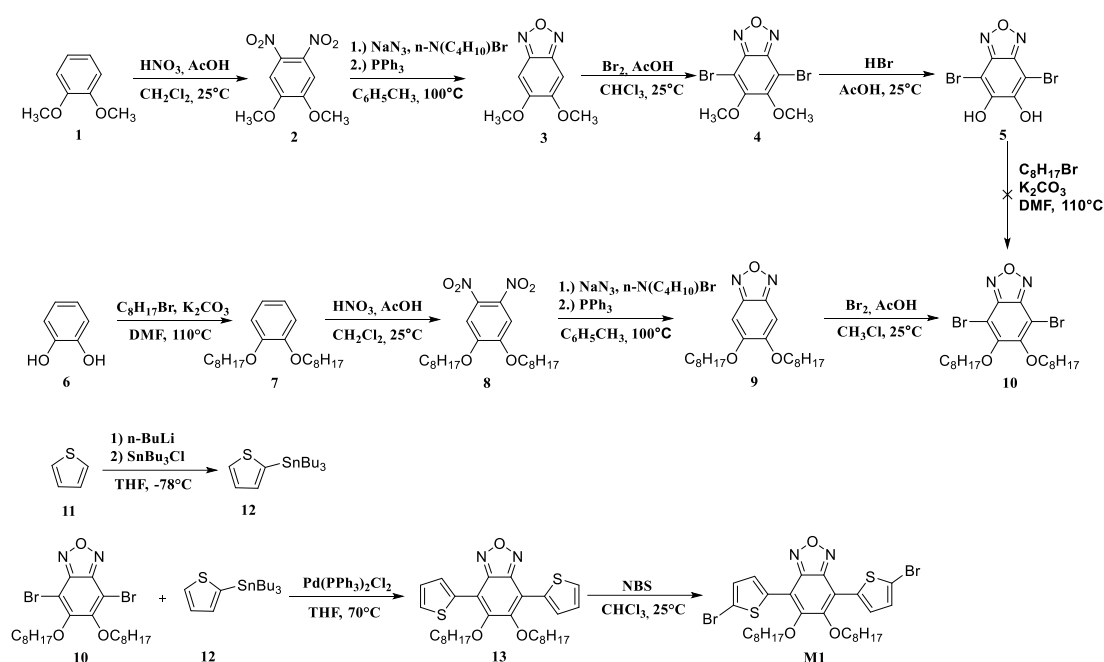


Figure 2.1. Synthetic pathway to obtain M1

2.2.1.1 Unsuccessful Approach

On the contrary to the literature, starting compound (1) was chosen as veratrole instead of catechol to obtain common core (compound 4) of M1, M2 and M3. Compound 2 was achieved by nitration reaction with fuming nitric acid (Shopsowitz et al., 2011). High yield was achieved (90%). Then, a ring closure reaction was performed (Bouffard & Swager, 2008) with sodium azide and compound 3 was obtained with a moderate yield (40%). After then, a bromination reaction was

performed (Bouffard & Swager, 2008) with molecular bromine since no selectivity was needed to obtain compound **4** and it was isolated in a good yield (78%). Compound **5** was synthesized via demethylation of compound **4** with concentrated hydrobromic acid (Prima et al., 2019) with a reasonable yield (72%). To achieve product **10** Williamson Ether Synthesis was tried. Mild base potassium carbonate was used to deprotonate the hydroxyl groups on compound **5**, then alkyl halide was introduced to the reaction medium (Goker et al., 2016). The yield was very poor (less than 10%) and attempts for isolation of product (**10**) were failed. Reasons behind failure may result from steric hindrance due to the presence of bromine on the benzoxadiazole group or instability of formed intermediate due to restricted charge delocalization.

2.2.1.2 Successful Approach

After the failure of the first pathway, the literature was followed. Compound **7** was synthesized by the Williamson ether synthesis method. A mild base (potassium carbonate) was used to deprotonate the hydroxyl groups of compound **6**, then 1-bromooctane was introduced to the reaction medium. Compound **7** was successfully obtained with a very good yield (86%). Then, a nitration reaction was performed to obtain compound **8** with a fuming nitric acid and the target product was isolated with a high yield (84%). After that, ring closure reaction was performed with sodium azide but the yield was very low at first trials. To solve this problem, the literature isolation procedure of compound was revised. The decantation method was used instead of the extraction method and after that re-crystallization method was used instead of column chromatography. Compound **9** was obtained with a moderate yield (53%). Then, a bromination reaction was performed with molecular bromine and compound **10** was obtained successfully (78%). Compound **10** was coupled with stannylated thiophene by Stille Cross-Coupling method. At the end of the reaction, compound **13** was isolated with a very good yield (82%). Finally, bromination with

n-bromo succinimide (NBS) which is a mild and selective bromination reagent was performed and **M1** was successfully synthesized with a high yield (85%).

2.2.2 Synthetic Pathways of M2

2.2.2.1 Unsuccessful Synthetic Pathway

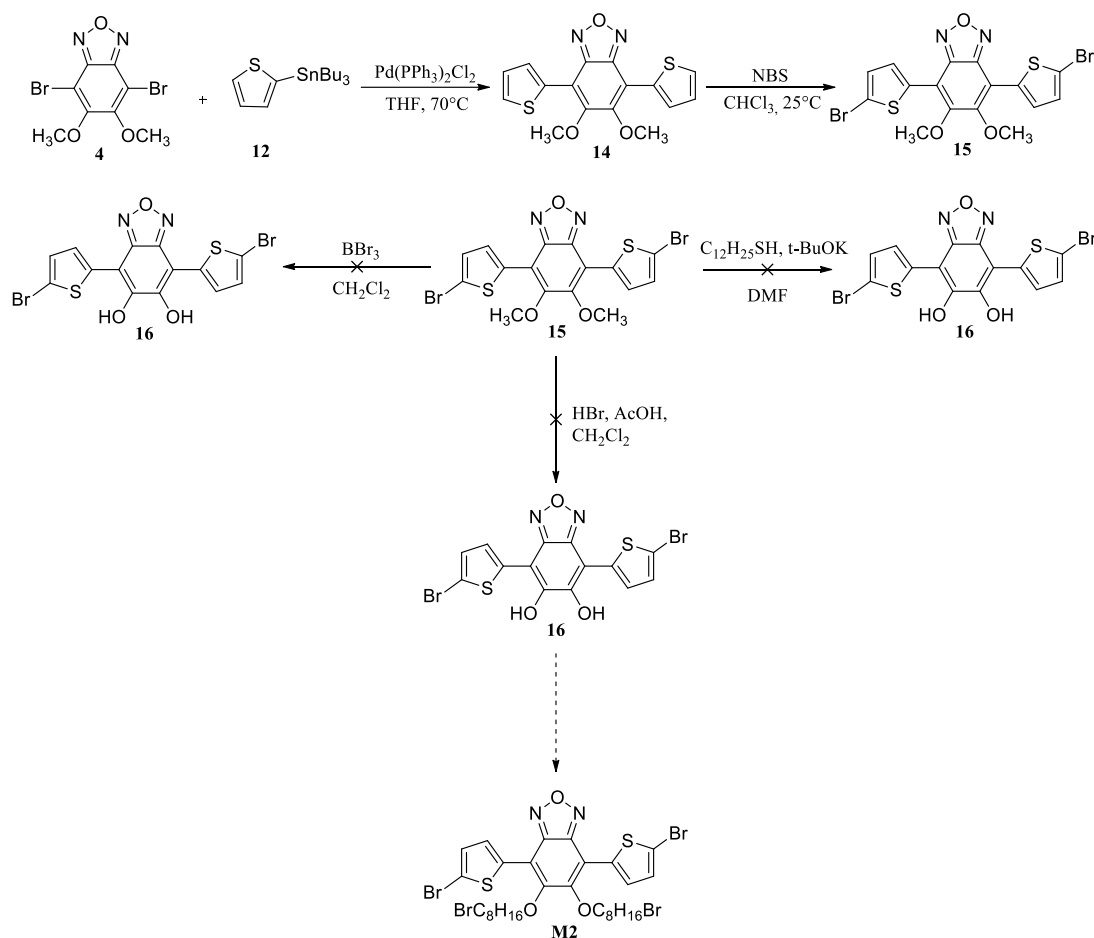


Figure 2.2. Unsuccessful synthetic pathway to obtain **M2**

Compound **14** was synthesized by the Stille Cross-Coupling reaction. compound **4** which was synthesized formerly, was coupled with stannylated thiophene at the presence of Pd catalyst and compound **14** was obtained with a good yield (74%). Then, compound **15** was synthesized with a bromination reaction. NBS was used as

a bromine source to avoid over bromination since NBS is selective and moderately reactive. Compound **15** was isolated successfully with a reasonable yield. (60%). To synthesize compound **16** three different reactions were tried but all of the reactions were failed. At the first trial, concentrated boron tribromide (BBr_3) was used for demethylation (Pässler & Knölker, 2011). BBr_3 significantly harsh reagent and it was caused to the decomposition of starting material. In the second trial, dodecanthiol and strong base were used (Goker et al., 2016) but again starting material was decomposed. At the last trial, the classic demethylation method with conc. HBr was tried (Prima et al., 2019). This time reaction was failed due to phase separation between solvents (acetic acid and DCM). Since compound **15** is not soluble in acetic acid and HBr is not soluble in DCM. A mixture of these solvents was used and phase separation was taken place. In the end, no reaction was observed and the starting material was recovered. The reason behind decompositions may come from the complexity of starting material. Since the starting material is fully conjugated and includes many heteroatoms, it is open for side reactions with harsh reagents.

2.2.2.2 Successful Synthetic Pathway

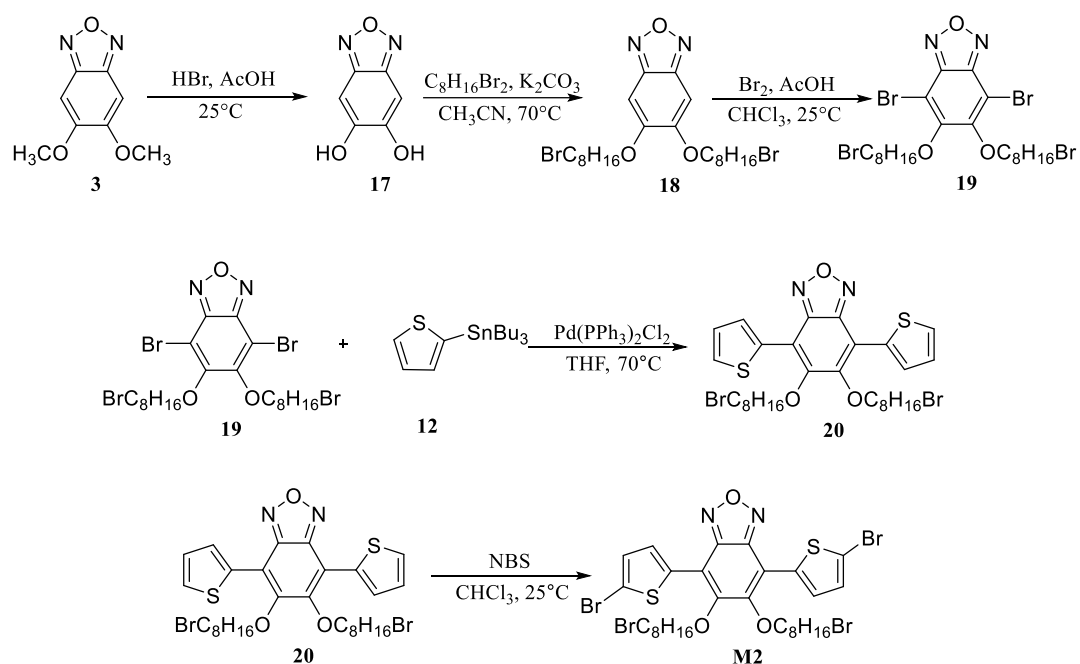


Figure 2.3. Successful synthetic pathway to obtain **M2**

Starting with compound **3**, a demethylation reaction was performed with concentrated hydrobromic acid to obtain compound **17**. The yield was good (82%). Then, alkylation was performed by Williamson Ether Synthesis reaction (Goker et al., 2016) and compound **18** was obtained with a moderate yield (57%). After, bromination reaction was performed with molecular bromine since no selectivity was needed. Compound **19** was synthesized successfully with a high yield (88%). Stille Cross-Coupling reaction (Aldenderfer et al., 2008) was used to obtain compound **20**. Compound **19** was coupled with stannylated thiophene and compound **20** was synthesized with a good yield (73%). Finally, bromination with *n*-bromo succinimide (NBS) which is a mild and selective bromination reagent was performed and **M2** was successfully synthesized with a high yield (81%).

2.2.3 Synthetic Pathways of M3 and M4

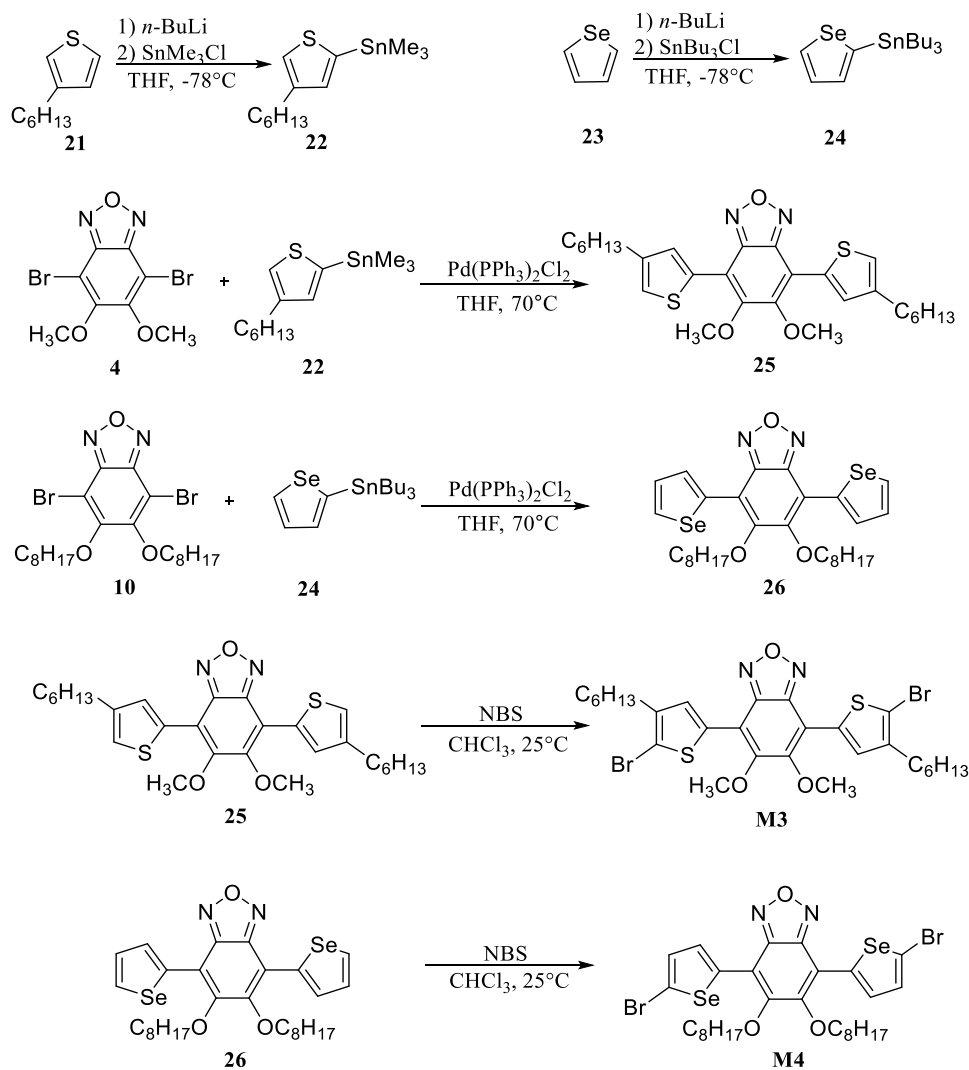


Figure 2.4. Synthetic pathway of **M3** and **M4**

Starting from compound **4** and compound **10**, the Stille Cross-Coupling reaction was performed to obtain compounds **25** and **26**. Compound **4** and **10** were coupled with stannylated 3-hexyl thiophene and stannylated selenophene respectively. Compound **25** and **26** were obtained with a reasonable yield of 76% and 71% respectively. Finally, bromination with *n*-bromo succinimide (NBS) was performed to obtain **M3** and **M4**. The reaction yield was moderate (67%) for **M3** and was good (79%) for **M4**.

2.3 Synthesis of Target Conjugated Polymers

All polymerization reactions are designed to be completed in a short time with a high molecular weight. The idea behind this, avoiding a decrease in the activities of catalyst during polymerization reactions. The Pd-based catalysts show a decrease in their activities when exposed to air or humidity. During long reaction times, the possibility of exposure to air is increasing. In order to prevent this situation, the idea was to increase the rate of polymerization. To speed up polymerization, the solvent amounts were minimized and monomer amounts were increased. As a result, for **P1** when compared with literature (Jiang et al. 2014) more than 3.5 times higher value of M_n was obtained in six times shorter polymerization time. For **P2** (Jiang et al. 2011), 1.5 times higher value of M_n was obtained in six times shorter polymerization time. Detailed procedures for the synthesis of polymers are given in the experimental section.

2.3.1 Characterization of Conjugated Polymers

The chemical structures of polymers were verified by IR spectroscopy. IR spectra of polymers were given in the appendix. The functional groups on polymers can be verified from an IR spectrum. NMR spectra of polymers could not be obtained due to solubility problems of polymers in chloroform. Gel permeation chromatography (THF as eluent, and polystyrene as standard) was used to obtain M_n , M_w and PDI values. All polymers are soluble in common organic solvents such as tetrahydrofuran, chlorobenzene, dichlorobenzene, etc.

2.4 Number Average Molecular Weight of Polymers

As described in section 2.3, the polymerization rate was increased and the reaction time was decreased. The polymerization reactions resulted in excellent M_n values except for **P5** (Table 2.1). The reason for the low M_n value for **P5** may result from the position of the alkyl chain. The alkyl group was repositioned from benzoxadiazole core to π bridge-group thiophene. The new position of the alkyl group where it is closer to the polymerization center may cause steric hindrance and inhibits polymerization reaction.

2.5 Thermal Stabilities of Polymers

In the appendix part, TGA thermograms of the polymers are available. TGA analysis was run under a nitrogen atmosphere at 10 °C/min. heating speed between the temperature interval of 25 °C-600 °C. TGA thermograms show the starting points of 5% weight loss of **P1**, **P2**, **P3**, **P4**, **P5** and **P6** are 327 °C, 326 °C, 305 °C, 313 °C, 344 °C and 318 °C respectively. Polymers show relatively high thermal stability which prevents deformation of morphology. Also, this stability prevents the degradation of the polymeric photoactive layer under applied electric fields.

Table 2.1 Results of polymerizations and thermal data of polymers

Polymer	M_n (kDa)	M_w (kDa)	PDI	T_d (°C)
P1	224	538	2.40	327
P2	90	385	4.28	326
P3	92	310	3.37	305
P4	75	270	3.60	313
P5	12	14	1.17	344
P6	66	200	3.03	318

2.6 Electrochemical Studies

Cyclic voltammetry experiment (CV) was performed to investigate the electrochemical properties of the polymers. Polymers, which were dissolved in CHCl_3 was spray coated on ITO glasses and a three-electrode system was used to conduct experiments. As shown in Figure 2.5. all polymers are n- and p- dopable which means they have ambipolar character. The ambipolar character of polymers can be accommodated to the π -bridge groups selenophene and thiophene units in the polymer backbone. They provide polymers n-type doping character.

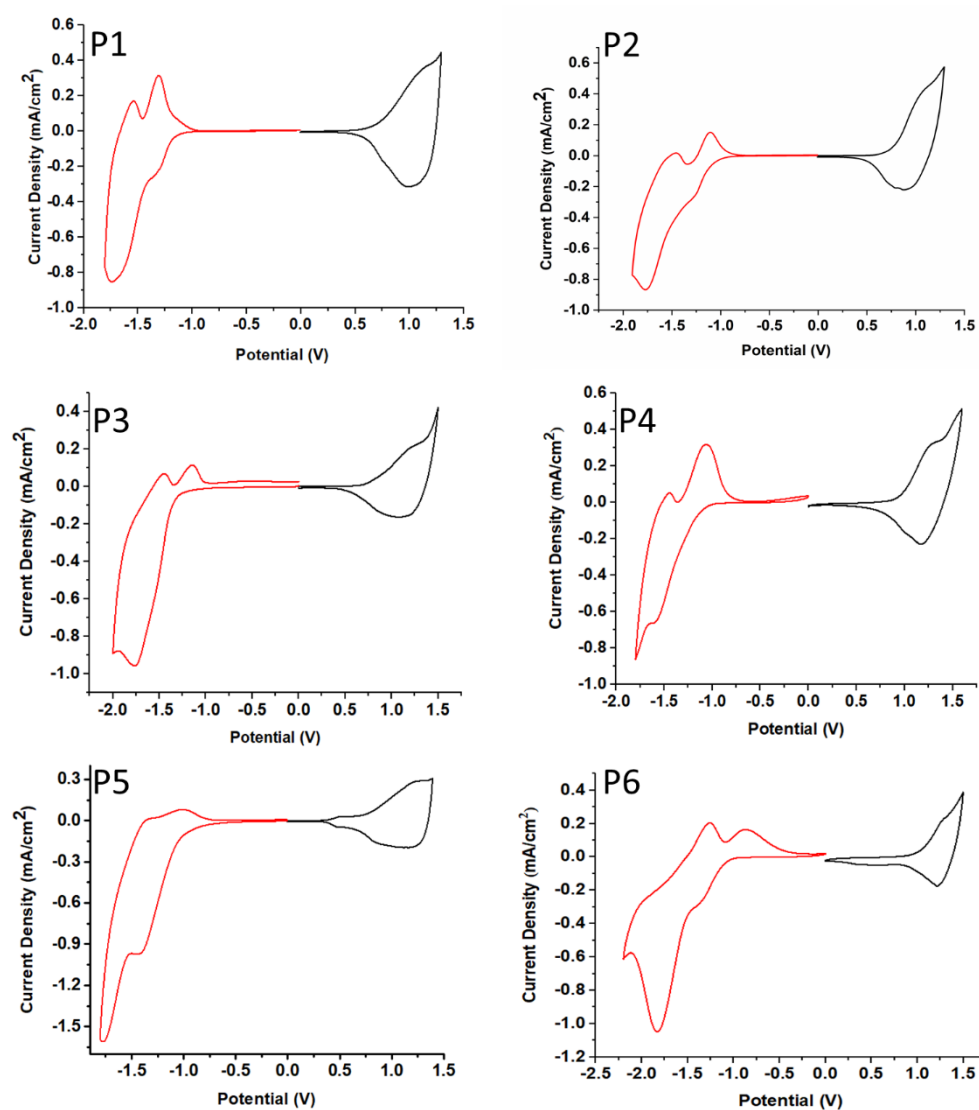


Figure 2.5. Cyclic voltammograms of the polymers at 100 mV/s scan rate

Oxidation and reduction onset potentials were used to calculate HOMO and LUMO energy levels. The value of the electronic band gap (E_g^{el}) was calculated by measuring the difference between the HOMO and LUMO levels.

P1, p-doping redox couples were found as 1.14/0.98 V and during n-type doping, redox couples were found as -1.34/-1.30 V and -1.75/-1.54 V. The onset values are $E_{ox}^{onset} = 0.68$ V and $E_{red}^{onset} = -1.15$ V. The electronic band gap (E_g^{el}) is 1.83 eV

P2, p-doping redox couples were found as 1.13/0.87 V and during n-type doping redox couples were found as -1.27/-1.10 V and -1.77/-1.46 V. The onset values are $E_{ox}^{onset} = 0.78$ V and $E_{red}^{onset} = -1.08$ V. The electronic band gap (E_g^{el}) is 1.86 eV.

P3, p-doping redox couples were found as 1.23/1.15 V. During n-type doping redox couples were found as -1.76/-1.45 V. The onset values are $E_{ox}^{onset} = 0.70$ V and $E_{red}^{onset} = -1.33$ V. The electronic band gap (E_g^{el}) is 2.03 eV.

P4, p-doping redox couples were found as 1.26/1.17 V. During n-type doping redox couples were found as -1.60/-1.45 V. The onset values are $E_{ox}^{onset} = 0.95$ V and $E_{red}^{onset} = -1.15$ V. The electronic band gap (E_g^{el}) is 2.06 eV.

P5, p-doping redox couples were found as 1.39/1.16 V. During n-type doping redox couples were found as -1.45/-1.01 V and -1.78/-1.35 V. The onset values are $E_{ox}^{onset} = 0.70$ V and $E_{red}^{onset} = -1.05$ V. The electronic band gap (E_g^{el}) is 1.76 eV

P6, p-doping redox couples were found as 1.30/1.22 V. During n-type doping redox couples were found as -1.83V and -1.37/-1.82 V. The onset values are $E_{ox}^{onset} = 1.03$ V and $E_{red}^{onset} = -1.08$ V. The electronic band gap (E_g^{el}) is 2.11 eV.

Table 2.2 Detailed electrochemical properties of the polymers

	$E_{p-doping}$ (V)	$E_{p-dedoping}$ (V)	$E_{n-doping}$ (V)	$E_{n-dedoping}$ (V)	HOMO (eV)	LUMO (eV)	E_g^{el} (eV)
P1	1.14	0.98	-1.34/-1.75	-1.30/-1.54	-5.43	-3.60	1.83
P2	1.13	0.87	-1.27/-1.77	-1.10/-1.46	-5.53	-3.67	1.86
P3	1.23	1.15	-1.76	-1.45	-5.45	-3.42	2.03
P4	1.26	1.17	-1.60	-1.45	-5.67	-3.60	2.07
P5	1.39	1.16	-1.45/-1.78	-1.01/-1.35	-5.46	-3.70	1.76
P6	1.30	1.22	-1.31/-1.83	-1.37/-1.82	-5.78	-3.66	2.10

In a summary, all the polymers showed suitable energy levels to construct an organic solar cell. HOMO and LUMO energies for PC₇₁BM are -5.90 eV and -3.90 eV respectively which are previously determined by Toppare and Çirpan groups (Istanbulluoglu et al., 2015). Energy levels of PC₇₁BM and the polymers yield sufficiently large HOMO-HOMO and LUMO-LUMO offsets to satisfy efficient charge transfer and dissociation for corresponding devices. Also, the electronic band gaps of polymers are narrow (<2.1 eV) which increases the possibility of harvesting photons from solar radiation (Sekine et al., 2014).

P1 and **P2** have a narrower electronic band gap when compared with former analogues from the literature (-1.99 eV and -2.11 eV (Jiang et al. 2011 and Jiang et al. 2014) respectively). The reason behind this band gap decrease could be from increase in effective π -conjugation length. It could be clear evidence for Mn dependence of π -conjugation length and thus, electrochemical properties of polymers.

P3 and **P4** have a broader electronic band gap when compared with **P1** and **P2**. The reason behind this band gap increase could be from decreases in effective π -conjugation length. The bromine groups on the tip of alkyl chains may disturb the linearity and aggregation of polymers in solid-state since bromine is a considerably big atom.

P2 and **P6** have different π -bridging groups between donor and acceptor units. While **P2** has thiophene, **P6** has selenophene. Selenophene has a larger size than sulfur which is lowering the aromaticity of the selenophene ring. Thus, the electron-donating ability of selenophene is higher than thiophene. From previous studies (Kim et al., 2012), the stronger electron-donating ability of selenophene was resulted in a decrease in LUMO level without changing the HOMO level but according to electrochemical results, **P6** has a higher electronic band gap than **P2** which is unexpected. The reason behind this anomaly could be from a personal or random error during CV measurement. For example, disturbance of inert atmosphere hence the presence of oxygen or other reactive gases could affect the p-doping and n-doping process.

2.7 Optical Studies

All the polymers were investigated in the visible and near-infrared regions with a UV-VIS-NIR spectrometer. Both solution and thin-film absorption spectra were obtained for all the polymers. Optical band gaps of polymers were calculated from $\lambda_{\text{max}}^{\text{onset}}$ values. Also, λ_{max} values of the polymers were obtained from the thin film UV spectra. Optical band gaps of polymers are lower than electrical band gaps due to the formation of free electrons during the electrochemistry experiment (S. W. Cho et al., 2010).

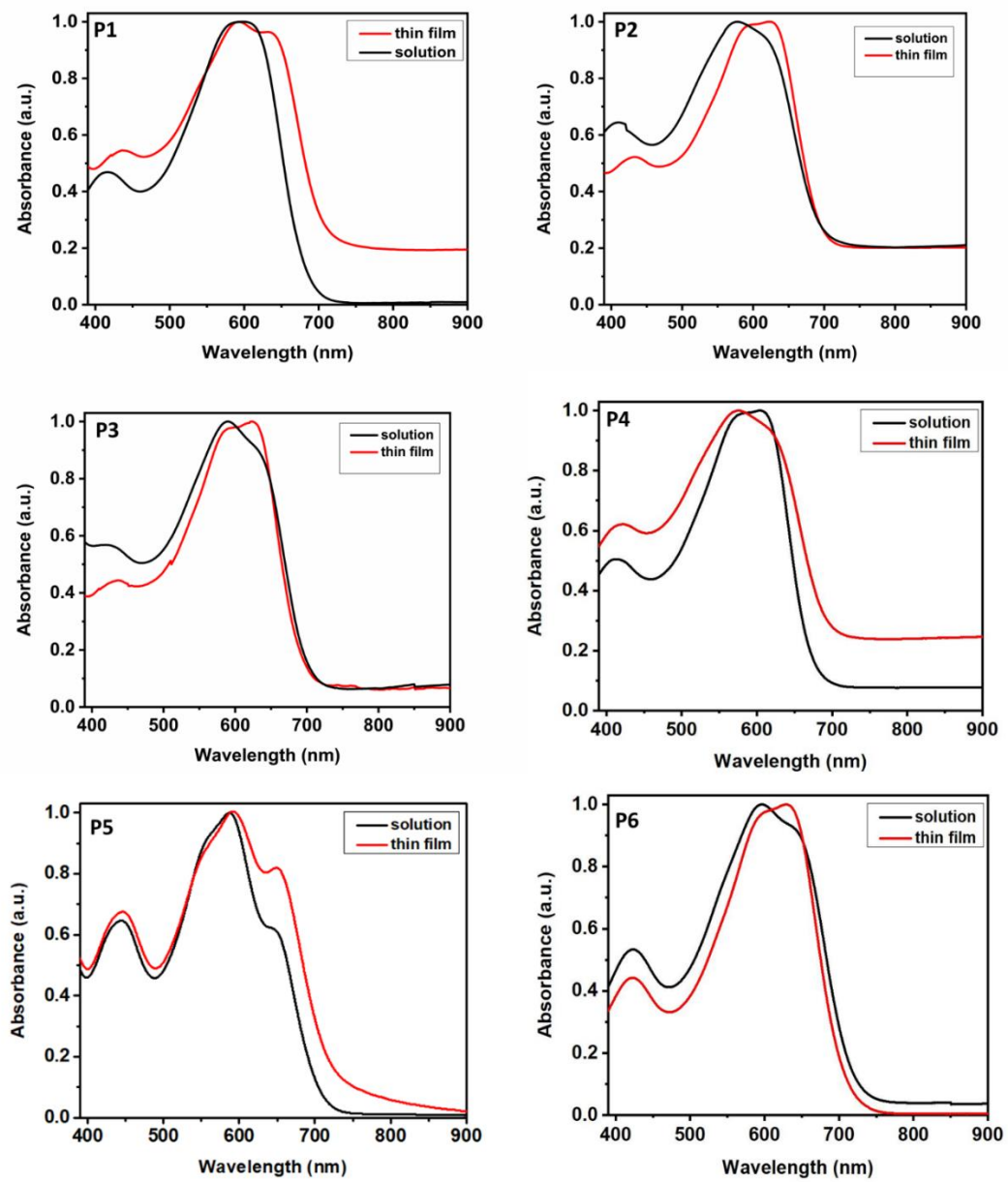


Figure 2.6. Normalized absorption spectra of polymers in solution and solid form

Table 2.3. Optical properties of the polymers

	λ_{\max} (nm)	$\lambda_{\max}^{\text{onset}}$ (nm)	E_g^{op} (eV)
P1	600	686	1.81
P2	623	705	1.76
P3	590	712	1.74
P4	576	726	1.74
P5	591	723	1.72
P6	630	727	1.71

Each absorption spectrum has specific two absorption bands. The first band which is narrow is lying at the region between 350 nm to 500 nm. This band could be assigned to localized π - π^* transitions. The second band which is broader than the first one has a range from 500 nm to 700 nm could be assigned to intermolecular charge transfer (ICT) between the donor and acceptor units in the polymer backbone (Yuan et al., 2012).

P1 and **P2** showed broader absorption spectra compared to former analogues from the literature. Synthesized polymers that having higher Mn values are showing red-shifted absorption maxima (λ_{\max}). The reason behind this shift could be from increases in π -conjugation length and chain aggregation. It could be clear evidence for Mn dependence of absorption spectra and thus, optical properties of polymers. In addition to that, red-shifted absorption spectra were observed at the thin-film state of **P1** and **P2** which could indicate that in solid-state that polymers showed crystalline character, with long-range ordered π - π stacking and conspicuous aggregation (Cuesta et al., 2019).

Table 2.4 Comparison of absorption spectra of **P1** and **P2** with literature analogues. (Jiang et al. 2011 and Jiang et al. 2014 respectively)

	P1	P1 Literature	P2	P2 Literature
λ_{\max} (nm)	600	576	623	575
Range	490 to 690	500 to 650	480 to 680	475 to 650

P3 and **P4** have a bromine functional group on the tip of their alkyl chains. Their solid-state absorption spectra are slightly different from solution absorption spectra which could indicate that polymers showed amorphous character, with no long-range ordered π - π stacking and poor aggregation in solid-state (Cuesta et al., 2019). The bromine groups on the tip of alkyl chains may disturb the linearity and aggregation of polymers in solid-state since bromine is a considerably big atom.

P1 and **P5** have alkyl chains at different positions. **P5** has a considerably lower M_n value than **P1** which was explained in section 2.4. In addition, the thin film absorbance spectra significantly differ from each other. It could be an indication of with the increasing of molecular weight, the range of π - π stacking is and chain aggregation is increasing in solid-state.

P2 and **P6** have different π -bridging groups between donor and acceptor units. While **P2** has thiophene, **P6** has selenophene. As mentioned in the electrochemical properties section, the presence of selenophene reduces LUMO level since the electron-donating ability of selenophene higher than thiophene (S. W. Cho et al., 2010). The anomaly which was observed in electrochemical properties was corrected in optical properties. Hence, the optical band gap of **P6** was found lower than that of **P2** as expected.

2.8 Photovoltaic Studies of the Polymers

2.8.1 P1 and P2

2.8.1.1 Conventional Device Structure

The energy level diagram of OSC which based on **P1** and **P2** was illustrated in Figure 2.7. HOMO, LUMO and electronic band gap measurements were described in Section 2.6.

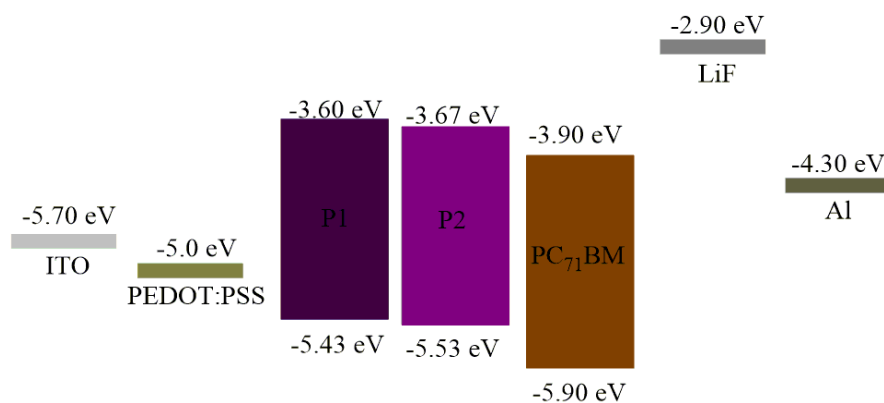


Figure 2.7. Energy level diagram of **P1** and **P2** based OSC with conventional device architecture

Formerly constructed devices with PBDTTBO (Jiang et al., 2014) were reconstructed for **P1** with the same parameters to provide a proper comparison. In other words, for **P1** dichlorobenzene (DCB) was used as a solvent, a fixed ratio of 1:2 of polymer: PC₇₁BM and total concentration (%3) was used and best device performance was obtained.

For **P2**, the same approach was planned with **P1** however, the described construction which is the total concentration was %4 and a fixed ratio of 1:1 of polymer: PC₇₁BM in the literature (Jiang et al., 2011) was failed. Polymer concentration was excessive and during the spin coating process, the active layer was not coated homogeneously

on the surface of ITO. Then, a regular optimization procedure was followed and the best device performance was obtained.

Table 2.5 Comparison of photovoltaic properties of **P1** and **P2** with PBDTTBO and PBDTBO

Polymers	Solvent	Weight	Polymer:PC ₇₁ Ratio	V _{oc} (V)	J _{sc} (mA cm ⁻²)	FF (%)	η (%)
P1	DCB	3%	1:2	0.87	17.33	68.93	10.33
PBDTTBO	DCB	3%	1:2	0.85	11.80	59.00	5.90
P2	DCB	3%	1:2	0.79	13.17	62.01	6.43
PBDTBO	DCB	4%	1:1	0.86	10.4	64.4	5.70

From Table 2.5, the PCE of the device which is constructed with **P1** by using the same parameters of literature was found 1.75 times higher than the formerly constructed device by Jiang et al., 2014. With the PCE of 10.33%, the highest reported power conversion efficiency was obtained among the conjugated polymers that include benzoxadiazole as an acceptor unit in their D:A alternating backbone. The difference in the V_{oc} levels is negligible which is expected since HOMO levels of **P1** and PBDTBO were not significantly different from each other. On the other hand, **P1** showed overwhelming superiority on PBDTTBO at J_{sc} and FF parameters. Starting with J_{sc}, the reason behind the superiority of the **P1** could be from the increased molecular weight. The relatively lower molecular weight of PBDTTBO may cause less absorption from incoming solar radiation. Also, wider fibrils of a polymer may be formed due to the higher solubility of polymers that have lower molecular weight. Wider fibrils reduce exciton diffusion which also reduces J_{sc} value. Lastly, the lower FF value of PBDTTBO compared to **P1**, could be explained with differences in active layer morphology since the FF value is primarily assigned by the powerful D-A phase separation at the active layer, with an interpenetrated bicontinuous morphology (Li et al., 2014). To summarize, although **P1** and

PBDTTBO have identical donor and acceptor units in their backbone, the difference between J_{sc} and FF values are high. Thus, the power conversion efficiency of PBDTTBO is lower than that of **P1**. This result could be clear evidence for the effect of molecular weight on photovoltaic properties.

For **P2**, from Table 2.5, a PCE of 6.43% was obtained with the device in which **P2** was used as a polymeric donor unit in the active layer. 1.16 times higher efficiency was obtained than a formerly constructed device with the same polymeric donor unit by Jiang et al., 2011. The difference in the V_{oc} values is negligible which is expected since repeating units of **P2** and PBDTTBO were not significantly different from each other. On the other hand, **P1** showed superiority on PBDTTBO at the J_{sc} parameter. The reason behind the superiority of the **P1** could be from the increased molecular weight. The relatively lower molecular weight of PBDTTBO may cause less absorption in solid form from incoming radiation. Also, wider fibrils of a polymer may be formed due to the higher solubility of polymers that have lower molecular weight. Wider fibrils reduce exciton diffusion which also reduces J_{sc} value (Li et al., 2014). Lastly, there was no significant difference for FF values observed.

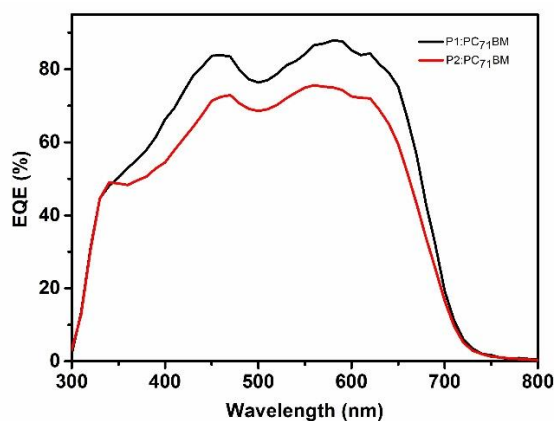


Figure 2.8. EQE curves of organic solar cells of polymer:PC₇₁BM blends

EQE curves of P1:PC₇₁BM and P2:PC₇₁BM blends were obtained to verify J_{sc} values of devices. J_{sc} values of 15.3 mA cm⁻² and 13.0 mA cm⁻² were obtained from EQE curves respectively for **P1** and **P2**. EQE curves showed insignificant loss and they confirmed to J_{sc} values obtained from devices.

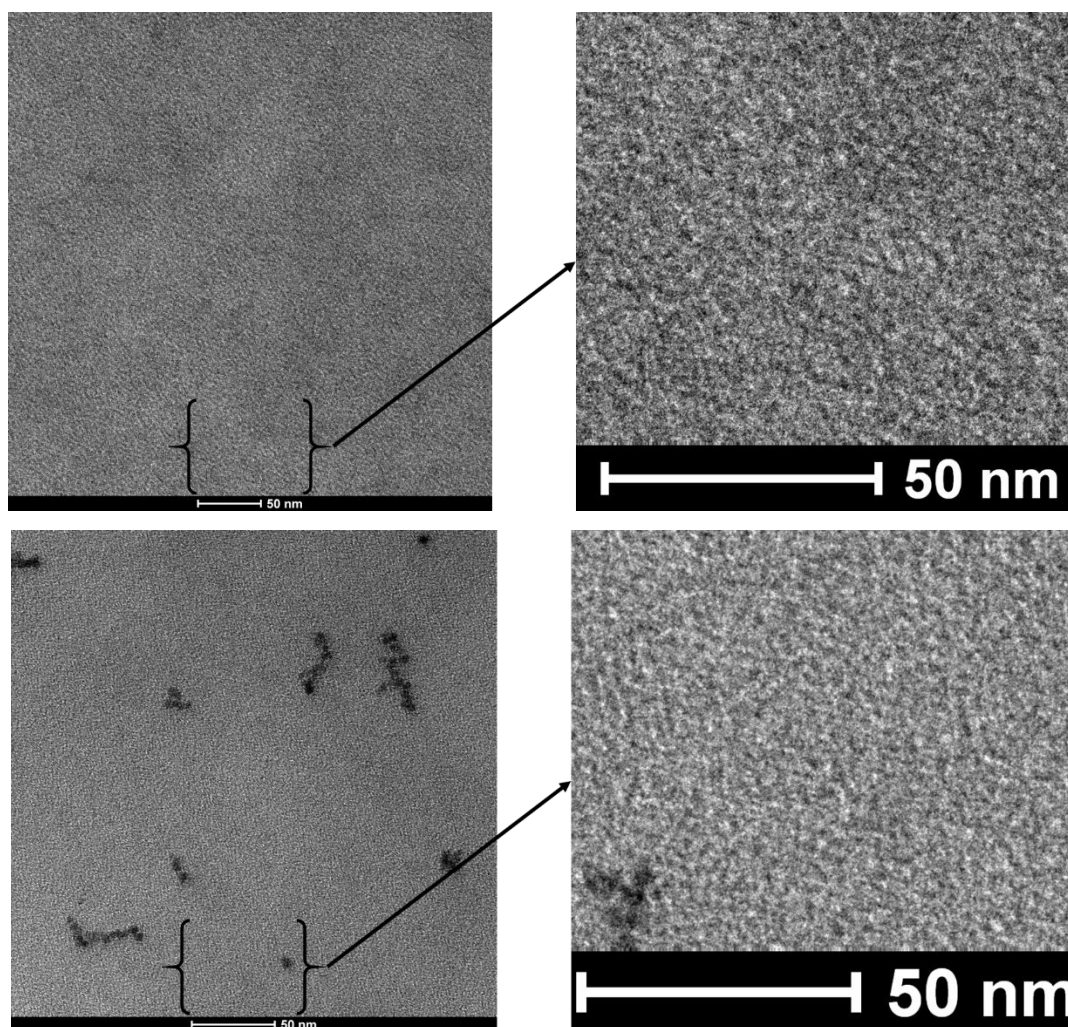


Figure 2.9. TEM images of P1: PC₇₁BM (1:2, w/w) and P2: PC₇₁BM (1:2, w/w) blends

Figure 2.9 shows TEM images of P1: PC₇₁BM (1:2, w/w) and P2: PC₇₁BM (1:2, w/w) blends with a scale of 50 and 100 nm respectively. While polymers are appearing as bright, PC₇₁BM appearing as dark regions. The images of the **P1** blend showed a good homogenous mixture, the **P1** and PC₇₁BM mixed very-well in each other. This could be explained by obtaining high FF values. Also, narrow fibril formation was observed from TEM images due to the high molecular weight of **P1**. As mentioned earlier, with the formation of narrower fibrils, the possibility of reaching the donor-acceptor interface for excitons are increasing. That could explain, obtaining remarkable J_{sc} value. From the TEM images of the **P2** blend, again good

homogenous mixture and narrow fibril formation were observed. The dark black spots on the image of the **P2** PC₇₁BM blend are undissolved PC₇₁BM. The relatively lower FF value of the **P2** blend, when compared with the **P1** blend, could be explained from these spots.

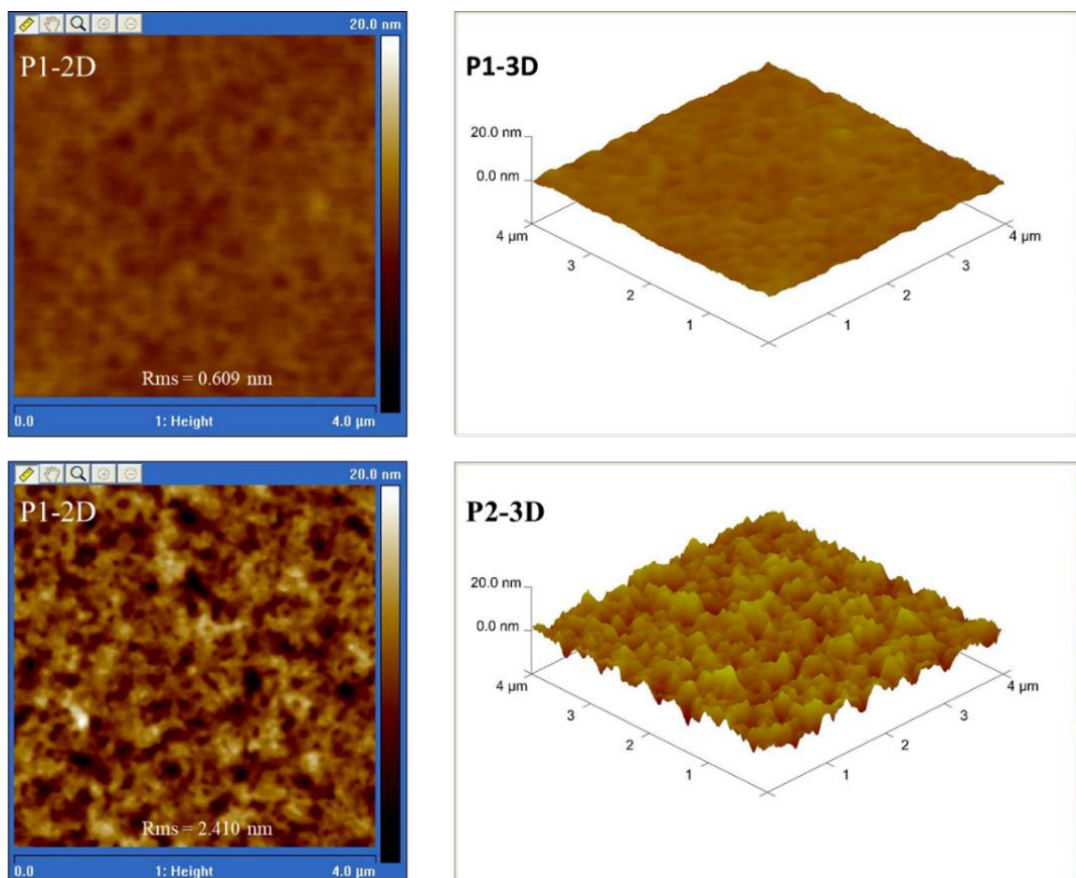


Figure 2.10. Topographic AFM images of P1: PC₇₁BM (1:2, w/w) and P2: PC₇₁BM blends

Figure 2.10. shows topographic AFM images of polymer blends **P1** and **P2** with PC₇₁BM. A smoother surface (0.609 nm) was observed when compared **P1** with literature analogue and a rougher surface (2.410 nm) was observed when compared **P2** with literature analogue. Since FF values are directly correlated with the morphology of the active layer, the increased FF value for **P1** and decreased FF value for **P2** was obtained when compared with literature analogues as expected.

To summarize, although **P1**, **P2** and PBDTTBO, PBDTBO have identical donor and acceptor units in their backbone, higher PCE was obtained with conventional device structure by increasing molecular weight of polymers. Hence, this result could be clear evidence for the effect of molecular weight on photovoltaic properties.

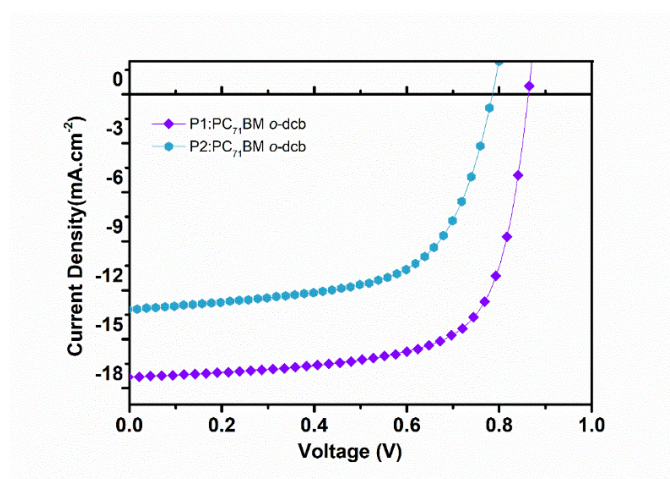


Figure 2.11. J-V curves of **P1** and **P2** for their best device performances

2.8.1.2 Inverted Device Structure and Ternary Blend Approach for **P1** and **P2**

Considerably high values of PCEs were obtained for both **P1** and **P2** with the conventional device structure. For further enhancements, two different device structures were constructed. The first ternary blend active layer was constructed instead of binary. As mentioned in section 1.7.1 ternary blends have been using to provide desirable incoming light absorption (Lu et al., 2014) but after several attempts, decreased FF values were observed without improving J_{sc} values when compared with the binary active layer. The reason could be poor mixing of polymeric donor units which could result in the poor D-A phase separation at the active layer, with a poorly interpenetrated bicontinuous morphology. In future work, different polymeric donor units will be mixed with **P1** and **P2** to achieve better active layer morphology. Table 2.6 summarizes the photovoltaic performances after ternary studies of **P1** and **P2**.

Table 2.6 Summary of the photovoltaic properties for devices with ternary blend active layer

Polymers	Solvent	Weight	Polymer:PC ₇₁ BM Ratio	V _{oc} (V)	J _{sc} (mA cm ⁻²)	FF (%)	PCE (%)
P1:PCE10 ^a	DCB	3%	0.9:0.1:2	0.82	15.06	52.44	6.47
P1:PCE10 ^a	DCB	3%	0.7:0.3:2	0.83	11.42	55.59	5.28
P1:AsI ₂ P1 ^b	DCB	3%	0.9:0.1:2	0.76	12.13	55.37	5.10
P1:AsI ₂ P1 ^b	DCB	3%	0.7:0.3:2	0.75	12.21	55.45	5.06
P2:PCE10 ^a	DCB	3%	0.9:0.1:2	0.76	9.56	58.89	4.25
P2:PCE10 ^a	DCB	3%	0.7:0.3:2	0.77	7.69	59.72	3.45

a. Commercial polymeric donor unit with 10% PCE b. polymeric donor unit which synthesized by a former student of Prof. Dr. Ali Çırpan

Secondly, an inverted device structure (ITO/ZnO/Polymer:PC₇₁BM/MoO₃/Ag) was constructed for **P1** and **P2**. As mentioned in section 1.7.1 inverted device architecture has been used for both increasing device stability and PCE (Vohra et al., 2015) but after the first attempt, a significant decrease was observed for FF and J_{sc} values when compared to conventional device architecture. In future work, further optimizations and analysis will be performed to clarify the reasons behind the device performance decreases. Table 2.7 summarizes photovoltaic performances after inverted device studies of **P1** and **P2**.

Table 2.7 Summary of the photovoltaic properties for devices with an inverted device structure

Polymers	Solvent	Weight	Polymer:PC ₇₁ BM Ratio	V _{oc} (V)	J _{sc} (mA cm ⁻²)	FF (%)	PCE (%)
P1	DCB	3%	1:2	0.82	8.40	52.46	3.59
P2	DCB	3%	1:2	0.82	9.76	51.85	4.12

2.8.2 P3 and P4

The energy level diagram of OSC which is based on **P3** and **P4** was illustrated in Figure 2.12. HOMO, LUMO and electronic band gap measurements were described in Section 2.6.

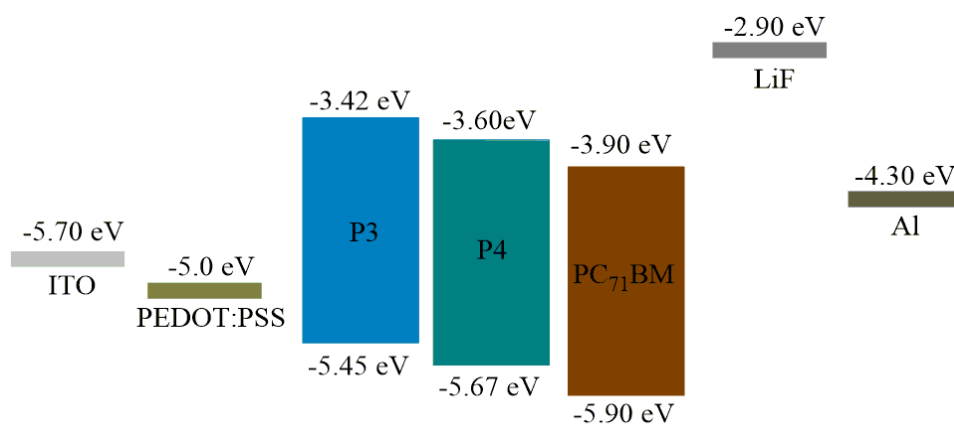


Figure 2.12. Energy level diagram of **P3** and **P4** based OSC with conventional device architecture

Table 2.

8 Summary of the pre-photovoltaic studies for polymers **P3** and **P4**

Polymer:PC ₇₁ BM (w:w)	J _{sc} (mA/cm ²)	V _{oc} (V)	FF %	η %
1:2 (P3) (2%)	9.78	0.79	52	4.06
1:3 (P3) (2%)	10.71	0.79	52	4.41
1:4 (P3) (2%)	8.17	0.78	49	3.11
1:3 (P3) (2.5%)	10.93	0.76	59	4.29
1:2 (P4) (2%)	5.62	0.67	46	1.74

Exceeding the 1:3 ratio of P3: PC₇₁BM at 2% (w/v) causes a decrease in the J_{sc} value (Table 2.8). This could be explained by decreasing the polymer ratio in the blend. The absorption intensity of the active layer, which mostly belongs to the polymer due to the low absorptivity of PC₇₁BM towards AM1.5G, is generally responsible for the J_{sc} values. After, P3:PC₇₁BM ratio optimization was completed, it is observed that the 1:3 ratio was the best among others. The ratio optimizations which were performed at 2% (w/v) were followed by blend concentration optimizations. In order to achieve enhanced current density values with increasing absorption of incoming radiation blend concentration was increased. When the blend concentration was increased from 2% to 2.5%, the PCE of device was decreased from 4.41% to 4.29%. Hence, optimum blend concentration was determined as 2%. As a future work, the thickness optimizations will be performed to obtain optimum parameters of the device. Device optimizations for **P4** were just started, as a future work they will be completed to reach optimum device parameters.

2.8.3 P5

The energy level diagram of OSC which is based on **P5** was illustrated in Figure 2.13. HOMO, LUMO and electronic band gap measurements were described in Section 2.6.

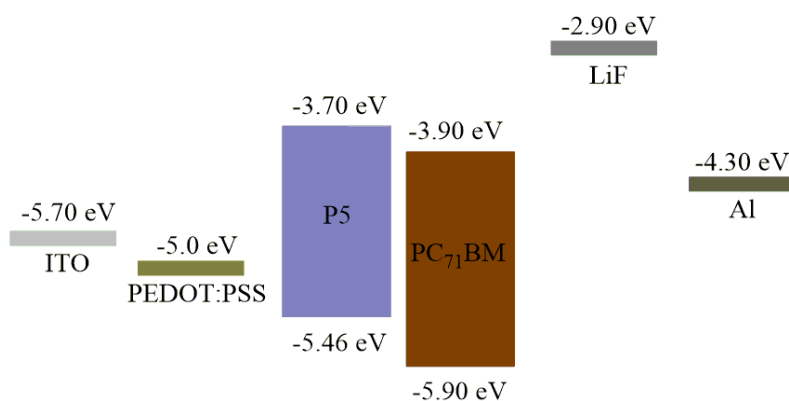


Figure 2.13. Energy level diagram of **P5** based OSC with conventional device architecture

The photovoltaic properties with respect to optimization studies for **P5** were summarized in Table 2.9,

Table 2.9 Summary of the photovoltaic properties for polymer **P5**

P3:PC ₇₁ BM (w:w)	J _{sc} (mA/cm ²)	V _{oc} (V)	FF %	η %	RPM	Treatment
1:1 (2%)	3.20	0.59	41.24	0.78	500	-
1:2 (2%)	4.76	0.59	39.18	1.10	500	-
1:3 (2%)	3.75	0.59	40.96	0.91	500	-
1:4 (2%)	2.82	0.62	47.04	0.84	500	-
1:2 (3%)	5.66	0.61	41.60	1.44	500	-
1:2 (3.5%)	5.60	0.58	35.39	1.15	500	-
1:2 (3%)	8.38	0.55	35.32	1.63	350	-
1:2 (3%)	5.66	0.56	36.19	1.14	750	-
1:2 (3%)	3.97	0.67	44.01	1.18	350	2% DIO
1:2 (3%)	4.88	0.63	35.32	1.09	350	3% DPE
1:2 (3%)	2.99	0.60	27.37	0.49	350	2% CN

Exceeding the 1:2 ratio of polymer: PC₇₁BM at 2% (w/v) causes a decrease in the J_{sc} value (Table 2.9). This could be explained by decreasing the polymer ratio in the blend. The absorption intensity of the active layer, which mostly belongs to the polymer due to the low absorptivity of PC₇₁BM towards AM1.5G, is generally responsible for the J_{sc} values. After, polymer:PC₇₁BM ratio optimization was completed, it is observed that the 1:2 ratio was the best among others. The ratio optimizations which were performed at 2% (w/v) were followed by blend

concentration optimizations. In order to achieve enhanced current density values with increasing absorption of incoming radiation blend concentration was increased. When the blend concentration was increased from 2% to 3%, the J_{sc} value increased from 4.76 mA/cm² to 5.66 mA/cm². However, when the ratio was increased from 3% to 3.5% both J_{sc} and FF values decreased. J_{sc} was decreased from 5.66 mA/cm² to 5.60 mA/cm² and FF was decreased from 41.60% to 35.39%. Hence optimum condition was determined in terms of blend concentration as 3%. After the conclusion of blend concentration optimizations, the thickness optimizations were started. The blend ratio optimizations were performed at 500 rpm. First, rpm was increased to 750 to decrease the thickness of the active layer because the extensive thickness could cause the failure in the charge transport to corresponding electrodes due to increased pathway. But J_{sc} value stays constant moreover, the FF value was decreased from 41.6% to 36.19% with the increased rpm from 500 to 750. It could cause the deterioration of bicontinuous morphology. Then the rpm decreased from 500 nm to 350 nm. After that, a decrease in FF value was observed again but the J_{sc} value increased dramatically to 8.38 mA/cm². The reason behind the improvement could from better absorptivity of incoming light with increasing the thickness of the active layer. Hence, the optimum optimization values were determined as P5:PC₇₁BM ratio of 1:2, blend concentration of 3% and at a spin coating ratio of 350 rpm. The final PCE of the device was recorded as 1.63% after optimizations.

For further optimization, three different additives were added to the active layer which are 1,8-diiodooctane (DIO), diphenyl ether (DPE) and chloronaphthalene (CN) in order to investigate the effects on overall device performance. After the addition of DIO, V_{oc} was increased from 0.55 V to 0.63 V without significant change in FF value but J_{sc} value was decreased dramatically from 8.38 mA/cm² to 3.97 mA/cm². With all these changes the PCE of the device was decreased from 1.63% to 1.18%. addition of DPE causes an increase in FF value from 35.32% to 44.01% and V_{oc} from 0.55 V to 0.67 V but J_{sc} value was decreased dramatically from 8.38 mA/cm² to 4.88 mA/cm². With all these changes the PCE of the device was decreased from 1.63% to 1.09%. Also, addition of CN increased V_{oc} from 0.55 V to

0.60 V but decreased FF from 35.32% to 27.37% and J_{sc} value from 8.38 mA/cm² to 3.97 mA/cm². With all these changes the PCE of the device was decreased from 1.63% to 0.49%. Overall, all additives decreased the J_{sc} values with a slight increment of V_{oc} values.

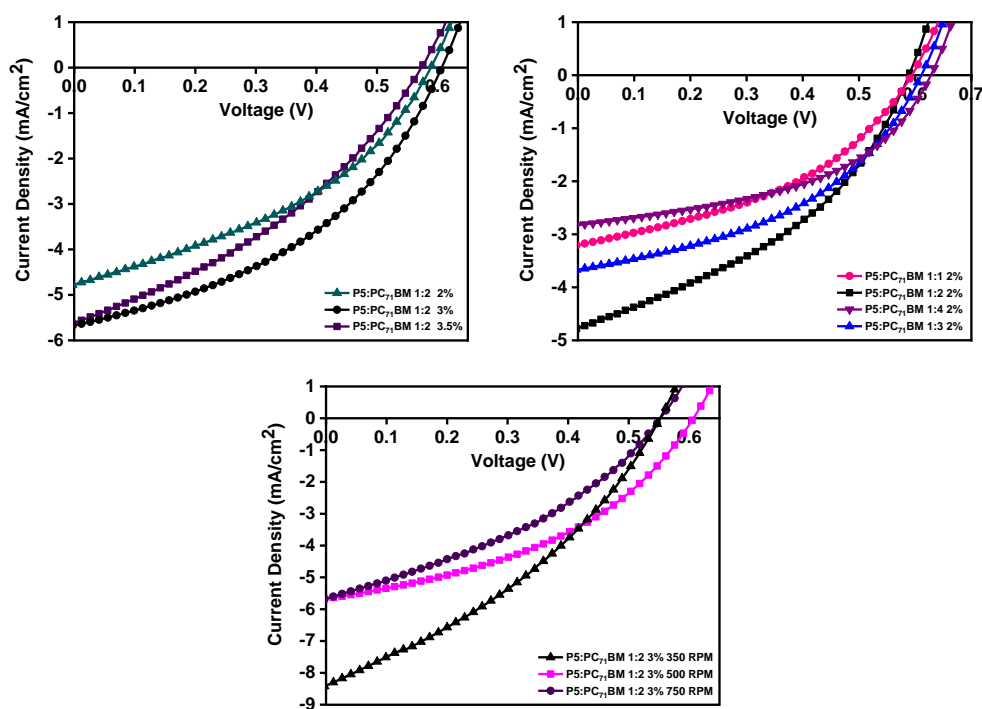


Figure 2.14. J-V curves that summarize the photovoltaic performance of **P5**

P1 and **P5** have alkyl chains at different positions. **P5** has a considerably lower M_n value than **P1** which was explained in section 2.4. When photovoltaic properties of **P1** and **P5** were compared, **P1** showed overwhelming superiority over **P5** at all the parameters. Starting with J_{sc} , the reason behind the superiority of **P1** could be from the high molecular weight. Low molecular weight causes poor absorption from incoming solar radiation. Also, wider fibrils of the polymer are formed due to excessive solubility of polymers which have low molecular weight. Wider fibrils reduce exciton diffusion which also reduces J_{sc} value (Li et al., 2014).

Also, decreased J_{sc} could be attributed to the alkyl group on thiophene which could cause a decrease in effective π -conjugation length due to disturbing in planarity at polymer backbone. From the electrochemical studies, **P1** and **P5** have similar HOMO levels but the V_{oc} values of the polymers are significantly different from each other which is surprising. V_{oc} levels should remain similar. Lower V_{oc} could be explained with less efficient charge transport property of **P5** which arises from poor active layer morphology. Which also explains the decreased FF value of **P5**.

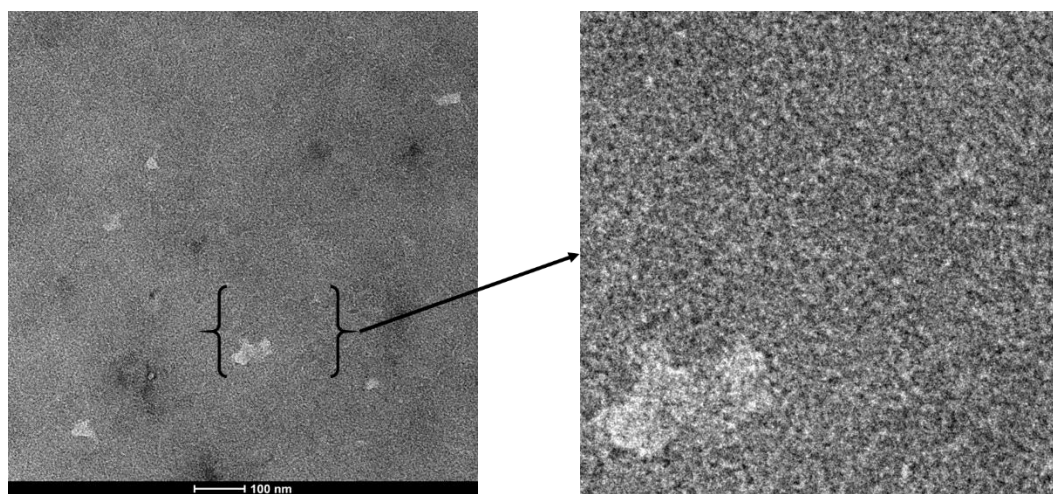


Figure 2.15. TEM images of P5: PC₇₁BM (1:2, w/w) blend

Figure 2.15. shows TEM images of P5: PC₇₁BM (1:2, w/w) blend with a scale of 50 and 100 nm respectively. While polymers are appearing as bright, PC₇₁BM appearing as dark regions. The images of the **P5** blend showed a moderately homogenous mixture with a lot of defects. The **P5** and PC₇₁BM poorly mixed in each other, aggregated PC₇₁BM domains as darker regions were observed. This could be explained by obtaining a low FF value. Also, thicker fibril formation was observed from TEM images due to the low molecular weight of **P5**. That could explain, obtaining a lower J_{sc} value than **P1** based device.

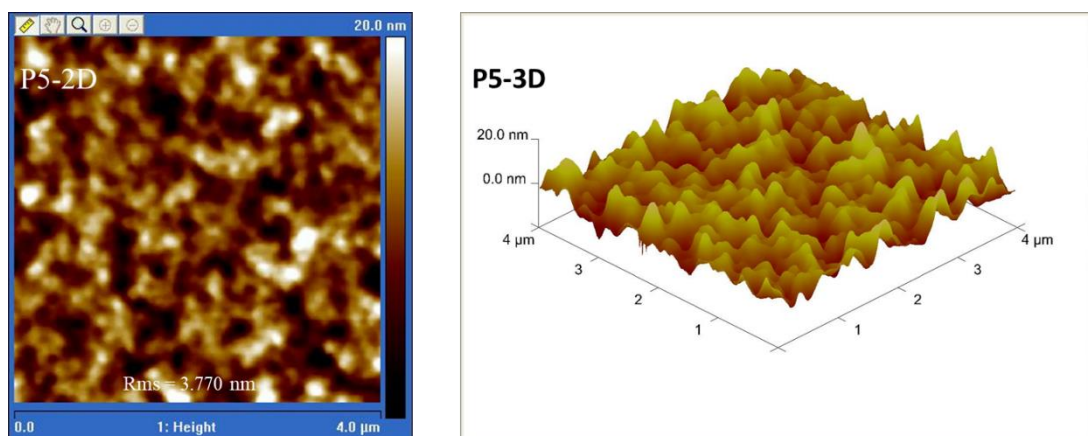


Figure 2.16. Topographic AFM images of P5: PC₇₁BM (1:2, w/w) blend

Figure 2.16. shows topographic AFM images of polymer blend **P5** with PC71BM. A rougher surface (3.770 nm) was observed when compared with **P1** (0.609 nm). Since FF values are directly correlated with the morphology of the active layer, a decreased FF value for **P5** was obtained when compared with **P1** as expected.

To summarize, although **P1** and **P5** have similar donor and acceptor units in their backbone, the difference between photovoltaic parameters is huge. Thus, the power conversion efficiency of **P5** is significantly lower than that of **P1**. This result could be clear evidence for the effect of the position of the alkyl chain on photovoltaic parameters.

2.8.4 P6

The energy level diagram of OSC which based on **P6** was illustrated in Figure 2.17. HOMO, LUMO and electronic band gap measurements were described in Section 2.6.

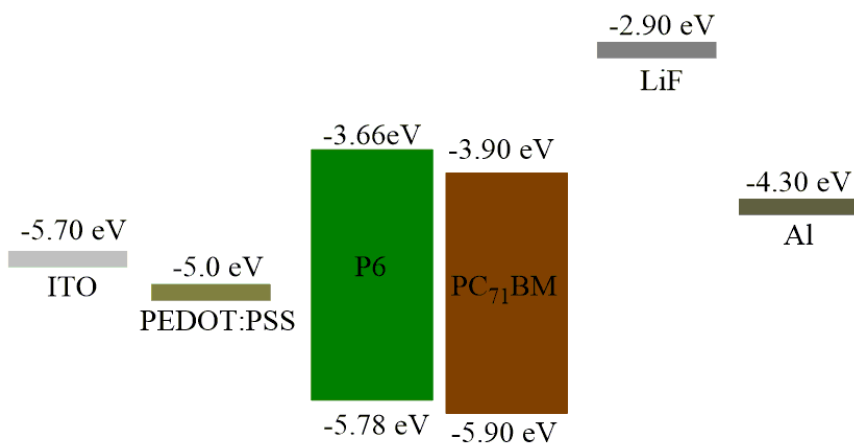


Figure 2.17. Energy level diagram of **P6** based OSC with conventional device architecture

Table 2.10 Summary of the photovoltaic properties for polymer **P6**

P6:PC ₇₁ BM (w:w)	J _{sc} (mA/cm ²)	V _{oc} (V)	FF (%)	η (%)	RPM
1:1 (2%)	7.30	0.72	55.89	2.89	750
1:2 (2%)	7.08	0.72	64.83	3.33	750
1:3 (2%)	8.19	0.72	64.07	3.78	750
1:4 (2%)	2.88	0.62	45.61	0.83	750
1:3 (3%)	8.41	0.73	63.70	3.89	750
1:3 (3.5%)	11.84	0.73	57.67	4.89	750

Exceeding the 1:3 ratio of P6: PC₇₁BM at 3% (w/v) causes a decrease in the J_{sc} value (Table 2.10). This could be explained by decreasing the polymer ratio in the blend. The absorption intensity of the active layer, which mostly belongs to the polymer due to the low absorptivity of PC₇₁BM towards AM1.5G, is generally responsible for the J_{sc} values. After, polymer:PC₇₁BM ratio optimization was completed, it is observed that the 1:3 ratio was the best among others. The ratio optimizations which were performed at 2% (w/v), was followed by blend concentration optimizations. In order to achieve enhanced current density values with increasing absorption of incoming radiation, blend concentration was increased. When the blend concentration was increased from 2% to 3%, the J_{sc} value increased from 8.19 mA/cm² to 8.41 mA/cm². Then, when the ratio was increased from 3% to 3.5%, again J_{sc} value was increased to 11.84 mA/cm² with overall device performance of 4.89% PCE. Hence optimum condition was determined in terms of blend concentration as 3.5%. As a future work, the thickness optimizations will be performed to obtain optimum parameters of the device.

For further optimization, three different additives will be added to the active layer which are DIO, DPE and CN in order to investigate the effects on overall device performance.

2.8.4.1 Addition of Gold NPs as an Additive

The effect of gold nanoparticles as an additive to the active layer in terms of photovoltaic properties were studied. Four devices based on **P6** as polymeric donor unit and PC₇₁BM as acceptor unit in the active layer of the cells were constructed simultaneously with the same parameters to minimize instrumental and personal errors and have an exact comparison. Gold NPs were simply mixed with the active layers of three out of four devices at different ratios which are 0.3%, 0.6% and 0.9% (w/w) and the device without gold NPs addition was used as the control group.

Table 2.11 Effect of addition of Au NPs on photovoltaic properties of **P6**

P6:PC ₇₁ BM Ratio	Weight	V _{oc} (V)	J _{sc} (mA cm ⁻²)	FF (%)	RPM	η (%)	Treatment
1:2	2%	0.58	6.14	65.06	750	2.89	-
1:2	2%	0.59	5.17	60.98	750	1.80	0.3% Au NPs
1:2	2%	0.57	4.67	61.98	750	1.65	0.6% Au NPs
1:2	2%	0.49	4.37	58.66	750	1.27	0.9% Au NPs

From the Table 2.11, significant decrease was observed after addition of Au NPs. The PCE of the devices was decreased with the increasing the concentration of Au NPs. The idea was promoting the absorption to increase J_{sc} value with utilization of nano-particles inside the active layer but the reverse situation was observed. J_{sc} values were decreased dramatically. The reason could be aggregation of NPs in the active layer. Further, morphology analysis will be performed to clarify the reasons behind performance decrease of the devices.

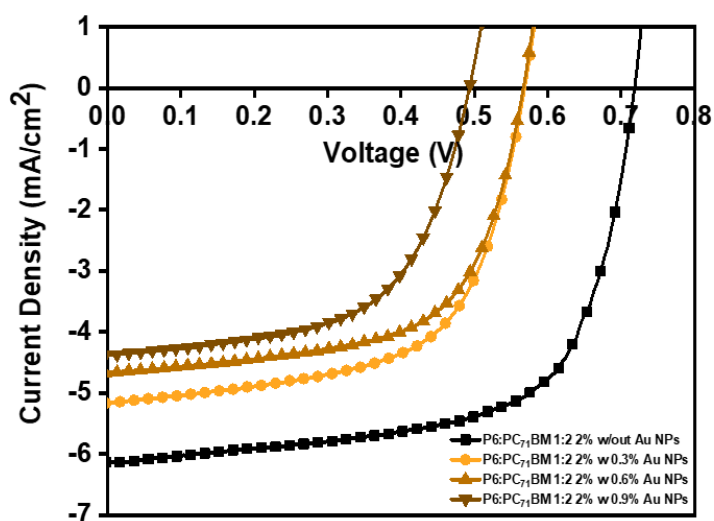


Figure 2.18. J-V curves of **P6** after Au NPs treatment with different concentrations

CHAPTER 3

EXPERIMENTAL

3.1 Materials

Chemicals were purchased from Merck, Tokyo Chemical Industry (TCI) and Solarmer. All reactions were carried out under a nitrogen atmosphere unless otherwise mentioned. Chloroform and chlorobenzene were dried over molecular sieves (4Å) and degassed with nitrogen for 2 days. Other dry solvents were obtained from a solvent drying system (Mbraun MBSPS5). Silica gel 60 was purchased from Merck (230-400 mesh) as a stationary phase for column chromatography. Thin-layer chromatography was performed with commercial 0.25 mm silica gel plates (TLC Merck Silica Gel 60).

3.2 Methods and Experimental

Bruker Spectrospin Avance DPX-400 MHz spectrometer was used to record the ^1H and ^{13}C -NMR spectra. As internal standard TMS (trimethylsilane) was used and chemical shifts are reported in parts per million (ppm). Coupling constants (J) were reported in hertz (Hz). Symbols: s(singlet), d(doublet), t(triplet), q(quartet) and m (multiplet) were used to specify the spin multiplicities. MestReNova software was used to process NMR spectra. Deuterated solvents CDCl_3 , MeOD and $(\text{CD}_3)_2\text{CO}$ were used as solvents for the analysis of ^1H and ^{13}C -NMR spectra. Exact masses of novel synthesized compounds were determined with high-resolution mass spectroscopy (Water Synapt MS System). Gel permeation chromatography (Shimadzu-20A) which is calibrated against polystyrene standard was performed to identify the molecular weight of synthesized polymers. Thermal properties of the polymers were identified by Pyris 1 TGA Thermogravimetry Analyzer and Perkin

Elmer Diamond DSC Differential Scanning Calorimeter. Redox behaviors and electronic band gaps of polymers were investigated by the cyclic voltammetry (CV) method. As a working electrode, Indium Tin Oxide (ITO) coated glass, as reference electrode (WE) silver and as counter electrode platinum were used. Grammy Instrument Reference 600 Potentiostat with a constant scan rate of 100 mV/s was used to investigate p- or n-type doping potentials. Varian Cary 5000 UV-Vis Spectrometer was used for spectroscopic studies. Lastly, the Keithley 2400 instrument was used to obtain current density vs voltage measurements. Photo-current was simulated with 100 mW cm² and measured under 1.5 G illumination.

3.3 Synthesis of Monomers

3.3.1 Synthesis of 1,2-dimethoxy-4,5-dinitrobenzene

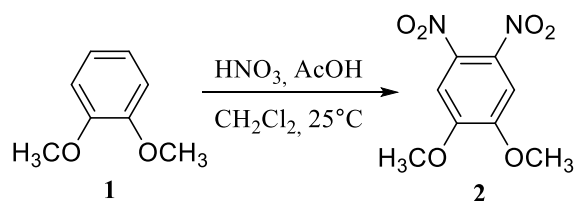


Figure 3.1. Synthetic route of compound **2**

In a 250 mL schlenk tube 9.66 g (70 mmol) veratrole (**1**), 50 mL DCM and 9.5 mL glacial acetic acid were added, then they were stirred in an ice bath until the temperature reached 0 °C. After that, 97.0% (fuming) nitric acid (26.6 mL) were added with the dropper around 1 hr. After the addition was completed, the reaction temperature was raised to room temperature and stirred for 24 hr. The resulting reddish-orange mixture was poured into the ice (around 400 mL) and extracted with DCM. The organic layer was washed with brine and dried over MgSO₄. After removing MgSO₄ by filtration, the solvent was evaporated under reduced pressure and a crude yellow-orange solid was obtained. To obtain a pure product,

recrystallization was performed with ethanol (EtOH). Yellow crystals were obtained (17.00 g, 90% yield).

^1H NMR (400 MHz, CDCl_3) δ 7.34 (s, 2H), 4.02 (s, $J = 6.0$ Hz, 6H).

^{13}C NMR (100 MHz, CDCl_3) δ 151.9, 136.7, 107.0, 57.1.

HR-MS (ESI) for $\text{C}_8\text{H}_9\text{N}_2\text{O}_6$, calculated 229.0461, found 229.0475

3.3.2 Synthesis of 5,6-dimethoxybenzo[*c*][1,2,5]oxadiazole

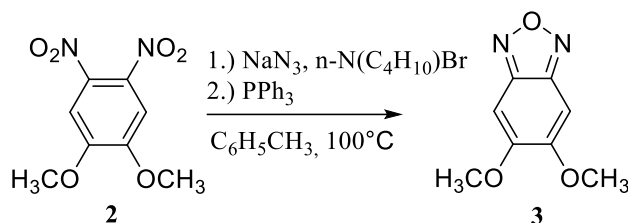


Figure 3.2. Synthetic route of compound **3**

The 2.80 g compound **2** (12 mmol), 3.00 g sodium azide (46 mmol) and 1.25 g tetrabutylammonium bromide (4 mmol) were added into a 250 mL schlenk tube and vacuumed for 30 min. to remove air and moisture. After that dry toluene (45 mL) were added to the schlenk tube under an N_2 atmosphere. The reaction temperature was set up to 110°C and stirred for 12 hr. During this process, the color of the reaction medium turned from yellow to red, then dark red. After TLC control 3.00 g triphenylphosphine (11 mmol) were added to the mixture and stirred for another 12 hr. under N_2 atmosphere at the same temperature. The reaction was concluded with TLC control and the reddish-black reaction medium was obtained. By decantation method, the salts were removed from the reaction medium and toluene was evaporated under reduced pressure. Crude black solid was dissolved in DCM and washed with brine several times. The organic layer was collected and dried over MgSO_4 . After removing MgSO_4 by filtration, DCM was evaporated by reduced pressure. The crude black solid was recrystallized with EtOH several times and dark yellow crystals were obtained (0.88 g, 40% yield).

^1H NMR (400 MHz, CDCl_3) δ 6.86 (s, 2H), 3.96 (s, $J = 13.0$ Hz, 6H).

^{13}C NMR (100 MHz, CDCl_3) δ 155.4, 146.7, 90.7, 56.6.

HR-MS (ESI) for $\text{C}_8\text{H}_9\text{N}_2\text{O}_3$, calculated 181.0613, found 181.0626

3.3.3 Synthesis of 4,7-dibromo-5,6-dimethoxybenzo[*c*][1,2,5]oxadiazole

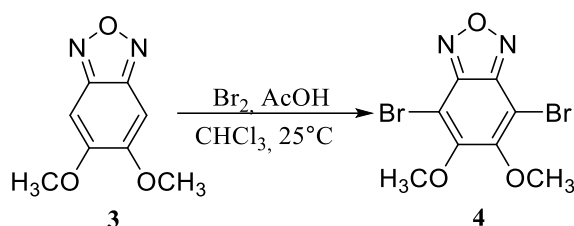


Figure 3.3. Synthetic route of compound 4

In a 250 mL schlenk tube 1.50 g (8 mmol) compound **3** and 80 mL CHCl_3 were added at room temperature and stirred. 0.90 mL bromine (18 mmol) and 10 mL acetic acid solution were added to the reaction mixture by dropper. The mixture was stirred for 3 days at room temperature under dark conditions. After TLC control, the reaction was finished. The free bromine was quenched by 20% NaOH solution and extraction was performed by CHCl_3 and brine. The organic layer was separated and dried over MgSO_4 . After filtrating MgSO_4 , the solvent was evaporated under reduced pressure. The yellowish-white crude solid was recrystallized with EtOH and pale-yellow crystals were obtained (2.20 g, 78% yield).

^1H NMR (400 MHz, CDCl_3) δ 4.03 (s, 6H).

^{13}C NMR (100 MHz, CDCl_3) δ 156.0, 147.4, 99.6, 61.7.

3.3.4 Synthesis of 4,7-dibromobenzo[*c*][1,2,5]oxadiazole-5,6-diol

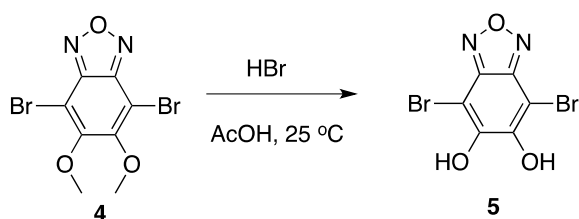


Figure 3.4. Synthetic route of compound **5**

The 0.70 g compound **4** (2 mmol) were placed into 100 mL, 2 neck reaction flask and 20 mL acetic acid added. The temperature was set to 50 °C and 7.00 mL fuming HBr were added dropwise by syringe. After the addition was completed, the reaction temperature was raised to 90 °C and stirred for 2 days. After that, the reaction mixture poured into the ice and the resulting precipitate was collected. The crude white solid was washed with water several times and dried in an oven at 60 °C. White solid was obtained (0.47 g, 73% yield).

^{13}C NMR (100 MHz, CD_3OD) δ 152.5, 147.9, 86.5.

3.3.5 Unsuccessful Trial of Synthesis of 4,7-dibromo-5,6-bis(octyloxy)benzo[*c*][1,2,5]oxadiazole

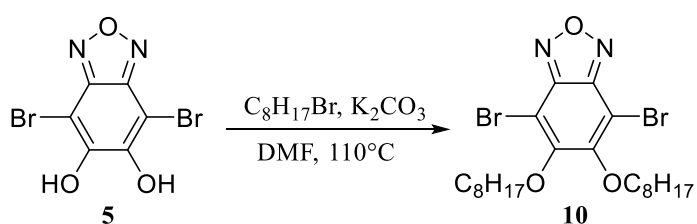


Figure 3.5. Unsuccessful synthetic trial of compound **10**

In a 250 mL schlenk tube, 0.40 g of compound **5** (1.29 mmol), 0.40 g of K_2CO_3 (2.84 mmol) and 25. mL of dry DMF were added. The reaction temperature was set to 80 °C. The mixture was stirred for 45 min. and 0.60 g 1-bromooctane (3.10 mmol) were added to the mixture. The temperature was raised to 110 °C and stirred 3 days under

an N₂ atmosphere. DMF was evaporated and extraction was performed with DCM and brine. The organic phase was collected and dried over MgSO₄ and the solvent was evaporated under reduced pressure. The crude milky liquid was collected. Column chromatography (silica gel, Hexane: DCM – 1:1) was performed to isolate the target compound. Due to the low yield, this method was abandoned.

3.3.6 Synthesis of 1,2-bis(octyloxy)benzene

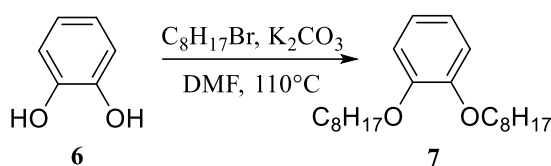


Figure 3.6. Synthetic route of compound **7**

In a 250 mL 2 neck reaction flask, 3.96 g of compound **6** (36.0 mmol), 13.0 g of K₂CO₃ (94.0 mmol), and 50 mL of dry DMF were added. The reaction temperature was set to 80 °C. The mixture was stirred for 45 min. and 14.10 g 1-bromooctane (75.0 mmol) were added to the mixture. The temperature was raised to 110 °C and stirred 3 days under an N₂ atmosphere. DMF was evaporated and extraction was performed with DCM and brine. The organic phase was collected and dried over MgSO₄. The solvent was evaporated under reduced pressure. The crude milky-brown liquid was collected. The target compound was precipitated in cold methanol (MeOH) and filtrated. White solid was obtained (10.35 g, 86% yield).

¹H NMR (400 MHz, CDCl₃) δ 6.81 (s, 4H), 3.93 (t, *J*=6.7 Hz, 4H), 1.73 (t, *J*=6.7 Hz, 4H), 1.46 – 1.14 (m, 20H), 0.81 (t, *J*=6.7 Hz, 6H).

¹³C NMR (100 MHz, CDCl₃) δ 149.2, 121.0, 114.1, 69.3, 31.9, 29.4, 29.4, 29.3, 26.1, 22.7, 14.1.

3.3.7 Synthesis of 1,2-dinitro-4,5-bis(octyloxy)benzene

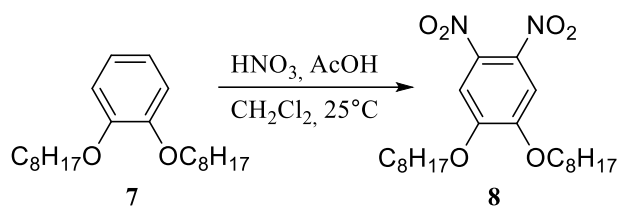


Figure 3.7. Synthetic route of compound **8**

In a 250 mL schlenk tube 3.00 g (8.97 mmol) compound **7**, 25 mL DCM and 10 mL glacial acetic acid were added, then they were stirred in an ice bath until the temperature reached 0 °C. After that, 97.0% (fuming) nitric acid (5.0 mL) were added with the dropper around 1 hr. After the addition was completed, the reaction temperature cooled to room temperature and stirred for 24 hr. The resulting reddish-orange mixture was poured into the ice (around 400 mL) and extracted with DCM. The organic layer was washed with brine and dried over MgSO₄. After removing MgSO₄ by filtration, the solvent was evaporated under reduced pressure and a crude yellow-orange solid was obtained. To obtain a pure product, recrystallization was performed with ethanol (EtOH). Yellow solids were obtained (3.20 g, 84% yield).

¹H NMR (400 MHz, CDCl₃) δ 7.27 (s, 2H), 4.11 (t, *J* = 6.3 Hz, 4H), 1.78 (m, 4H), 1.53 – 1.41 (m, 4H), 1.39 – 1.22 (m, 16H), 0.88 (t, *J* = 6.8 Hz, 6H).

¹³C NMR (100 MHz, CDCl₃) δ 151.8, 136.5, 107.9, 70.2, 31.8, 29.2, 28.7, 28.7, 25.8, 22.7, 14.1.

3.3.8 Synthesis of 5,6-bis(octyloxy)benzo[*c*][1,2,5]oxadiazole

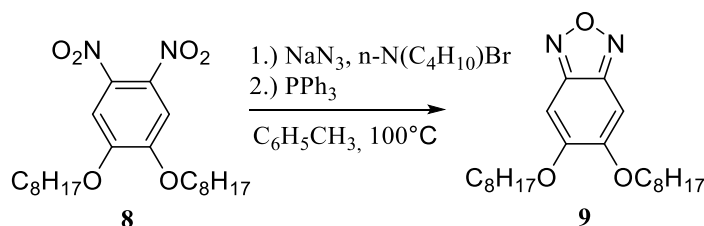


Figure 3.8. Synthetic route of compound **9**

The 1.50 g compound **8** (3.53 mmol), 2.20 g sodium azide (33.7 mmol) and 1.25 g tetrabutylammonium bromide (3.2 mmol) were added into a 150 mL schlenk tube and vacuumed for 30 min. to remove air and moisture. After that dried toluene (20 mL) were added to the schlenk tube under an N_2 atmosphere. The reaction temperature was set up to 110°C and stirred for 12 hr. During this process, the color of the reaction medium turned from yellow to red. After TLC control 1.00 g triphenylphosphine (3.67 mmol) were added to the mixture and stirred for another 12 hr. under N_2 atmosphere at the same temperature. The reaction was finished with TLC control and the dark red reaction medium was obtained. Salts were removed from the reaction medium by decantation method and toluene was evaporated under reduced pressure. The crude dark red solid was recrystallized in MeOH and a yellow solid was obtained (0.70 g, 53% yield).

^1H NMR (400 MHz, CDCl_3) δ 4.14 (t, $J = 6.6$ Hz, 4H), 2.00 – 1.72 (m, 4H), 1.56 – 1.44 (m, 4H), 1.40 – 1.25 (m, 16H), 0.89 (t, $J = 6.7$ Hz, 6H).

^{13}C NMR (100 MHz, CDCl_3) δ 155.7, 147.5, 99.6, 75.4, 31.8, 30.2, 29.3, 29.2, 25.9, 22.7, 14.1

3.3.9 Synthesis of 4,7-dibromo-5,6-bis(octyloxy)benzo[*c*][1,2,5]oxadiazole

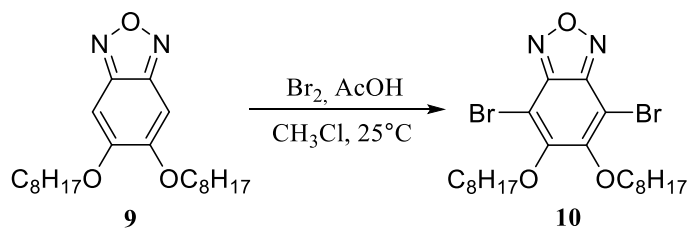


Figure 3.9. Synthetic route of compound **10**

In a 250 mL schlenk tube 1.00 g (2.66 mmol) compound **9** and 60 mL CHCl₃ were added and stirred at room temperature. 0.90 mL bromine (18 mmol) and 10 mL acetic acid solution were added to the mixture by dropper. The mixture was stirred for 3 days at room temperature under dark conditions. After TLC control, the reaction was finished. The free bromine was quenched with 20% NaOH solution and extraction was performed with CHCl₃ and brine. The organic phase was separated and dried by MgSO₄. After filtrating MgSO₄, the solvent was evaporated under reduced pressure. The yellowish-white crude liquid was precipitated in MeOH and a yellow-white solid was obtained (1.10 g, 78% yield).

¹H NMR (400 MHz, CDCl₃) δ 4.14 (t, *J* = 6.6 Hz, 4H), 2.00 – 1.72 (m, 4H), 1.56 – 1.44 (m, 4H), 1.40 – 1.25 (m, 16H), 0.89 (t, *J* = 6.7 Hz, 6H).

¹³C NMR (100 MHz, CDCl₃) δ 155.7, 147.5, 99.6, 75.4, 31.8, 30.2, 29.3, 29.2, 25.9, 22.7, 14.1.

3.3.10 Synthesis of tributyl(thiophen-2-yl)stannane

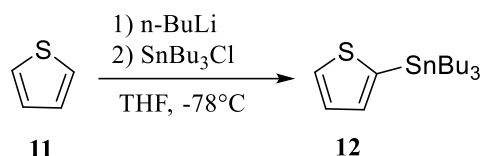


Figure 3.10. Synthetic route of compound **12**

5.00 g of compound **11** (59 mmol) were placed in 100 mL of schlenk tube and dissolved with 30 mL dry tetrahydrofuran (THF) under N₂ atmosphere. The reaction temperature was set up at -78°C. 26.15 mL of n-butyllithium (n-BuLi) (2.5 M in hexane 65 mmol) were added to the mixture dropwise around 40 min. After the addition was completed, the reaction stirred for 1 hr. at room temperature. The temperature then was set up at -78°C and 17.73 mL tributyl stannyl chloride (SnBu₃Cl) (65 mmol) were added dropwise. The mixture was stirred for 1 day at room temperature. The excess n-BuLi was quenched with distilled water and extraction was performed with brine and CHCl₃. The organic phase was collected and dried over MgSO₄. The solvent was evaporated under reduced pressure. The yellowish-transparent liquid was collected (17.00 g, 77% yield).

¹H NMR (400 MHz, CDCl₃): δ 7.58 (d, J=4.7 Hz, 1H), 7.19 (t, J= 3.3 Hz, 1H), 7.12 (d, J= 3.2 Hz, 1H), 1.50 (m, 6H), 1.28 (m, 6H), 1.03 (t, J= 8.4 Hz, 6H), 0.82 (t, J= 7.3 Hz, 9H).

3.3.11 Synthesis of 5,6-bis(octyloxy)-4,7-di(thiophen-2-yl)benzo[*c*][1,2,5]oxadiazole

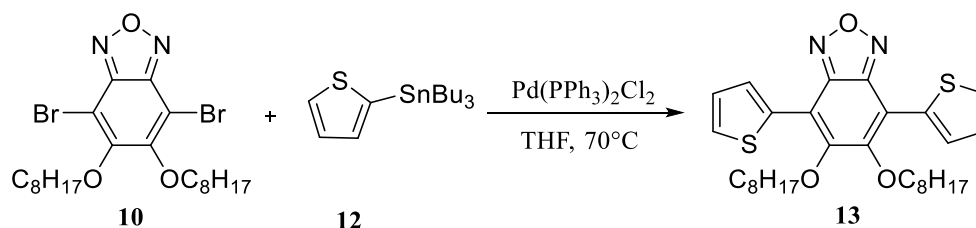


Figure 3.11. Synthetic route of compound **13**

In a 150 mL schlenk tube 0.60 g compound **10** (1.12 mmol) and 0.92 g compound, **12** (2.46 mmol) were added and vacuumed for 30 min to remove air and moisture. After that, 50 mL of dry THF were added under N₂ atmosphere and degassed for 30 min. 0.16 g PdCl₂(PPh₃)₂ were added quickly to the mixture and reaction temperature was set to 77 °C. The mixture was stirred for 1 day and finished with TLC control. After that, THF was removed under reduced pressure and the crude black liquid was obtained. Column chromatography (silica gel, Hexane: DCM – 5:1) was performed to isolate and purify molecule **13** which was orange solid (0.50 g, 82% yield).

¹H NMR (400 MHz, CDCl₃) δ 8.47 (dd, *J* = 3.8 Hz, 1.0 Hz, 2H), 7.50 (dd, *J* = 5.2 Hz, 1.0 Hz, 2H), 7.22 (dd, *J* = 5.1 Hz, 1.0 Hz, 2H), 4.15 (t, *J* = 7.3 Hz, 4H), 2.04 – 1.95 (m, 4H), 1.52 – 1.42 (m, 4H) 1.41 – 1.22 (m, 16H), 0.92 (t, *J* = 6.4 Hz, 6H).

¹³C NMR (100 MHz, CDCl₃) δ 151.2, 146.2, 134.3, 131.2, 130.1, 116.3, 112.7, 74.8, 31.8, 30.2, 29.5, 29.3, 25.8, 22.7, 14.1.

3.3.12 Synthesis of 4,7-bis(5-bromothiophen-2-yl)-5,6-bis(octyloxy)benzo[*c*][1,2,5]oxadiazole

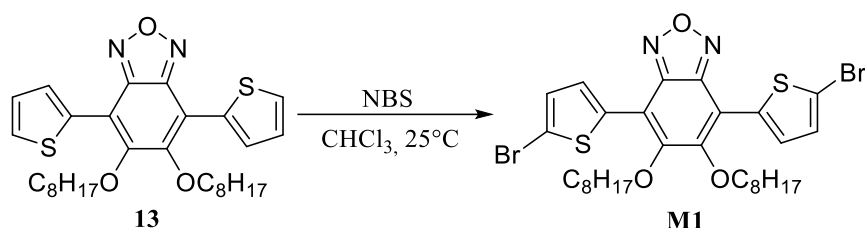


Figure 3.12. Synthetic route of compound **M1**

0.50 g compound **13** (0.90 mmol) were placed into a 250 mL schlenk tube and dissolved in 60 mL of dry CHCl_3 under an N_2 atmosphere. N-Bromosuccinimide 0.12 g (2.00 mmol) which were dissolved in 20 mL dry CHCl_3 under N_2 atmosphere were added dropwise to the reaction mixture by dropper around 20 min. After the addition was completed, the reaction mixture was stirred for 1 hr. at room temperature. Then the reaction was finished with TLC control and extraction was performed with CHCl_3 and brine. The organic phase was collected and dried over MgSO_4 . Reddish orange crude solid-liquid was obtained. Column chromatography (silica gel, Hexane: DCM – 6:1) was performed to isolate and purify **M1** which was reddish-orange solid (0.55 g, 85% yield).

^1H NMR (400 MHz, CDCl_3) δ 8.22 (d, $J = 4.1$ Hz, 2H), 7.15 (d, $J = 4.1$ Hz, 2H), 4.15 (t, $J = 7.3$ Hz, 4H), 2.15 – 1.89 (m, 4H), 1.52 – 1.20 (m, 20H), 0.90 (t, $J = 6.4$ Hz, 6H).

^{13}C NMR (100 MHz, CDCl_3) δ 151.2, 146.2, 134.3, 131.2, 130.1, 116.3, 112.7, 74.8, 31.8, 30.2, 29.5, 29.3, 25.8, 22.7, 14.1.

3.3.13 Synthesis of 5,6-dimethoxy-4,7-di(thiophen-2-yl)benzo[c][1,2,5]oxadiazole

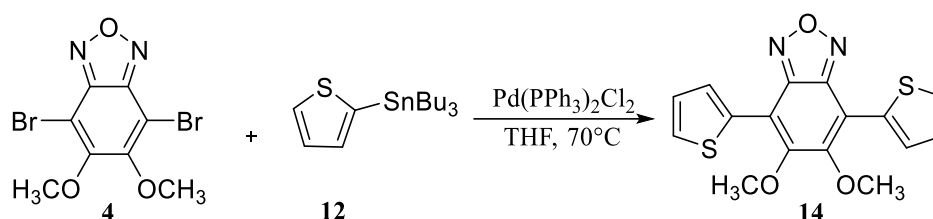


Figure 3.13. Synthetic route of compound **14**

In a 150 mL schlenk tube 1.00 g compound **4** (2.96 mmol) and 2.43 g compound, **12** (6.51 mmol) were added and vacuumed for 30 min to remove air and moisture. After that, 70 mL of dry THF were added under N₂ atmosphere and degassed for 30 min. 0.42 g PdCl₂(PPh₃)₂ (0.60 mmol) were added quickly to the mixture and reaction temperature was set to 77 °C. The mixture was stirred for 1 day and finished with TLC control. After that, THF was removed under reduced pressure and the crude black liquid was obtained. Column chromatography (silica gel, Hexane: DCM – 3:1) was performed to isolate and purify molecule **14** which was orange solid (0.75 g, 74% yield).

¹H NMR (400 MHz, CDCl₃) δ 8.51 (dd, *J* = 3.8, 0.9 Hz, 2H), 7.52 (dd, *J* = 5.2, 0.9 Hz, 2H), 7.23 (dd, *J* = 5.1, 3.9 Hz, 2H), 4.07 (s, 6H).

¹³C NMR (100 MHz, CDCl₃) δ 152.0, 146.5, 132.7, 131.0, 128.3, 127.3, 112.9, 60.5.

3.3.14 Synthesis of 4,7-bis(5-bromothiophen-2-yl)-5,6-bis(octyloxy)benzo[*c*][1,2,5]oxadiazole

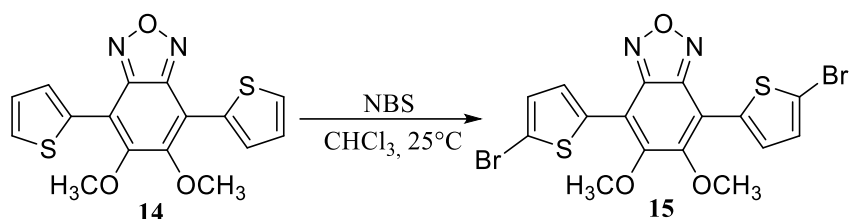


Figure 3.14. Synthetic route of compound **15**

0.75 g compound **14** (2.18 mmol) were placed into a 250 mL schlenk tube and dissolved with 60 mL of dry CHCl₃ under an N₂ atmosphere. N-Bromosuccinimide 0.85 g (4.79 mmol) which were dissolved in 20 mL dry CHCl₃ under N₂ atmosphere were added dropwise to the reaction mixture by dropper around 20 min. After the addition was completed, the reaction mixture was stirred for 1 hr. at room temperature. Then the reaction was finished with TLC control and extraction was performed with CHCl₃ and brine. The organic phase was collected and dried over MgSO₄. Orange crude solid-liquid was obtained. Column chromatography (silica gel, Hexane: DCM – 4:1) was performed to isolate and purify **15** which pale red solid. (0.66 g, 60% yield)

¹H NMR (400 MHz, CDCl₃) δ 8.26 (d, *J* = 4.2 Hz, 2H), 7.17 (d, *J* = 4.1 Hz, 2H), 4.07 (s, 6H).

¹³C NMR (100 MHz, CDCl₃) δ 151.6, 146.0, 134.1, 131.2, 130.2, 116.7, 112.5, 60.6.

3.3.15 Unsuccessful Trials of Synthesis of 4,7-bis(5-bromothiophen-2-yl)benzo[*c*][1,2,5]oxadiazole-5,6-diol

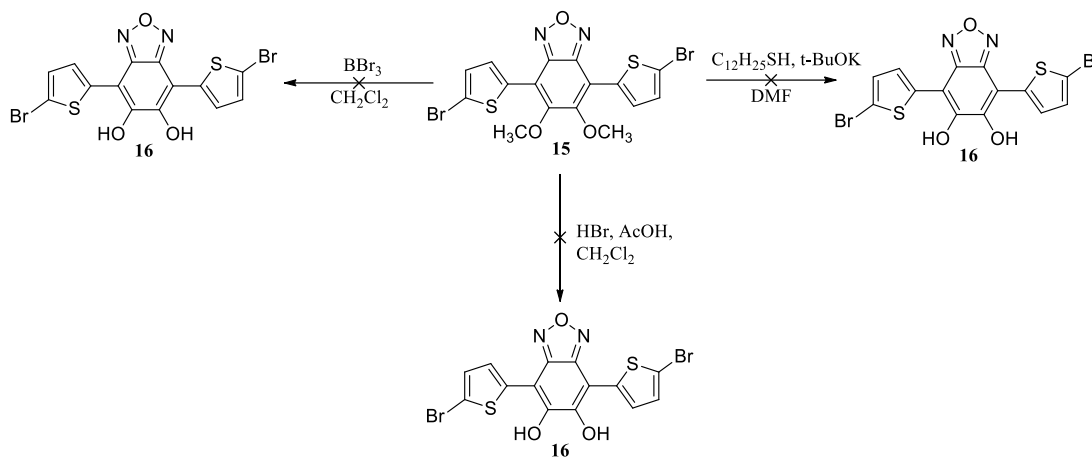


Figure 3.15. Unsuccessful trials to obtain product **16**

3.3.15.1 First Trial of Synthesis of 4,7-bis(5-bromothiophen-2-yl)benzo[*c*][1,2,5]oxadiazole-5,6-diol

0.20 g compound **15** (0.4 mmol) were placed into a 100 ml schlenk tube and dissolved with 20 ml dry DCM. The mixture was stirred until the temperature to reach 0 °C under N_2 atmosphere. 1 ml concentrated BBr_3 ($\geq 99.99\%$) was added dropwise to the reaction mixture. The reaction mixture was stirred for 1 day at room temperature. Due to significant color change from bright orange to dark red-black, the reaction was finished by quenching excess BBr_3 with the addition of distilled water dropwise. Extraction was performed with DCM and brine. The organic phase was collected and dried over MgSO_4 . The solvent was evaporated under reduced pressure. According to NMR spectroscopy of crude solid, the target molecule was not reached and the starting material was decomposed. The reaction was failed.

3.3.15.2 Second Trial of Synthesis of 4,7-bis(5-bromothiophen-2-yl)benzo[*c*][1,2,5]oxadiazole-5,6-diol

0.20 g compound **15** (0.4 mmol) and 0.1 g t-BuOK (0.89 mmol) were placed into 100 ml schlenk tube and they dissolved at 120°C with 25 ml DMF under N₂ atmosphere. After 15 min. 0.46 g 1-Dodecanethiol (3.2 mmol) were added. The mixture was stirred for 2 days. DMF was evaporated, then extraction was performed with DCM and brine. The organic phase was collected and dried over MgSO₄. The solvent was evaporated under reduced pressure. According to NMR spectroscopy of crude solid, the target molecule was not reached and the starting material was decomposed. The reaction was failed.

3.3.15.3 Third Trial of Synthesis of 4,7-bis(5-bromothiophen-2-yl)benzo[*c*][1,2,5]oxadiazole-5,6-diol

0.20 g compound **15** (0.4 mmol) were placed into 100 ml schlenk tube and dissolved with 20 ml acetic acid and 10 ml DCM. The reaction mixture was stirred 30 min. at 50°C. Then, 5 ml concentrated HBr were added dropwise to the reaction mixture. The temperature was raised to 50°C and stirred for 1 day. Extraction was performed with cold water and DCM. The organic phase was collected and dried over MgSO₄. The solvent was evaporated under reduced pressure. According to NMR spectroscopy of crude solid, the target molecule was not reached and the starting material was decomposed. The reaction was failed.

3.3.16 Synthesis of benzo[*c*][1,2,5]oxadiazole-5,6-diol

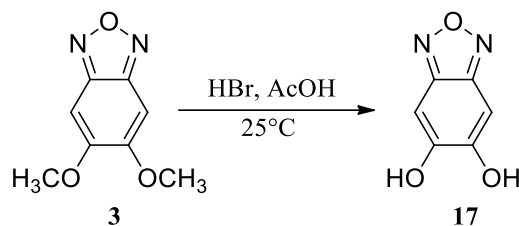


Figure 3.16. Synthetic route of compound **17**

The 0.95 g compound **3** (5.27 mmol) were placed into a 100 mL 2 neck reaction flask and 30 mL glacial acetic acid added. The temperature was set to 50 °C and 15.00 mL fuming HBr were added dropwise by syringe. After the addition was completed, the reaction temperature was raised to 90 °C and stirred for 2 days. After that, the reaction mixture was poured into the ice and extraction was performed with brine and ethyl acetate. The organic phase was collected and dried over MgSO₄ and the solvent was evaporated under reduced pressure. The crude dark brown solid was collected and washed with DCM several times. Brown solid was obtained (0.65 g, 82% yield).

¹H NMR (400 MHz, Acetone) δ 9.91 (s, 2H), 6.98 (s, 2H).

¹³C NMR (100 MHz, Acetone) δ 153.8, 148.0, 93.4

HR-MS (ESI) for C₆H₃N₂O₃, calculated 151.0144, found 151.0126

3.3.17 Synthesis of 5,6-bis((8-bromooctyl)oxy)benzo[*c*][1,2,5]oxadiazole

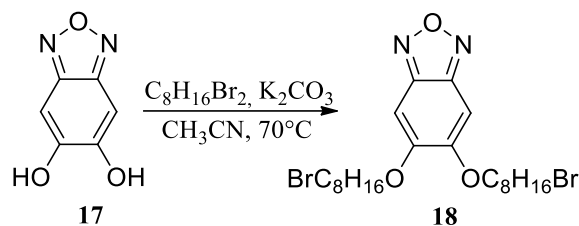


Figure 3.17. Synthetic route of compound **18**

In a 250 mL schlenk tube, 0.90 g of compound **17** (5.92 mmol), 3.27 g of K_2CO_3 (23.67 mmol) and 80. mL of dry acetonitrile (CH_3CN) were added. The reaction temperature was set to 80 °C. The mixture was stirred for 45 min. and 12.88 g 1,8-dibromooctane (47.33 mmol) were added to the mixture. The temperature was raised to 90 °C and stirred for 30 hr. under an N_2 atmosphere. CH_3CN was evaporated and extraction was performed with $CHCl_3$ and brine. The organic phase was collected and dried over $MgSO_4$ and the solvent was evaporated under reduced pressure. Crude yellow liquid was collected. The product was precipitated with cold hexane and washed several times. Yellowish white molecule **18** was collected (1.80 g, 57% yield).

1H NMR (400 MHz, $CDCl_3$) δ 6.80 (s, 2H), 4.06 (t, $J = 6.4$ Hz, 4H), 3.41 (t, $J = 6.8$ Hz, 4H), 1.93 – 1.82 (m, 8H), 1.55 – 1.34 (m, 16H).

^{13}C NMR (100 MHz, $CDCl_3$) δ 155.1, 146.8, 90.7, 69.3, 33.9, 32.7, 29.1, 28.7, 28.5, 28.1, 25.9.

HR-MS (ESI) for $C_{22}H_{35}N_2O_3Br_2$, calculated 535.0994, found 535.1021

3.3.18 Synthesis of 4,7-dibromo-5,6-bis((8-bromooctyl)oxy)benzo[*c*][1,2,5]oxadiazole

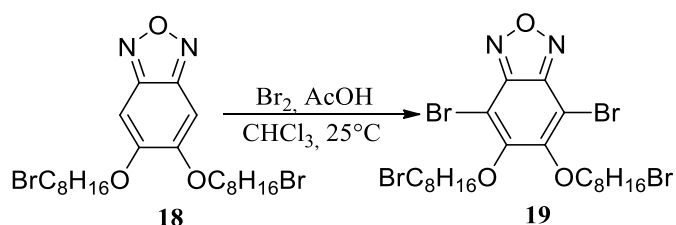


Figure 3.18. Synthetic route of compound **20**

In a 250 mL schlenk tube 1.00 g (1.87 mmol) compound **18** and 60 mL CHCl_3 were added and stirred at room temperature. 0.67 mL bromine (13.47 mmol) and 8 mL acetic acid solution were added to the mixture by dropper. The mixture was stirred for 3 days at room temperature under dark conditions. After TLC control, the reaction was finished. The free bromine was quenched with 20% sodium metabisulfite ($\text{Na}_2\text{S}_2\text{O}_5$) solution and extraction was performed with CHCl_3 and brine. The organic phase was separated and dried by MgSO_4 . After filtrating MgSO_4 , the solvent was evaporated under reduced pressure. The yellowish-white crude liquid was obtained. Column chromatography (silica gel, Hexane: CHCl_3 – 2:1) was performed to isolate and purify **19** which was white solid (1.15 g, 88% yield).

^1H NMR (400 MHz, CDCl_3) δ 4.08 (t, $J = 6.5$ Hz, 4H), 3.35 (t, $J = 6.8$ Hz, 4H), 1.84 – 1.76 (m, 8H), 1.50 – 1.30 (m, 16H).

^{13}C NMR (100 MHz, CDCl_3) δ 155.6, 147.4, 99.5, 75.3, 33.9, 32.7, 30.1, 29.2, 28.7, 28.1, 25.9.

HR-MS (ESI) for $\text{C}_{22}\text{H}_{33}\text{N}_2\text{O}_3\text{Br}_4$, calculated 692.9184, found 692.9007

3.3.19 Synthesis of 5,6-bis((8-bromooctyl)oxy)-4,7-di(thiophen-2-yl)benzo[*c*][1,2,5]oxadiazole

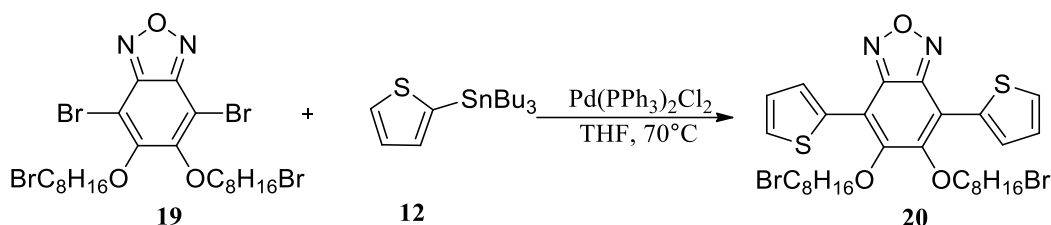


Figure 3.19. Synthetic route of compound **20**

In a 150 mL schlenk tube 0.84 g compound **19** (1.22 mmol) and 1.00 g compound, **12** (2.68 mmol) were added and vacuumed for 30 min. to remove air and moisture. After that, 70 mL of dry THF were added under N₂ atmosphere and degassed for 30 min. 0.17 g PdCl₂(PPh₃)₂ (0.24 mmol) were added quickly to the mixture and reaction temperature was set to 77 °C. The mixture was stirred for 1 day and finished with TLC control. After that, THF was removed under reduced pressure and the crude black-reddish liquid was obtained. Column chromatography (silica gel, Hexane: CHCl₃ – 4:1) was performed to isolate and purify molecule **20** which was orange solid (0.62 g, 73% yield).

¹H NMR (400 MHz, CDCl₃) δ 8.46 (dd, *J* = 3.8, 1.0 Hz, 2H), 7.51 (dd, *J* = 5.1, 1.0 Hz, 2H), 7.23 (dd, *J* = 5.1, 3.9 Hz, 2H), 4.15 (t, *J* = 7.3 Hz, 4H), 3.42 (t, *J* = 6.8 Hz, 4H), 2.04 – 1.95 (m, 4H), 1.91 – 1.83 (m, 4H), 1.49 – 1.35 (m, 16H).

¹³C NMR (100 MHz, CDCl₃) δ 150.6, 145.7, 131.8, 129.9, 127.0, 126.2, 112.1, 73.4, 32.9, 31.7, 29.2, 28.3, 27.7, 27.1, 24.7.

HR-MS (ESI) for C₃₀H₃₉N₂O₃S₂Br₂, calculated 699.0748, found 699.0813

3.3.20 Synthesis of 5,6-bis((8-bromooctyl)oxy)-4,7-bis(5-bromothiophen-2-yl)benzo[*c*][1,2,5]oxadiazole

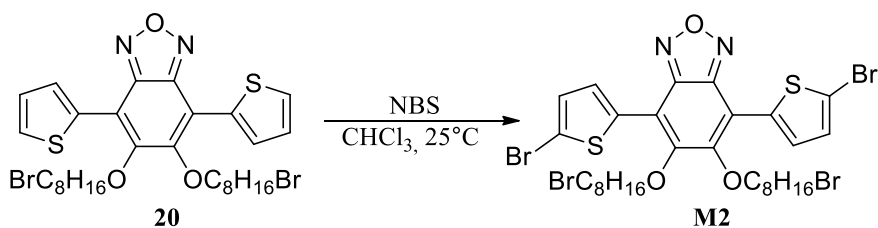


Figure 3.20. Synthetic route of compound **M2**

0.46 g compound **20** (0.65 mmol) were placed into a 250 mL schlenk tube and dissolved with 40 mL of dry CHCl_3 under an N_2 atmosphere. N-Bromosuccinimide 0.25 g (1.38 mmol) which were dissolved in 10 mL dry CHCl_3 under N_2 atmosphere were added dropwise to the reaction mixture by dropper around 20 min. After the addition was completed, the reaction mixture was stirred for 1 hr. at room temperature. Then the reaction was finished with TLC control and extraction was performed with CHCl_3 and brine. The organic phase was collected and dried over MgSO_4 . Orange crude solid-liquid was obtained. Column chromatography (silica gel, Hexane: CHCl_3 – 4:1) was performed to isolate and purify **M2** which pale red solid. (0.46 g, 81% yield)

^1H NMR (400 MHz, CDCl_3) δ 8.21 (d, $J = 3.9$ Hz, 2H), 7.15 (d, $J = 4.0$ Hz, 2H), 4.15 (t, $J = 7.3$ Hz, 4H), 3.42 (t, $J = 6.8$ Hz, 4H), 2.03 – 1.94 (m, 4H), 1.93 – 1.82 (m, 4H), 1.51 – 1.38 (m, 16H).

^{13}C NMR (100 MHz, CDCl_3) δ 150.1, 145.1, 133.1, 130.2, 129.0, 115.3, 111.6, 73.6, 32.9, 31.7, 29.1, 28.2, 27.7, 27.1, 24.7.

HR-MS (ESI) for $\text{C}_{30}\text{H}_{37}\text{N}_2\text{O}_3\text{S}_2\text{Br}_4$, calculated 856.8938, found 856.9152

3.3.21 Synthesis of trimethyl(4-hexylthiophen-2-yl)stannane

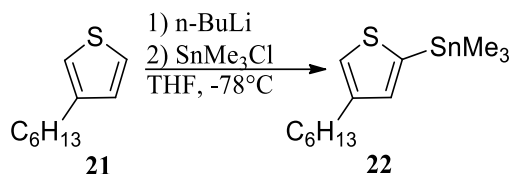


Figure 3.21. Synthetic route of compound **22**

1.00 g of compound **21** (5.94 mmol) were placed in 150 mL of schlenk tube and dissolved with 30 mL dry tetrahydrofuran (THF) under N₂ atmosphere. The reaction temperature was set up at -78°C. 2.61 mL of n-BuLi (2.5 M in hexane 6.54 mmol) were added to the mixture dropwise around 20 min. After the addition was completed, the reaction stirred for 1 hr. at room temperature. The temperature then was set up at -78°C and 7.13 mL trimethyl stannyl chloride (SnMe₃Cl) (7.13 mmol) were added dropwise. The mixture was stirred for 1 day at room temperature. The excess n-BuLi was quenched by distilled water and extraction was performed with brine and CHCl₃. The organic phase was collected and dried over MgSO₄. The solvent was evaporated under reduced pressure. The yellowish-transparent liquid was collected (1.71 g, 87% yield).

3.3.22 Synthesis of trimethyl(4-hexylthiophen-2-yl)stannane

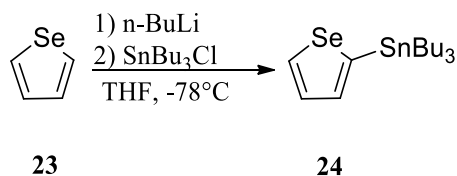


Figure 3.22. Synthetic route of compound **24**

5.00 g of compound **23** (38,16 mmol) were placed in 100 mL of schlenk tube and dissolved with 30 mL dry tetrahydrofuran (THF) under N₂ atmosphere. The reaction temperature was set up at -78°C. 18,32 mL of n-butyllithium (n-BuLi) (2.5 M in hexane 45,79 mmol) were added to mixture dropwise around 30 min. After the

addition was completed, the reaction stirred for 1 hr. at room temperature. The temperature then was set up at -78°C and 14.90 mL tributyl stannyl chloride (SnBu_3Cl) (45,79 mmol) were added dropwise. The mixture was stirred for 1 day at room temperature. The excess n-BuLi was quenched with distilled water and extraction was performed with brine and CHCl_3 . The organic phase was collected and dried over MgSO_4 . The solvent was evaporated under reduced pressure. The yellowish-transparent liquid was collected (12.20 g, 77,11% yield).

3.3.23 Synthesis of 4,7-bis(4-hexylthiophen-2-yl)-5,6-dimethoxybenzo[c][1,2,5]oxadiazole

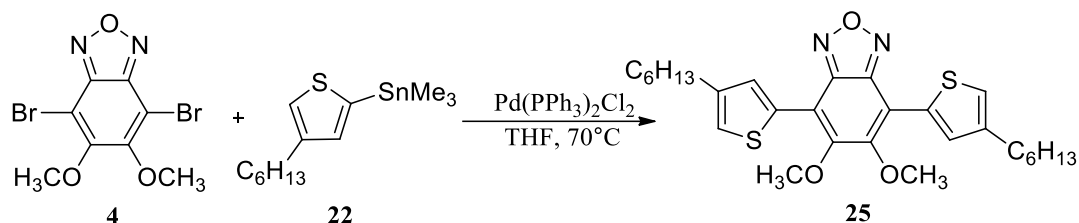


Figure 3.23. Synthetic route of compound **25**

In a 150 mL schlenk tube 0.61 g compound **4** (1.8 mmol) and 1.31 g compound, **22** (3.97 mmol) were added and vacuumed for 30 min to remove air and moisture. After that, 50 mL of dry THF were added under N_2 atmosphere and degassed for 30 min. 0.29 g $\text{PdCl}_2(\text{PPh}_3)_2$ (0.36 mmol) were added quickly to the mixture and reaction temperature was set to 70°C . The mixture was stirred for 1 day and finished with TLC control. After that, THF was removed under reduced pressure and the crude black-reddish liquid was obtained. Column chromatography (silica gel, Hexane: DCM – 4:1) was performed to isolate and purify molecule **25** which was yellow-orange solid. (0.58 g, 76% yield)

^1H NMR (400 MHz, CDCl_3) δ 8.34 (s, 2H), 7.11 (s, 2H), 4.05 (s, 6H), 2.71 (t, $J = 7.5$ Hz, 4H), 1.72 – 1.67 (m, 4H), 1.36 – 1.30 (m, 12H), 0.92 – 0.90 (m, 6H).

^{13}C NMR (100 MHz, CDCl_3) δ 152.5, 147.0, 144.0, 132.9, 132.7, 123.8, 113.24, 61.0, 32.2, 31.0, 29.5, 23.1, 14.6, 1.5.

HR-MS (ESI) for $\text{C}_{28}\text{H}_{36}\text{N}_2\text{O}_3\text{S}_2$, calculated 512.2167, found 512.2169

3.3.24 Synthesis of 5,6-bis(octyloxy)-4,7-di(selenophen-2-yl)benzo[*c*][1,2,5]oxadiazole

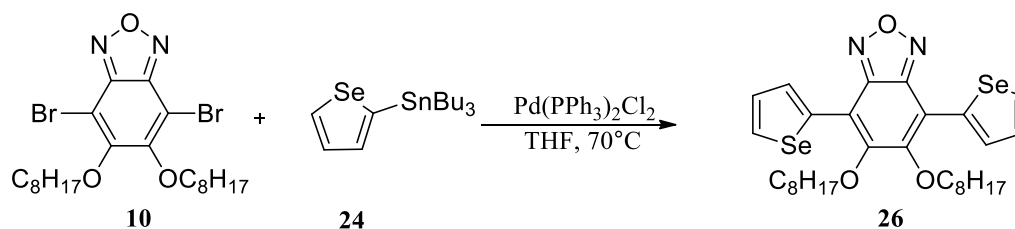


Figure 3.24. Synthetic route of compound **26**

In a 150 mL schlenk tube 0.62 g compound **10** (1.16 mmol) and 1.07 g compound, **24** (2.55 mmol) were added and vacuumed for 30 min to remove air and moisture. After that, 40 mL of dry THF were added under an N_2 atmosphere and degassed for 30 min. 0.16 g $\text{PdCl}_2(\text{PPh}_3)_2$ (0.23 mmol) were added quickly to the mixture and the reaction temperature was set to 70°C . The mixture was stirred for 1 day and finished with TLC control. After that, THF was removed under reduced pressure and the crude black-reddish liquid was obtained. Column chromatography (silica gel, Hexane: CHCl_3 – 5:1) was performed to isolate and purify molecule **26** which was red solid (0.52 g, 71% yield).

^1H NMR (400 MHz, CDCl_3) δ 8.77 (d, $J = 3.9$ Hz, 2H), 8.22 (d, $J = 5.7$ Hz, 2H), 7.49 (dd, $J = 5.7, 4.1$ Hz, 2H), 4.18 (t, $J = 7.4$ Hz, 4H), 2.04 (m, 4H), 1.48 – 1.43 (m, 4H), 1.41 – 1.27 (m, 20H), 0.91 (t, $J = 9.1$ Hz, 6H)

^{13}C NMR (100 MHz, CDCl_3) δ 151.4, 146.5, 136.6, 133.9, 133.3, 130.1, 115.4, 74.9, 32.0, 30.7, 29.7, 29.4, 26.0, 22.8, 14.3.

3.3.25 Synthesis of 4,7-bis(5-bromo-4-hexylthiophen-2-yl)-5,6-dimethoxybenzo[*c*][1,2,5]oxadiazole

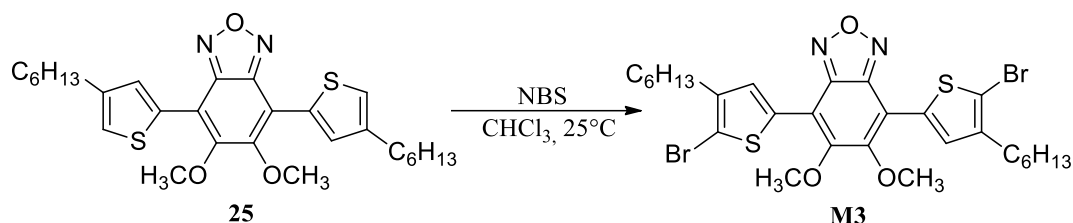


Figure 3.25. Synthetic route of compound **M3**

0.34 g compound **25** (0.66 mmol) were placed into a 150 mL schlenk tube and dissolved with 30 mL of dry CHCl_3 under an N_2 atmosphere. N-Bromosuccinimide 0.26 g (1.46 mmol) which were dissolved in 20 mL dry CHCl_3 under N_2 atmosphere were added dropwise to the reaction mixture by dropper around 20 min. After the addition was completed, the reaction mixture was stirred for 1 hr. at room temperature. Then the reaction was finished with TLC control and extraction was performed with CHCl_3 and brine. The organic phase was collected and dried over MgSO_4 . Red crude solid was obtained. Column chromatography (silica gel, Hexane: CHCl_3 – 4:1) was performed to isolate and purify **M3** which pale yellow-orange solid (0.30 g, 67% yield).

^1H NMR (400 MHz, CDCl_3) δ 8.21 (s, 2H), 4.05 (s, 6H), 2.64 (t, 4H), 1.69 – 1.62 (m, 4H), 1.41 – 1.32 (m, 12H), 0.90 (t, $J = 6.9$ Hz, 6H).

^{13}C NMR (100 MHz, CDCl_3) δ 152.1, 146.5, 142.9, 132.6, 132.2, 114.3, 112.8, 61.1, 32.1, 30.2, 30.1, 29.4, 23.1, 14.6.

HR-MS (ESI) for $\text{C}_{28}\text{H}_{34}\text{N}_2\text{O}_3\text{S}_2\text{Br}_2$, calculated 670.0357, found 670.0372

3.3.26 Synthesis of 4,7-bis(5-bromo-4-octylthiophen-2-yl)-5,6-dimethoxybenzo[*c*][1,2,5]oxadiazole

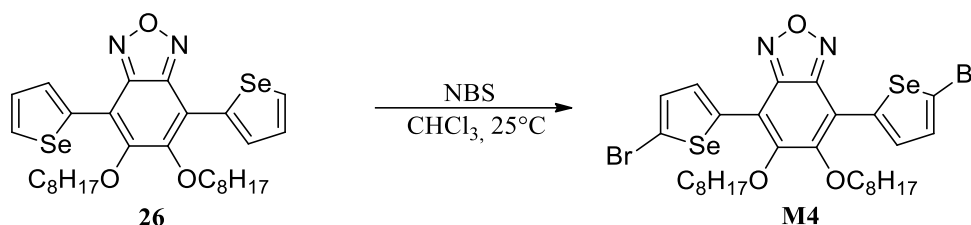


Figure 3.26. Synthetic route of compound **M4**

0.50 g compound **26** (0.79 mmol) were placed into a 250 mL schlenk tube and dissolved with 40 mL of dry CHCl_3 under an N_2 atmosphere. N-Bromosuccinimide 0.29 g (1.16 mmol) which were dissolved in 35 mL dry CHCl_3 under N_2 atmosphere were added dropwise to the reaction mixture by dropper around 30 min. After the addition was completed, the reaction mixture was stirred for 3 hr. at room temperature. Then the reaction was finished with TLC control and extraction was performed with CHCl_3 and brine. The organic phase was collected and dried over MgSO_4 . Red crude solid was obtained. Column chromatography (silica gel, Hexane: CHCl_3 – 5:1) was performed to isolate and purify **M4** which red solid (0.49 g, 79% yield).

^1H NMR (400 MHz, CDCl_3) δ 8.39 (d, $J = 4.4$ Hz, 2H), 7.32 (d, $J = 4.4$ Hz, 2H), 4.09 (t, $J = 7.5$ Hz, 4H), 1.97 – 1.89 (m, 4H), 1.40 – 1.20 (m, 20H), 0.83 (t, $J = 6.8$ Hz, 6H).

^{13}C NMR (100 MHz, CDCl_3) δ 150.9, 146.1, 138.1, 133.5, 133.2, 120.8, 114.8, 75.3, 31.9, 30.6, 29.6, 29.4, 25.9, 22.8, 14.23.

3.4 Synthesis of Polymers

3.4.1 Synthesis of P1

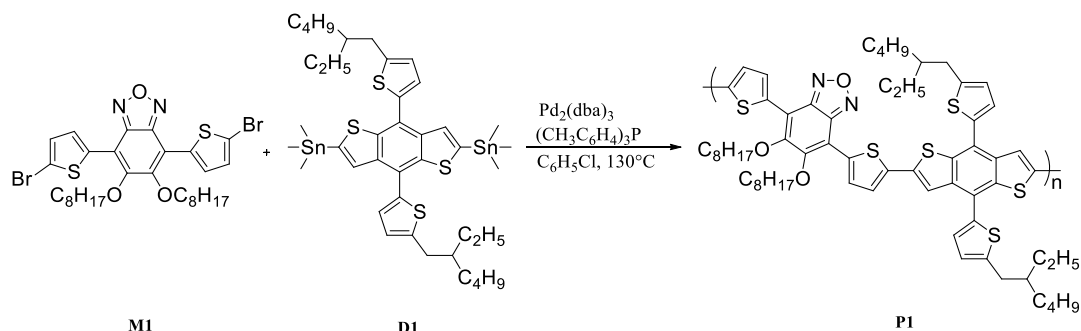


Figure 3.27. Synthetic route of **P1**

In a 25 mL schlenk tube 0.180 g **M1** ($257.67\mu\text{mol}$), 0.233 g **D1** ($257.67\mu\text{mol}$) and 6.30 mg tri(o-tolyl)phosphine ($(\text{CH}_3\text{C}_6\text{H}_4)_3\text{P}$) ($20.61\mu\text{mol}$) were added. Schlenk tube was vacuumed for 30 min. and then inert gas (N_2) allowed to pass through the schlenk tube to remove possible oxygen and humidity residues. This process was repeated 3 times. 6 mL of dry chlorobenzene ($\text{C}_6\text{H}_5\text{Cl}$) were added under N_2 atmosphere and mixture temperature was set to 60°C . The mixture was degassed for 1 h. Then 4.70 mg tris(dibenzylideneacetone)dipalladium(0) ($\text{Pd}_2(\text{dba})_3$) ($5.15\mu\text{mol}$) were added to reaction mixture and temperature raised to 130°C . The reaction was finished after 8 h. with TLC control. The reaction mixture was poured into the cold MeOH and precipitated. Then, 200 mg of palladium scavenger (3-(Diethylenetriamino)propyl-functionalized silica gel) were added and stirred for 1 h. The crude polymer was then filtrated and collected. The crude polymer was washed with Soxhlet apparatus with an order of methanol, acetone, hexane, chloroform and chlorobenzene solvents. Chlorobenzene fragment was collected. Chlorobenzene was evaporated under reduced pressure and **P1** collected (0.260 g, 88% yield).

GPC Result: $M_n = 224 \text{ kDa}$, $M_w = 538 \text{ kDa}$

3.4.2 Synthesis of P2

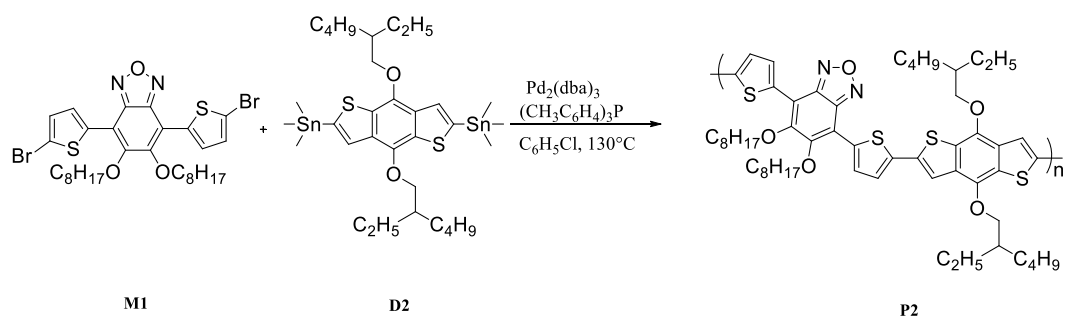


Figure 3.28. Synthetic route of **P2**

In a 25 mL schlenk tube 0.180 g **M2** ($257.67\mu mol$), 0.199 g **D2** ($257.67\mu mol$) and 6.30 mg tri(o-tolyl)phosphine ($(CH_3C_6H_4)_3P$) ($20.61\mu mol$) were added. Schlenk tube was vacuumed for 30 min. and then inert gas (N_2) allowed to pass through the schlenk tube to remove possible oxygen and humidity residues. This process was repeated 3 times. 6 mL of dry chlorobenzene (C_6H_5Cl) were added under N_2 atmosphere and mixture temperature was set to $60^\circ C$. The mixture was degassed for 1 hr. Then 4.70 mg tris(dibenzylideneacetone)dipalladium(0) ($Pd_2(dba)_3$) ($5.15\mu mol$) were added to reaction mixture and temperature raised to $130^\circ C$. The reaction was finished after 4 h. with TLC control. The reaction mixture was poured into the cold MeOH and precipitated. Then, 200 mg of palladium scavenger (3-(Diethylenetriamino)propyl-functionalized silica gel) were added and stirred for 1 hr. The crude polymer was then filtrated and collected. The crude polymer was washed with Soxhlet apparatus with an order of methanol, acetone, hexane, chloroform and chlorobenzene solvents. Chlorobenzene fragment was collected. Chlorobenzene was evaporated under reduced pressure and **P2** collected (0.220 g, 84% yield).

GPC Result: $M_n = 90$ kDa, $M_w = 385$ kDa

3.4.3 Synthesis of P3

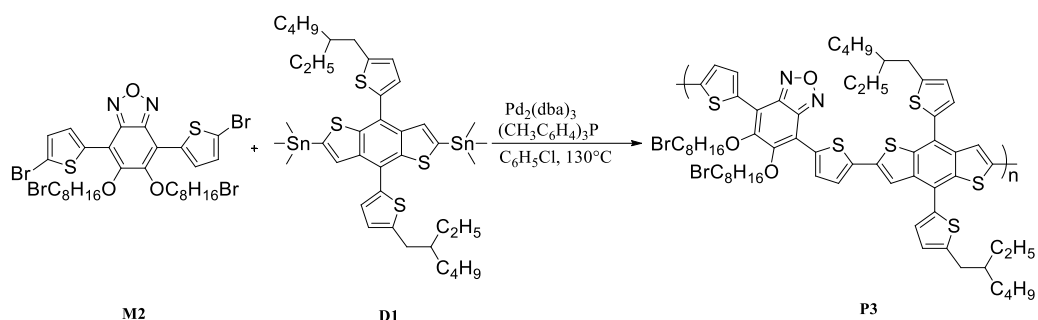


Figure 3.29. Synthetic route of **P3**

In a 25 mL schlenk tube 0.250 g **M1** (291.93 μ mol), 0.264 g **D2** (291.93 μ mol) and 7.10 mg tri(o-tolyl)phosphine ((CH₃C₆H₄)₃P) (23.35 μ mol) were added. Schlenk tube was vacuumed for 30 min. and then inert gas (N₂) allowed to pass through the schlenk tube to remove possible oxygen and humidity residues. This process was repeated 3 times. 8 mL of dry chlorobenzene (C₆H₅Cl) were added under N₂ atmosphere and mixture temperature was set to 60 °C. The mixture was degassed for 1 h. Then 5.30 mg tris(dibenzylideneacetone)dipalladium(0) (Pd₂(dba)₃) (5.84 μ mol) were added to reaction mixture and temperature raised to 130 °C. The reaction was finished after 150 min. with TLC control. The reaction mixture was poured into the cold MeOH and precipitated. Then, 200 mg of palladium scavenger (3-(Diethylenetriamino)propyl-functionalized silica gel) were added and stirred for 1 hr. The crude polymer was then filtrated and collected. The crude polymer was washed with Soxhlet apparatus with an order of methanol, acetone, hexane, chloroform and chlorobenzene solvents. Chlorobenzene fragment was collected. Chlorobenzene was evaporated under reduced pressure and **P3** collected (0.305 g, 80% yield).

GPC Result: Mn = 92 kDa, Mw = 310 kDa

3.4.4 Synthesis of P4

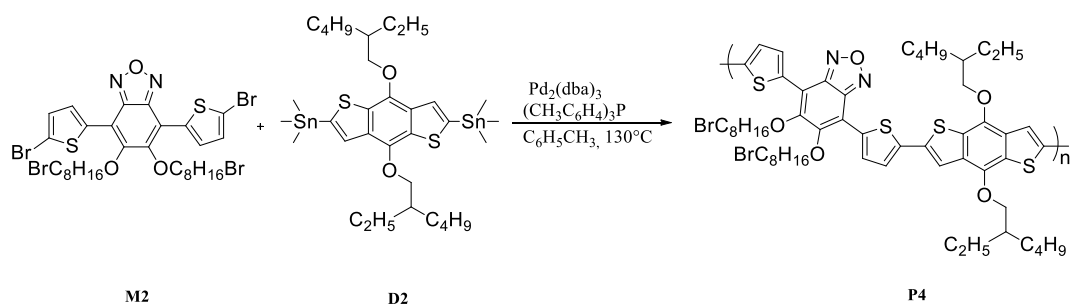


Figure 3.30. Synthetic route of **P4**

In a 25 mL schlenk tube 0.250 g **M2** (291.93 μmol), 0.225 g **D2** (291.93 μmol) and 7.10 mg tri(o-tolyl)phosphine ($(\text{CH}_3\text{C}_6\text{H}_4)_3\text{P}$) (23.35 μmol) were added. Schlenk tube was vacuumed for 30 min. and then inert gas (N_2) allowed to pass through the schlenk tube to remove possible oxygen and humidity residues. This process was repeated 3 times. 8 mL of dry toluene ($\text{C}_6\text{H}_5\text{CH}_3$) were added under N_2 atmosphere and mixture temperature was set to 60°C . The mixture was degassed for 1 hr. Then 5.30 mg tris(dibenzylideneacetone)dipalladium(0) ($\text{Pd}_2(\text{dba})_3$) (5.84 μmol) were added to reaction mixture and temperature raised to 100°C . The reaction was finished after 120 min. with TLC control. The reaction mixture was poured into the cold MeOH and precipitated. Then, 200 mg of palladium scavenger (3-(Diethylenetriamino)propyl-functionalized silica gel) were added and stirred for 1 h. The crude polymer was then filtrated and collected. The crude polymer was washed with Soxhlet apparatus with an order of methanol, acetone, hexane and chloroform solvents. Chloroform fragment was collected. Chloroform was evaporated under reduced pressure and **P4** collected (0.271 g, 85% yield).

GPC Result: $M_n = 75 \text{ kDa}$, $M_w = 270 \text{ kDa}$

3.4.5 Trials of Synthesis of P3-SH and P4-SH

3.4.5.1 Trial of Synthesis of P3-SH

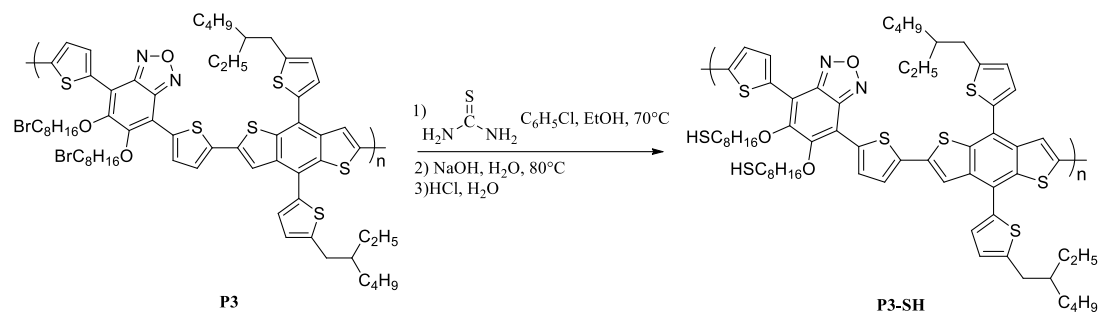


Figure 3.31. Trial of synthesis of **P3-SH**

0.150 g **P3** were placed into 150 mL of schlenk tube and dissolved with 40 mL dry chlorobenzene. 0.100 g thiourea (1.28 mmol) which were dissolved with 5 mL of EtOH were added dropwise into the solution of **P3**. The reaction mixture was stirred for 5 hr. at 70°C and the solvent of the reaction mixture were evaporated under reduced pressure. 20% 50 mL NaOH solution were added to schlenk tube and stirred vigorously 5 h. at 80°C . The reaction mixture was neutralized with 10% HCl addition in an ice bath. The resulting precipitate was collected and washed with cold water several times. Due to the solubility problem further, work-up was failed. Characterization of the final product was also failed due to the solubility problem.

3.4.5.2 Trial of Synthesis of P4-SH

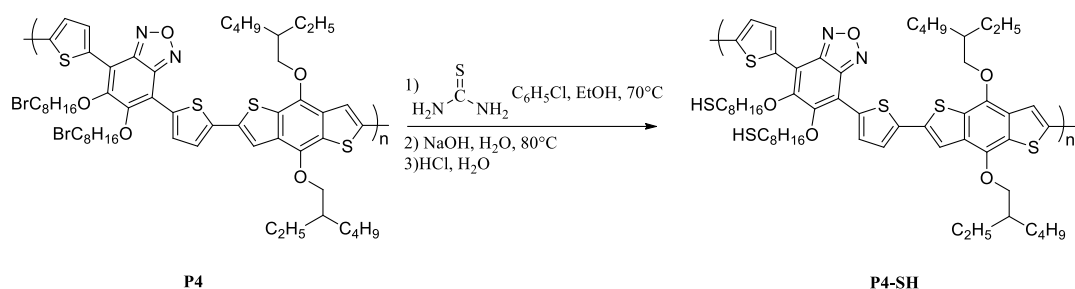


Figure 3.32. Trial of synthesis of **P4-SH**

0.150 g **P4** were placed into 150 mL of schlenk tube and dissolved with 40 mL dry THF. 0.100 g thiourea (1.28 mmol) which were dissolved with 5 mL of EtOH were added dropwise into the solution of **P4**. The reaction mixture was stirred 1 day at 70 °C and the solvent of the reaction mixture were evaporated under reduced pressure. 20% 50 mL NaOH solution were added to schlenk tube and stirred vigorously 8 h. at 80 °C. The reaction mixture was neutralized with 10% HCl addition in an ice bath. The resulting precipitate was collected and washed with cold water several times. Due to the solubility problem further, work-up was failed. Characterization of the final product was also failed due to the solubility problem.

3.4.6 Synthesis of P5

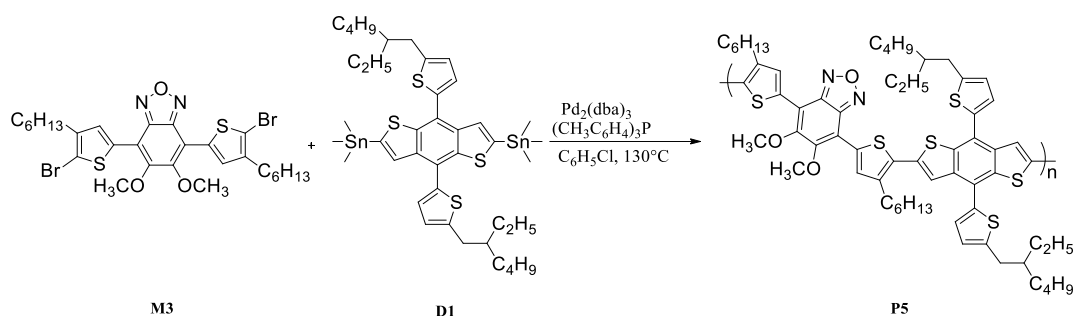


Figure 3.33. Synthetic route of **P5**

In a 25 mL schlenk tube 0.150 g **M3** (223.71 μmol), 0.202 g **D1** (223.71 μmol) and 5.50 mg tri(o-tolyl)phosphine ((CH₃C₆H₄)₃P) (17.90 μmol) were added. Schlenk tube was vacuumed for 30 min. and then inert gas (N₂) allowed to pass through the schlenk tube to remove possible oxygen and humidity residues. This process was repeated 3 times. 5 mL of dry chlorobenzene (C₆H₅Cl) were added under N₂ atmosphere and mixture temperature was set to 60 °C. The mixture was degassed for 1 h. Then 4.00 mg tris(dibenzylideneacetone)dipalladium(0) (Pd₂(dba)₃) (4.47 μmol) were added to reaction mixture and temperature raised to 130 °C. The reaction was finished after 8 h. with TLC control. The reaction mixture was poured into the cold MeOH and precipitated. Then, 200 mg of palladium scavenger (3-(Diethylenetriamino)propyl-functionalized silica gel) were added and stirred for 1 hr. The crude polymer was then filtrated and collected. The crude polymer was washed with Soxhlet apparatus with an order of methanol, acetone, hexane and chloroform solvents. Chloroform fragment was collected. Chloroform was evaporated under reduced pressure and **P5** collected (0.205 g, 80% yield).

GPC Result: Mn = 12 kDa, Mw = 16 kDa

3.4.7 Synthesis of P6

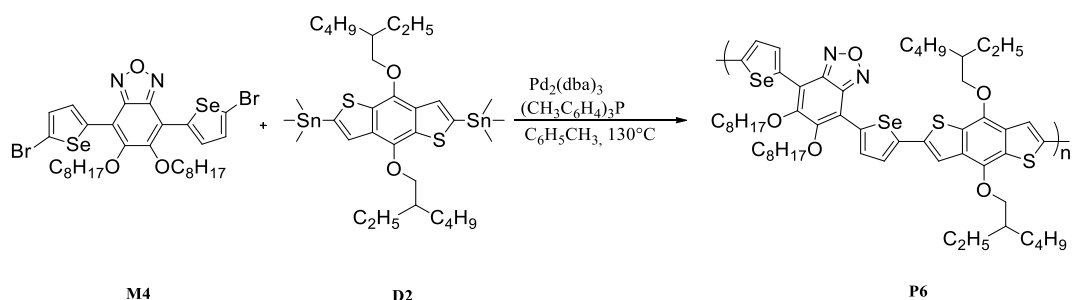


Figure 3.34. Synthetic route of **P6**

In a 25 mL schlenk tube 0.170 g **M4** (220.12 μmol), 0.174 g **D1** (220.12 μmol) and 6.70 mg tri(o-tolyl)phosphine ($(\text{CH}_3\text{C}_6\text{H}_4)_3\text{P}$) (22.01 μmol) were added. Schlenk tube was vacuumed for 30 min. and then inert gas (N_2) allowed to pass through the schlenk tube to remove possible oxygen and humidity residues. This process was repeated 3 times. 8 mL of dry toluene ($\text{C}_6\text{H}_5\text{CH}_3$) were added under N_2 atmosphere and mixture temperature was set to 60°C . The mixture was degassed for 1 h. Then 6.05 mg tris(dibenzylideneacetone)dipalladium(0) ($\text{Pd}_2(\text{dba})_3$) (6.60 μmol) were added to reaction mixture and temperature raised to 130°C . The reaction was finished after 100 min. with TLC control. The reaction mixture was poured into the cold MeOH and precipitated. Then, 200 mg of palladium scavenger (3-(Diethylenetriamino)propyl-functionalized silica gel) were added and stirred for 1 h. The crude polymer was then filtrated and collected. The crude polymer was washed with Soxhlet apparatus with an order of methanol, acetone, hexane and chloroform solvents. Chloroform fragment was collected. Chloroform was evaporated under reduced pressure and **P6** collected. (0.220 g, 88% yield)

GPC Result: $M_n = 66 \text{ kDa}$, $M_w = 200 \text{ kDa}$

3.5 Organic Solar Cell Device Fabrication of P1, P2, P3, P4, P5 and P6

3.5.1 General Procedure for Preparing Devices

Indium tin oxide (ITO) coated glass substrates should be cleaned and etched before device fabrication. Hydrochloric acid (HCl), (49%) nitric acid (HNO₃) (1%) and distilled water (50%) was mixed and ITO was etched by this mixture. They were cut with a size of 2.45 x 2.45 cm. After cutting and etching, ITO coated glass substrates were cleaned by solvents with an order of toluene, Hellmanex, distilled water and isopropyl alcohol in an ultrasonic bath for 15 min. As the last part of the cleaning process, oxygen plasma was applied for 5 min to ITO coated glass substrates in order to clean organic impurities and regulation of the work function of ITO coated glass substrates. After applying oxygen plasma, PEDOT:PSS was coated on the surface of ITO coated glass. This layer was coated at 4000 rpm speed for 30 seconds by a rotary coating device. PEDOT:PSS is a water-based material. The water content of PEDOT:PSS layer may affect the power conversion efficiency of the device, in order to prevent this, glass substrates were annealed at 135 °C for 15 min after coating PEDOT:PSS layer immediately. After this process, substrates were taken to the glove cabin system which was filled with inert N₂ gas in order to coat active layers of devices.

3.5.2 Procedures for Preparing Best Devices

3.5.2.1 The procedure of Preparing Best Device of P1

Polymer **P1**, PCBM was dissolved in the ortho-dichlorobenzene solvent and stirred for 16 hours at 70 °C to prepare an active layer solution. The mass of solution was 30 mg/mL and the ratio of donor-acceptor was 1:2. The active layer was coated at 600 rpm speed for 30 seconds. After the coating of the active layer, substrates were taken into a metal evaporator. LiF was coated with a thickness of 0.8 nm with an average speed of 0.3 Å/s under 2×10^{-7} mbar pressure. Also, Al was coated with a thickness of 100 nm with an average speed of 6 Å/s under the same pressure. Keithley 2400 instrument was used to obtain current density vs voltage measurements. Photo-current was simulated with 100 mW cm² and measured under 1.5 G illumination.

3.5.2.2 The procedure of Preparing Best Device for P2

Polymer **P2**, PCBM was dissolved in the ortho-dichlorobenzene solvent and stirred for 16 hours at 70 °C to prepare an active layer solution. Mass of solution was 30 mg/mL and the ratio of donor-acceptor was 1:2. The active layer was coated at 600 rpm speed for 30 second. After the coating of the active layer, substrates were taken into a metal evaporator. LiF was coated with a thickness of 0.8 nm with an average speed of 0.3 Å/s under 2×10^{-7} mbar pressure. Also, Al was coated with a thickness of 100 nm with an average speed of 6 Å/s under the same pressure. Keithley 2400 instrument was used to obtain current density vs voltage measurements. Photo-current was simulated with 100 mW cm² and measured under 1.5 G illumination.

3.5.2.3 The procedure of Preparing Best Device for P5

Polymer P5, PC₇₁BM was dissolved in the ortho-dichlorobenzene solvent and stirred for 16 hours at 70 °C to prepare an active layer solution. The mass of the solution was 30 mg/mL, and the ratio of donor-acceptor was 1:2. The active layer was coated at 350 rpm speed for 30 seconds. After the coating of the active layer, substrates were taken into a metal evaporator. LiF was coated with a thickness of 0.6 nm with an average speed of 0.3 Å/s under 2×10^{-7} mbar pressure. Also, Al was coated with a thickness of 100 nm with an average speed of 6 Å/s under the same pressure. Keithley 2400 instrument was used to obtain current density vs voltage measurements. Photo-current was simulated with 100 mW cm² and measured under 1.5 G illumination.

CHAPTER 4

CONCLUSION

Six different conjugated polymers as polymeric donor units for organic solar cells were synthesized. Four of them were new to the literature. To obtain those polymers, four different monomers and twenty-six different molecules were successfully synthesized. Their thermal, electrochemical, optical and photovoltaic properties were investigated. **P1** and **P2** which are already present in the literature were successfully re-synthesized with superior molecular weight when compared with literature analogs. Thermal properties of polymers confirmed that all polymers are thermally stable up to 305°C. As a result of electrochemistry experiments, all polymers showed ambipolar character. HOMO and LUMO levels of polymers were found as -5.43/-3.60, -5.53/-3.67, -5.45/-3.42, -5.67/-3.60, -5.46/-3.70 and -5.78/-3.66 respectively for **P1**, **P2**, **P3**, **P4**, **P5** and **P6**. The energy levels of them were found suitable for constructing organic solar cells. Optical band gaps of polymers were obtained from their thin-film absorption spectra and they were calculated as 1.81, 1.76, 1.74, 1.74, 1.72 and 1.71 respectively for **P1**, **P2**, **P3**, **P4**, **P5** and **P6**. Their photovoltaic properties were examined and best device performances in terms of PCE were found as 10.33% for **P1**, 6.43% for **P2**, 1.63% and for **P5**. Narrow fibril formation and homogenous morphology for **P1** and **P2** based devices were observed which resulted in an increase in PCE. A reverse situation was observed for **P5**, the wider formation of fibrils and non-uniform morphology with defects which resulted in a decrease in PCE.

Also, device optimizations for **P3**, **P4** and **P6** will be completed and post-polymerization which is converting the bromine group at the tip of the alkyl chain to thiol group will be performed. After thiol modification, insertion of surfactant-free gold NPs in the active layer of constructed devices will be performed to study the effect of gold-thiol interaction in terms of device morphology and efficiency.

REFERENCES

- Aldenderfer, M., Craig, N., Speakman, R., & Popelka-Filcoff, R. (2008). Supporting Information. *Aldenderfer, Mark S., Craig, Nathan M., Speakman, Robert Jeff, and Popelka-Filcoff, Rachel S.*, 1.
- Bao, Z., Chan, W., & Yu, L. (1993). Synthesis of Conjugated Polymer by the Stille Coupling Reaction. *Chemistry of Materials*, 5(1), 2–3. <https://doi.org/10.1021/cm00025a001>
- Beaujuge, P. M., Pisula, W., Hoi, N. T., Ellinger, S., Müllen, K., & Reynolds, J. R. (2009). Tailoring structure-property relationships in dithienosilole-benzothiadiazole donor-acceptor copolymers. *Journal of the American Chemical Society*, 131(22), 7514–7515. <https://doi.org/10.1021/ja900519k>
- Blouin, N., Michaud, A., Gendron, D., Wakim, S., Blair, E., Neagu-Plesu, R., Belletête, M., Durocher, G., Tao, Y., & Leclerc, M. (2008). Toward a rational design of poly(2,7-carbazole) derivatives for solar cells. *Journal of the American Chemical Society*, 130(2), 732–742. <https://doi.org/10.1021/ja0771989>
- Bouffard, J., & Swager, T. M. (2008). Fluorescent conjugated polymers that incorporate substituted 2,1,3-benzooxadiazole and 2,1,3-benzothiadiazole units. *Macromolecules*, 41(15), 5559–5562. <https://doi.org/10.1021/ma8010679>
- Braga, A. A. C., Ujaque, G., & Maseras, F. (2013). *Computational Perspective on Pd-Catalyzed*. 46(11). <https://doi.org/10.1021/ar400080r>
- Cho, C. H., Kim, H. J., Kang, H., Shin, T. J., & Kim, B. J. (2012). The effect of side-chain length on regioregular poly[3-(4-n-alkyl) phenylthiophene]/PCBM and ICBA polymer solar cells. *Journal of Materials Chemistry*, 22(28), 14236–14245. <https://doi.org/10.1039/c2jm31371e>

- Cho, S. W., Piper, L. F. J., Demasi, A., Preston, A. R. H., Smith, K. E., Chauhan, K. V., Sullivan, P., Hatton, R. A., & Jones, T. S. (2010). Electronic structure of C60/phthalocyanine/ITO interfaces studied using soft X-ray spectroscopies. *Journal of Physical Chemistry C*, *114*(4), 1928–1933. <https://doi.org/10.1021/jp910504a>
- Claverie, J. P., & Schaper, F. (2013). Ziegler-Natta catalysis: 50 years after the Nobel Prize. *MRS Bulletin*, *38*(3), 213–218. <https://doi.org/10.1557/mrs.2013.52>
- Cordovilla, C., Bartolomé, C., Martínez-Illarduya, J. M., & Espinet, P. (2015). The stille reaction, 38 years later. *ACS Catalysis*, *5*(5), 3040–3053. <https://doi.org/10.1021/acscatal.5b00448>
- Cuesta, V., Vartanian, M., Malhotra, P., Biswas, S., De La Cruz, P., Sharma, G. D., & Langa, F. (2019). Increase in efficiency on using selenophene instead of thiophene in π -bridges for D- π -DPP- π -D organic solar cells. *Journal of Materials Chemistry A*, *7*(19), 11886–11894. <https://doi.org/10.1039/c9ta02415h>
- Dunston, M. A. J., & Pattenden, G. (1999). The intramolecular stille reaction. *Journal of the Chemical Society - Perkin Transactions 1*, *10*, 1235–1246. <https://doi.org/10.1039/a808261h>
- Espinet, P., & Echavarren, A. M. (2004). The mechanisms of the Stille reaction. *Angewandte Chemie - International Edition*, *43*(36), 4704–4734. <https://doi.org/10.1002/anie.200300638>
- Feldman, D. (2008). Polymer history. *Designed Monomers and Polymers*, *11*(1), 1–15. <https://doi.org/10.1163/156855508X292383>
- Gedefaw, D., Tessarolo, M., Bolognesi, M., Prosa, M., Kroon, R., Zhuang, W., Henriksson, P., Bini, K., Wang, E., Muccini, M., Seri, M., & Andersson, M. R. (2016). Synthesis and characterization of benzodithiophene and benzotriazole-based polymers for photovoltaic applications. *Beilstein Journal of Organic Chemistry*, *12*, 1629–1637. <https://doi.org/10.3762/bjoc.12.160>

- Goker, S., Hizalan, G., Kutkan, S., Arslan Udum, Y., Cirpan, A., & Toppare, L. (2016). Incorporation of different conjugated linkers into low band gap polymers based on 5,6-Bis(octyloxy)-2,1,3 benzoxadiazole for tuning optoelectronic properties. *Journal of Polymer Science, Part A: Polymer Chemistry*, 54(16), 2459–2467. <https://doi.org/10.1002/pola.28141>
- Hafeez, H. Y., Iro, Z. S., Adam, B. I., & Mohammed, J. (2018). Fabrication and Characterization of Organic Photovoltaic Cell using Keithley 2400 SMU for efficient solar cell. *Journal of Physics: Conference Series*, 1000(1). <https://doi.org/10.1088/1742-6596/1000/1/012124>
- Harun, M. H., Saion, E., Kassim, A., Yahya, N., & Mahmud, E. (2007). Conjugated Conducting Polymers : A Brief Overview. *Sensors Peterborough NH*, 2(May 2016), 63–68. <http://sedaya.edu.my/jasa/2/papers/08I.pdf>
- Hau, S. K., Yip, H. L., & Jen, A. K. Y. (2010). A review on the development of the inverted polymer solar cell architecture. *Polymer Reviews*, 50(4), 474–510. <https://doi.org/10.1080/15583724.2010.515764>
- Heeger, A. J. (2010). Semiconducting polymers: The Third Generation. *Chemical Society Reviews*, 39(7), 2354–2371. <https://doi.org/10.1039/b914956m>
- Istanbulluoglu, C., Göker, S., Hizalan, G., Hacıoglu, S. O., Udum, Y. A., Yildiz, E. D., Cirpan, A., & Toppare, L. (2015). Synthesis of a benzotriazole bearing alternating copolymer for organic photovoltaic applications. *New Journal of Chemistry*, 39(8), 6623–6630. <https://doi.org/10.1039/c5nj01026h>
- Jenkins, A. D., Stepto, R. F. T., Kratochvíl, P., & Suter, U. W. (1996). Glossary of basic terms in polymer science (IUPAC Recommendations 1996). *Pure and Applied Chemistry*, 68(12), 2287–2311. <https://doi.org/10.1351/pac199668122287>
- Jiang, J. M., Raghunath, P., Lin, H. K., Lin, Y. C., Lin, M. C., & Wei, K. H. (2014). Location and number of selenium atoms in two-dimensional conjugated polymers affect their band-gap energies and photovoltaic performance. *Macromolecules*, 47(20), 7070–7080. <https://doi.org/10.1021/ma501720k>

- Jiang, J. M., Yang, P. A., Chen, H. C., & Wei, K. H. (2011). Synthesis, characterization, and photovoltaic properties of a low-bandgap copolymer based on 2,1,3-benzooxadiazole. *Chemical Communications*, 47(31), 8877–8879. <https://doi.org/10.1039/c1cc12040a>
- Kim, B., Yeom, H. R., Yun, M. H., Kim, J. Y., & Yang, C. (2012). to Lower of the Bandgap for Efficient Polymer Solar Cells. *Macromolecules*, 45, 8658–8664.
- Kosar, N., Ayub, K., & Mahmood, T. (2018). Accurate theoretical method for homolytic cleavage of C–Sn bond: A benchmark approach. *Computational and Theoretical Chemistry*, 1140, 134–144. <https://doi.org/10.1016/j.comptc.2018.08.003>
- Lei, T., Cao, Y., Zhou, X., Peng, Y., Bian, J., & Pei, J. (2012). Systematic investigation of isoindigo-based polymeric field-effect transistors: Design strategy and impact of polymer symmetry and backbone curvature. *Chemistry of Materials*, 24(10), 1762–1770. <https://doi.org/10.1021/cm300117x>
- Li, W., Hendriks, K. H., Furlan, A., Roelofs, W. S. C., Meskers, S. C. J., Wienk, M. M., & Janssen, R. A. J. (2014). Effect of the fibrillar microstructure on the efficiency of high molecular weight diketopyrrolopyrrole-based polymer solar cells. *Advanced Materials*, 26(10), 1565–1570. <https://doi.org/10.1002/adma.201304360>
- Liang, N., Jiang, W., Hou, J., & Wang, Z. (2017). New developments in non-fullerene small molecule acceptors for polymer solar cells. *Materials Chemistry Frontiers*, 1(7), 1291–1303. <https://doi.org/10.1039/c6qm00247a>
- Lin, C. F., Zhang, M., Liu, S. W., Chiu, T. L., & Lee, J. H. (2011). High photoelectric conversion efficiency of metal phthalocyanine/fullerene heterojunction photovoltaic device. *International Journal of Molecular Sciences*, 12(1), 476–505. <https://doi.org/10.3390/ijms12010476>
- Liu, B., Chen, X., He, Y., Li, Y., Xu, X., Xiao, L., Li, L., & Zou, Y. (2013). New alkylthienyl substituted benzo[1,2-b:4,5-b']dithiophene-based polymers for high performance solar cells. *Journal of Materials Chemistry A*, 1(3), 570–

577. <https://doi.org/10.1039/c2ta00474g>

Liu, J., Baek, J., Dai, L., Chemistry, A., & Reserve, C. W. (2021). Encyclopedia of Polymeric Nanomaterials. *Encyclopedia of Polymeric Nanomaterials*, 1–7. <https://doi.org/10.1007/978-3-642-36199-9>

Liu, L., Li, F., Wu, C., Tang, T., Chen, X., Luo, X., & Li, J. (2019). Synthesis and Properties of Benzodithiophene-Based Donor-Acceptor Metallo-Supramolecular Polymers. *Macromolecular Research*, 27(6), 534–542. <https://doi.org/10.1007/s13233-019-7076-6>

Liu, Y., Zhao, J., Li, Z., Mu, C., Ma, W., Hu, H., Jiang, K., Lin, H., Ade, H., & Yan, H. (2014). Aggregation and morphology control enables multiple cases of high-efficiency polymer solar cells. *Nature Communications*, 5(9), 1–8. <https://doi.org/10.1038/ncomms6293>

Lu, L., Xu, T., Chen, W., Landry, E. S., & Yu, L. (2014). Ternary blend polymer solar cells with enhanced power conversion efficiency. *Nature Photonics*, August, 1–7. <https://doi.org/10.1038/nphoton.2014.172>

Matsumura, S., Hlil, A. R., Lepiller, C., Gaudet, J., Guay, D., Shi, Z., Holdcroft, S., & Hay, A. S. (2008). Stability and Utility of Pyridyl Disulfide Functionality in RAFT and Conventional Radical Polymerizations. *Journal of Polymer Science: Part A: Polymer Chemistry*, 46, 7207–7224. <https://doi.org/10.1002/pola>

McDowell, C., Abdelsamie, M., Toney, M. F., & Bazan, G. C. (2018). Solvent Additives: Key Morphology-Directing Agents for Solution-Processed Organic Solar Cells. *Advanced Materials*, 30(33), 1–30. <https://doi.org/10.1002/adma.201707114>

Milstein, D., & Stille, J. K. (1979). Palladium-Catalyzed Coupling of Tetraorganotin Compounds with Aryl and Benzyl Halides. Synthetic Utility and Mechanism. *Journal of the American Chemical Society*, 101(17), 4992–4998. <https://doi.org/10.1021/ja00511a032>

Nicolaou, K. C., Bulger, P. G., & Sarlah, D. (2005). Palladium-catalyzed cross-coupling reactions in total synthesis. *Angewandte Chemie - International*

- Edition*, 44(29), 4442–4489. <https://doi.org/10.1002/anie.200500368>
- Paci, B., Spyropoulos, G. D., Generosi, A., Bailo, D., Albertini, V. R., Stratakis, E., & Kymakis, E. (2011). Enhanced structural stability and performance durability of bulk heterojunction photovoltaic devices incorporating metallic nanoparticles. *Advanced Functional Materials*, 21(18), 3573–3582. <https://doi.org/10.1002/adfm.201101047>
- Pässler, U., & Knölker, H. J. (2011). The Pyrrolo[2,1-a]isoquinoline Alkaloids. In *Alkaloids: Chemistry and Biology* (Vol. 70). <https://doi.org/10.1016/B978-0-12-391426-2.00002-5>
- Prima, D. O., Makarov, A. G., Bagryanskaya, I. Y., Kolesnikov, A. E., Zargarova, L. V., Baev, D. S., Eliseeva, T. F., Politanskaya, L. V., Makarov, A. Y., Slizhov, Y. G., & Zibarev, A. V. (2019). Fluorine-Containing n-6 and Angular and Linear n-6-n' (n, n' = 5, 6, 7) Diaza-Heterocyclic Scaffolds Assembled on Benzene Core in Unified Way. *ChemistrySelect*, 4(8), 2383–2386. <https://doi.org/10.1002/slct.201803970>
- Rodrigues, R., Meira, R., Ferreira, Q., Charas, A., & Morgado, J. (2014). Improving the efficiency of organic solar cells upon addition of polyvinylpyridine. *Materials*, 7(12), 8189–8196. <https://doi.org/10.3390/ma7128189>
- Scharber, M. C., & Sariciftci, N. S. (2013). Efficiency of bulk-heterojunction organic solar cells. *Progress in Polymer Science*, 38(12), 1929–1940. <https://doi.org/10.1016/j.progpolymsci.2013.05.001>
- Scharber, Markus C., Mühlbacher, D., Koppe, M., Denk, P., Waldauf, C., Heeger, A. J., & Brabec, C. J. (2006). Design rules for donors in bulk-heterojunction solar cells - Towards 10 % energy-conversion efficiency. *Advanced Materials*, 18(6), 789–794. <https://doi.org/10.1002/adma.200501717>
- Sekine, C., Tsubata, Y., Yamada, T., Kitano, M., & Doi, S. (2014). Recent progress of high performance polymer OLED and OPV materials for organic printed electronics. *Science and Technology of Advanced Materials*, 15(3). <https://doi.org/10.1088/1468-6996/15/3/034203>

- Shen, H., Bienstman, P., & Maes, B. (2009). Plasmonic absorption enhancement in organic solar cells with thin active layers. *Journal of Applied Physics*, *106*(7). <https://doi.org/10.1063/1.3243163>
- Shirakawa, H., Louis, E. J., MacDiarmid, A. G., Chiang, C. K., & Heeger, A. J. (1977). Synthesis of electrically conducting organic polymers: Halogen derivatives of polyacetylene, (CH)_x. *Journal of the Chemical Society, Chemical Communications*, *16*, 578–580. <https://doi.org/10.1039/C39770000578>
- Shopsowitz, K., Lelj, F., & MacLachlan, M. J. (2011). Regioselectivity in the nitration of dialkoxybenzenes. *Journal of Organic Chemistry*, *76*(5), 1285–1294. <https://doi.org/10.1021/jo102113t>
- Simon, J. J., Escoubas, L., Monestier, F., Torchio, P., & Flory, F. (2009). Optical properties engineering for Organic Solar Cells. *International Journal of Materials and Product Technology*, *34*(4), 469–487. <https://doi.org/10.1504/IJMPT.2009.025001>
- Spyropoulos, G. D., Stylianakis, M. M., Stratakis, E., & Kymakis, E. (2012). Organic bulk heterojunction photovoltaic devices with surfactant-free Au nanoparticles embedded in the active layer. *Applied Physics Letters*, *100*(21). <https://doi.org/10.1063/1.4720510>
- Sun, Y., Lin, B., Yang, H., & Gong, X. (2012). Improved bulk-heterojunction polymer solar cell performance through optimization of the linker group in donor-acceptor conjugated polymer. *Polymer*, *53*(7), 1535–1542. <https://doi.org/10.1016/j.polymer.2012.02.007>
- Uddin, M. A., Chan, H. P., & Rahman, B. M. A. (2010). Structural improvement of organic photovoltaic cell (OPVC) towards higher efficiency. *Reviews on Advanced Materials Science*, *26*(1–2), 58–66.
- Vikse, K., Naka, T., McIndoe, J. S., Besora, M., & Maseras, F. (2013). Oxidative additions of aryl halides to palladium proceed through the monoligated complex. *ChemCatChem*, *5*(12), 3604–3609.

<https://doi.org/10.1002/cctc.201300723>

- Vohra, V., Kawashima, K., Kakara, T., Koganezawa, T., Osaka, I., Takimiya, K., & Murata, H. (2015). Efficient inverted polymer solar cells employing favourable molecular orientation. *Nature Photonics*, 9(6), 403–408. <https://doi.org/10.1038/nphoton.2015.84>
- Wang, D. H., Park, K. H., Seo, J. H., Seifert, J., Jeon, J. H., Kim, J. K., Park, J. H., Park, O. O., & Heeger, A. J. (2011). Enhanced power conversion efficiency in PCDTBT/PC 70 BM bulk heterojunction photovoltaic devices with embedded silver nanoparticle clusters. *Advanced Energy Materials*, 1(5), 766–770. <https://doi.org/10.1002/aenm.201100347>
- Xu, X., Bi, Z., Ma, W., Wang, Z., Choy, W. C. H., Wu, W., Zhang, G., Li, Y., & Peng, Q. (2017). Highly Efficient Ternary-Blend Polymer Solar Cells Enabled by a Nonfullerene Acceptor and Two Polymer Donors with a Broad Composition Tolerance. *Advanced Materials*, 29(46), 1–8. <https://doi.org/10.1002/adma.201704271>
- Xue, M., Li, L., Tremolet De Villers, B. J., Shen, H., Zhu, J., Yu, Z., Stieg, A. Z., Pei, Q., Schwartz, B. J., & Wang, K. L. (2011). Charge-carrier dynamics in hybrid plasmonic organic solar cells with Ag nanoparticles. *Applied Physics Letters*, 98(25), 13–16. <https://doi.org/10.1063/1.3601742>
- Yang, T., Wang, M., Duan, C., Hu, X., Huang, L., Peng, J., Huang, F., & Gong, X. (2012). Inverted polymer solar cells with 8.4% efficiency by conjugated polyelectrolyte. *Energy and Environmental Science*, 5(8), 8208–8214. <https://doi.org/10.1039/c2ee22296e>
- Yu, S., Frisch, J., Opitz, A., Cohen, E., Bendikov, M., Koch, N., & Salzmann, I. (2015). Effect of molecular electrical doping on polyfuran based photovoltaic cells. *Applied Physics Letters*, 106(20), 1–6. <https://doi.org/10.1063/1.4921484>
- Yuan, M., Yang, P., Durban, M. M., & Luscombe, C. K. (2012). Low bandgap polymers based on silafluorene containing multifused heptacyclic arenes for photovoltaic applications. *Macromolecules*, 45(15), 5934–5940. <https://doi.org/10.1021/ma300839c>

- Yue, W., Huang, X., Yuan, J., Ma, W., Krebs, F. C., & Yu, D. (2013). A novel benzodipyrrolidone-based low band gap polymer for organic solar cells. *Journal of Materials Chemistry A*, *1*(35), 10116–10119. <https://doi.org/10.1039/c3ta12701j>
- Zhang, Z. G., & Wang, J. (2012). Structures and properties of conjugated Donor-Acceptor copolymers for solar cell applications. *Journal of Materials Chemistry*, *22*(10), 4178–4187. <https://doi.org/10.1039/c2jm14951f>
- Zhao, J., Li, Y., Hunt, A., Zhang, J., Yao, H., Li, Z., Zhang, J., Huang, F., Ade, H., & Yan, H. (2016). A Difluorobenzoxadiazole Building Block for Efficient Polymer Solar Cells. *Advanced Materials*, *28*(9), 1868–1873. <https://doi.org/10.1002/adma.201504611>

APPENDICES

A. Spectra

Bruker Spectrospin Avance DPX-400 Spectrometer was used to analysis for each compound. As internal standard, TMS and deuterated solvents CDCl_3 , CD_3OD and $(\text{CD}_3)_2\text{CO}$ were used.

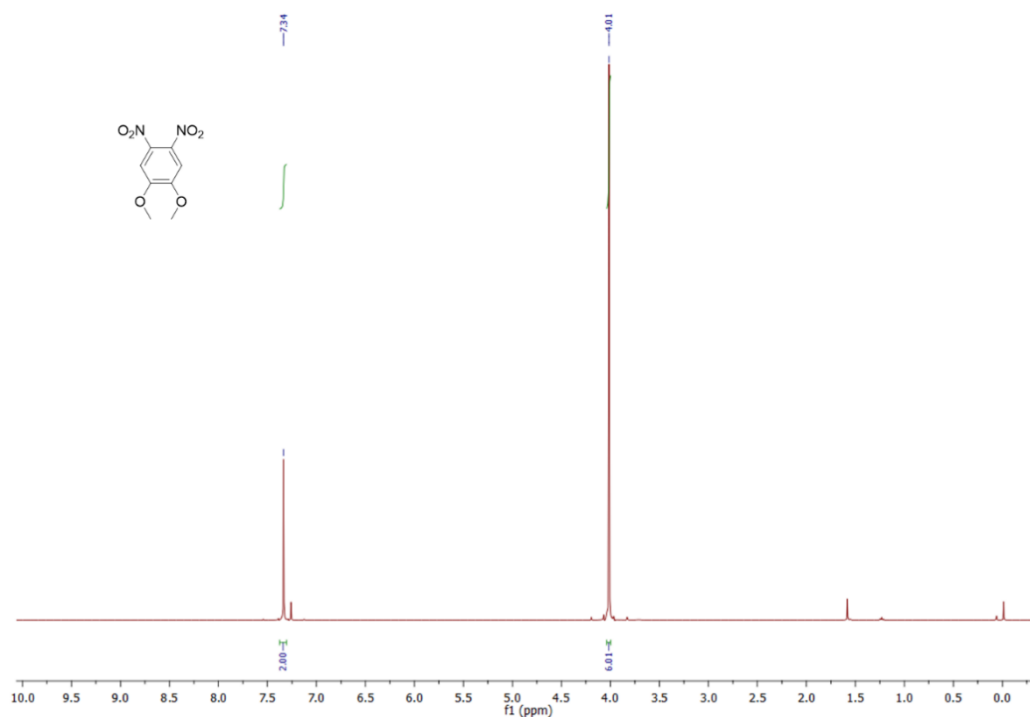


Figure A.1. ^1H NMR spectrum of compound **2** in CDCl_3

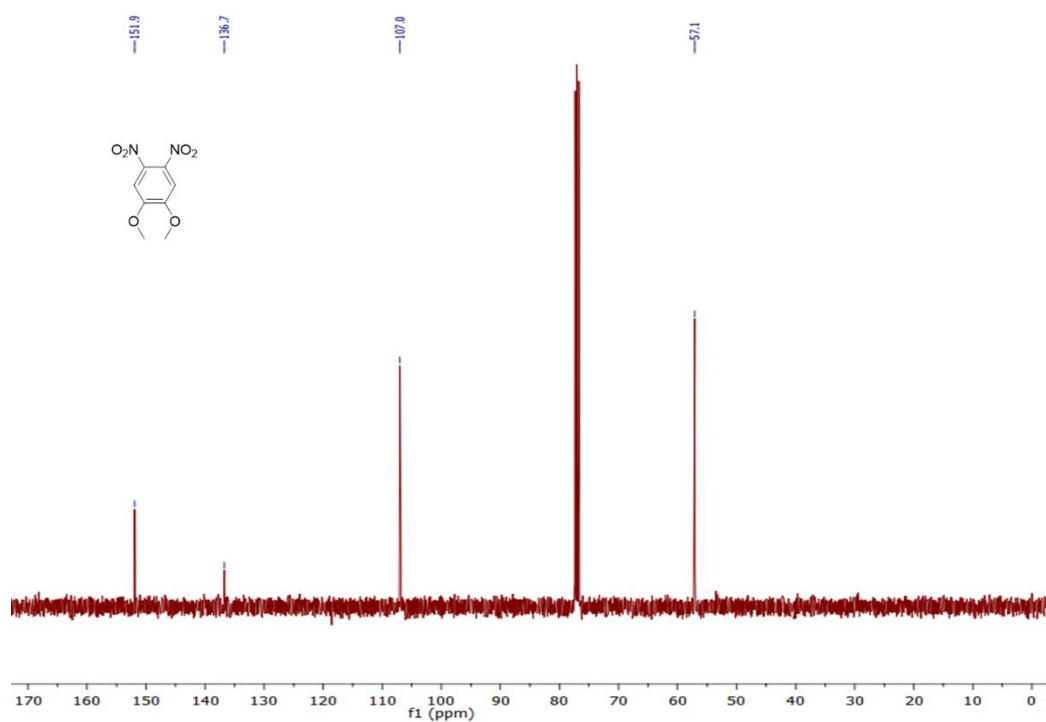


Figure A.2. ¹³C NMR spectrum of compound **2** in CDCl₃

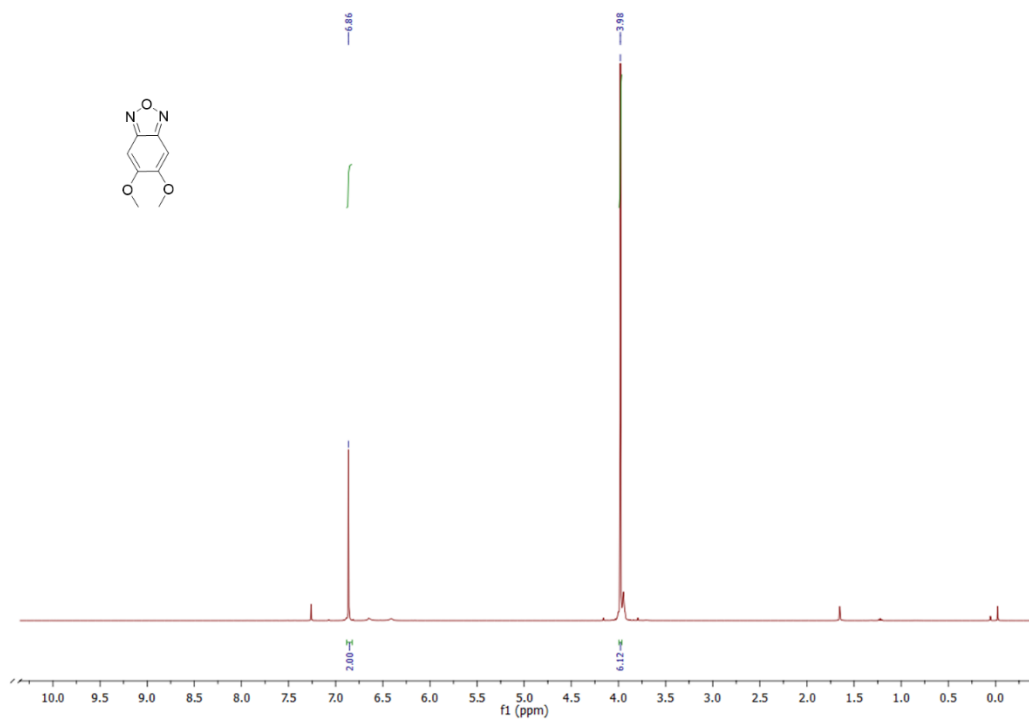


Figure A.3. ¹H NMR spectrum of compound **3** in CDCl₃

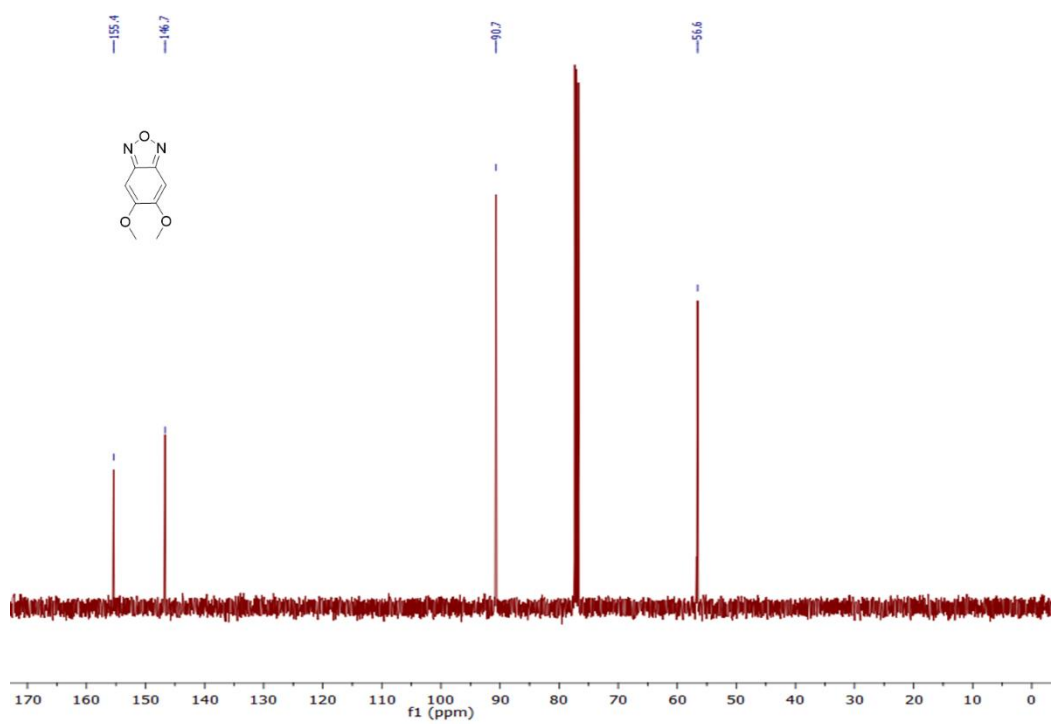


Figure A.4. ^{13}C NMR spectrum of compound **3** in CDCl_3

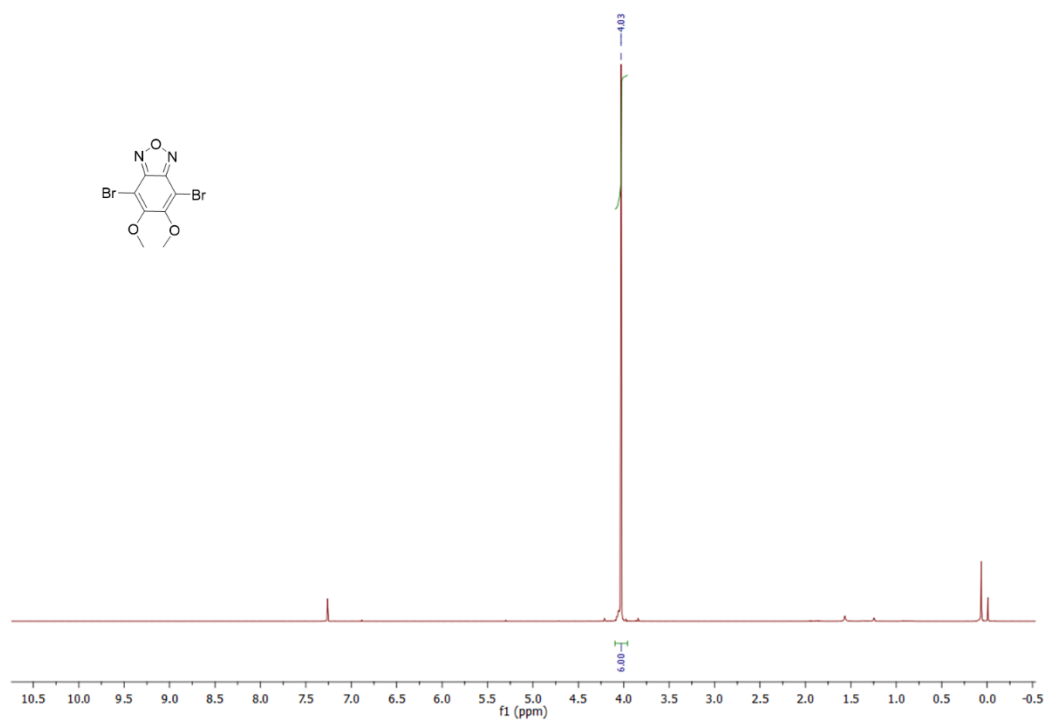


Figure A.5. ^1H NMR spectrum of compound **4** in CDCl_3

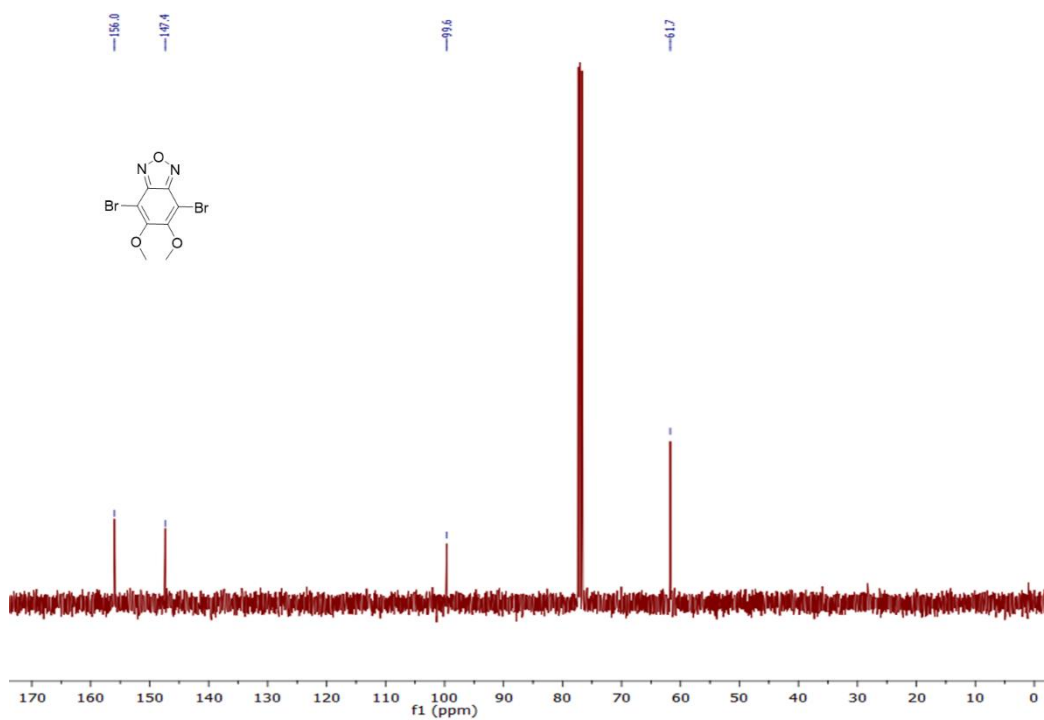


Figure A.6. ¹³C NMR spectrum of compound 4 in CDCl₃

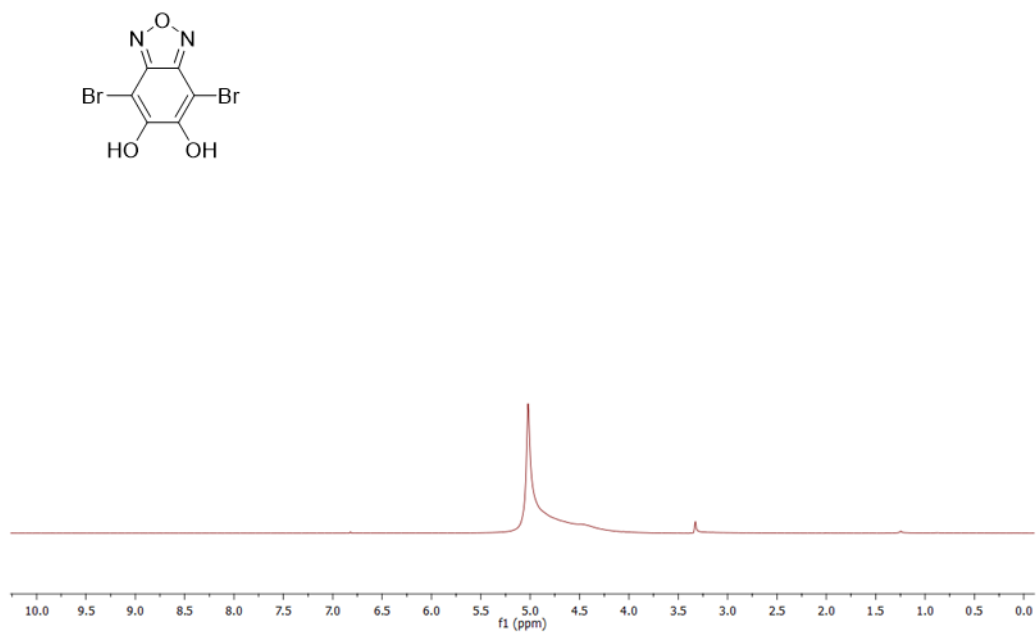


Figure A.7. ¹H NMR spectrum of compound 5 in CD₃OD

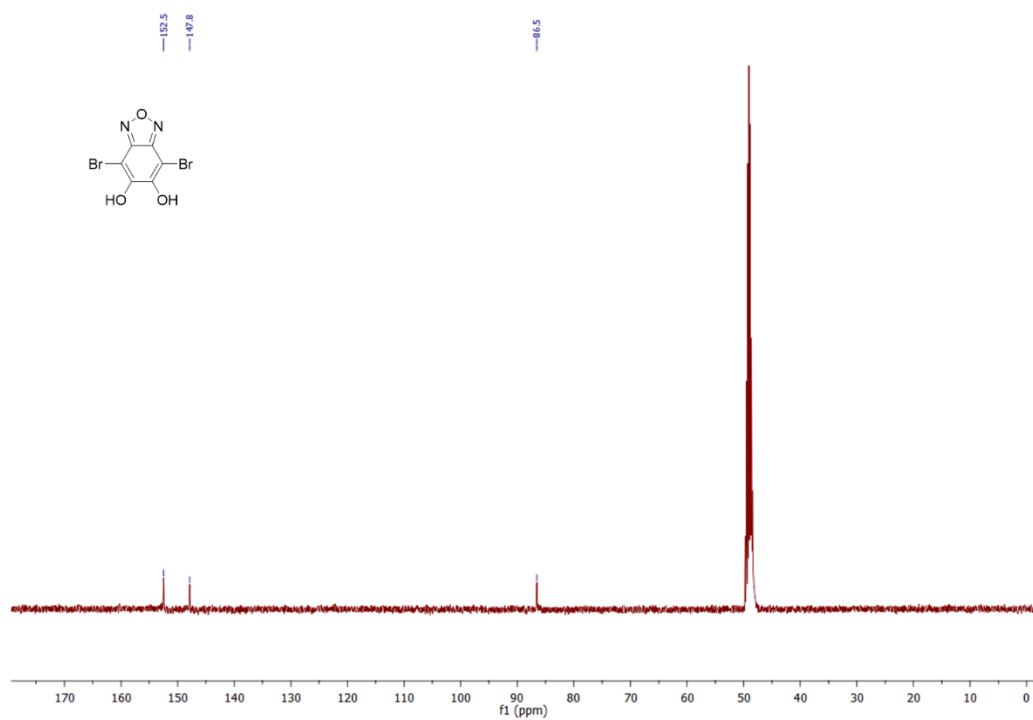


Figure A.8. ^{13}C NMR spectrum of compound **5** in CD_3OD

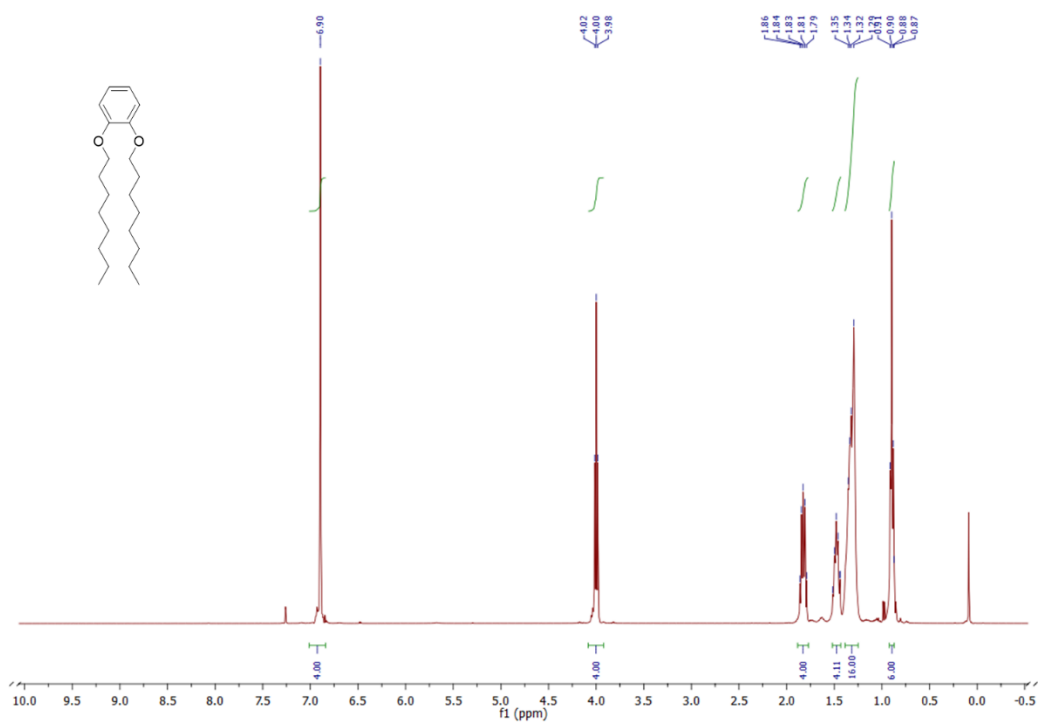


Figure A.9. ^1H NMR spectrum of compound **7** in CDCl_3

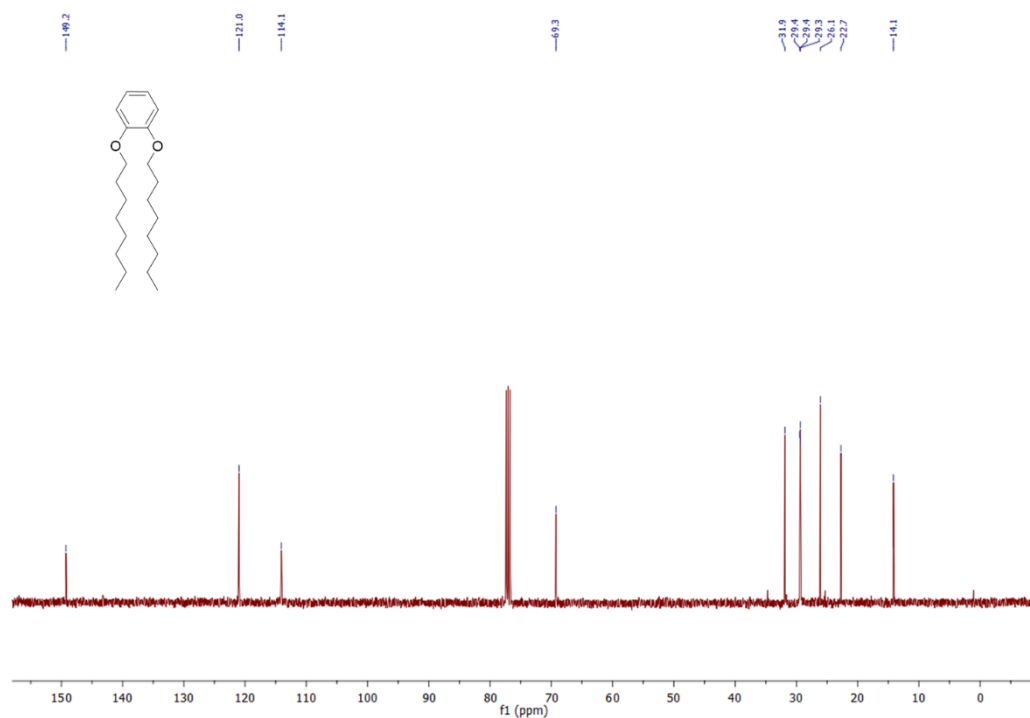


Figure A.10. ^{13}C NMR spectrum of compound **7** in CDCl_3

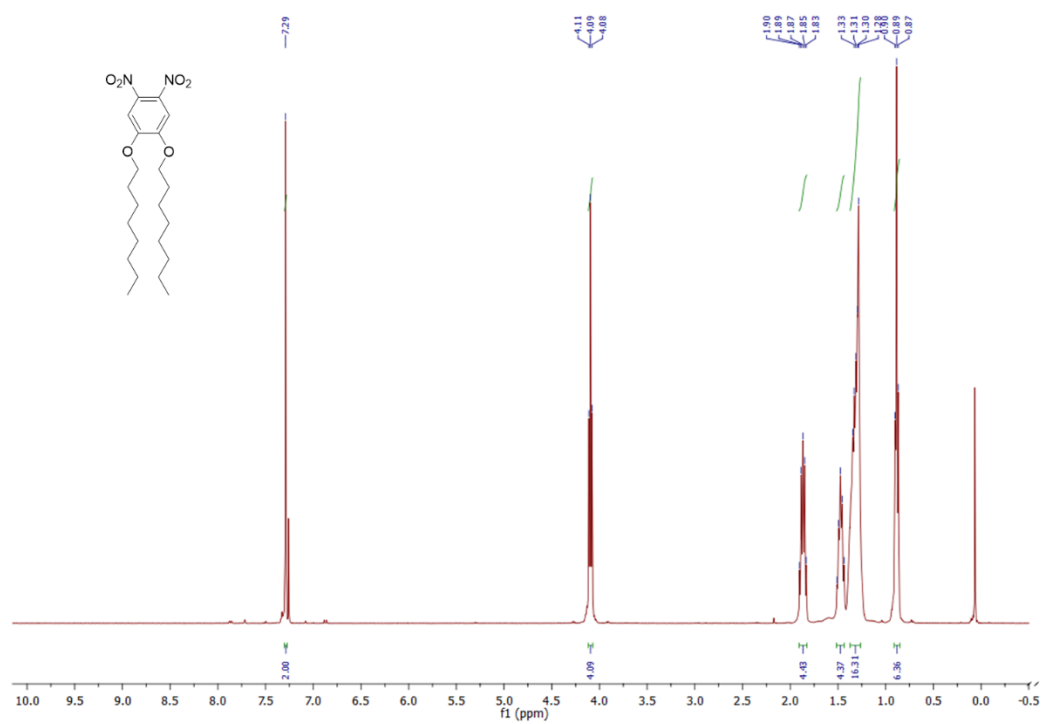


Figure A.11. ^1H NMR spectrum of compound **8** in CDCl_3

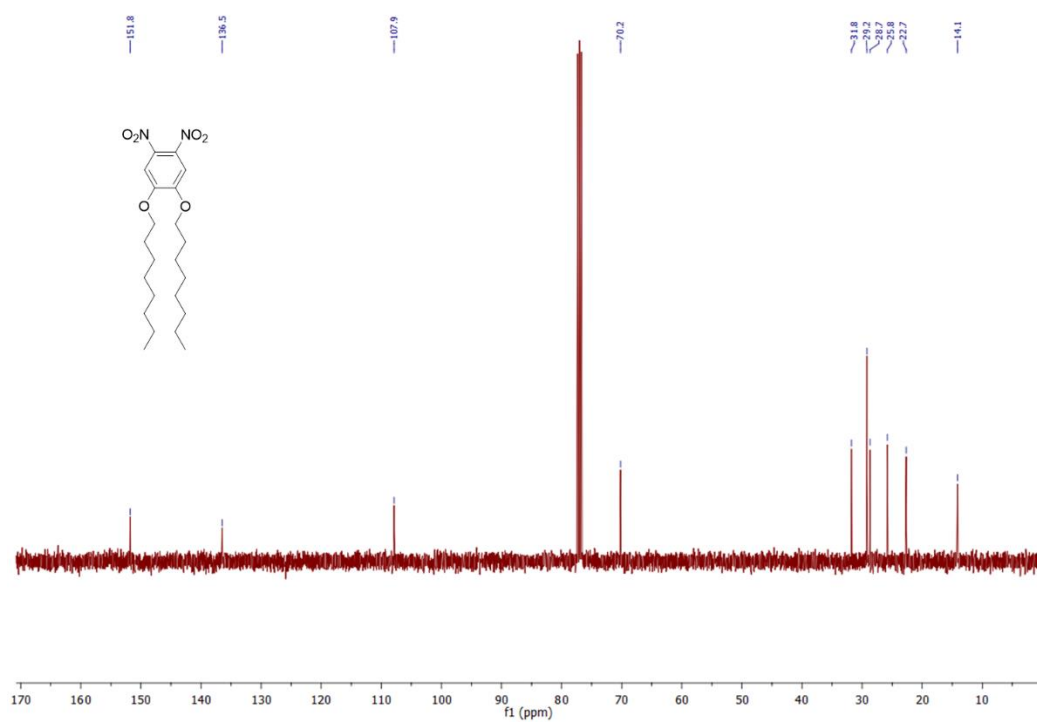


Figure A.12. ^{13}C NMR spectrum of compound **8** in CDCl₃

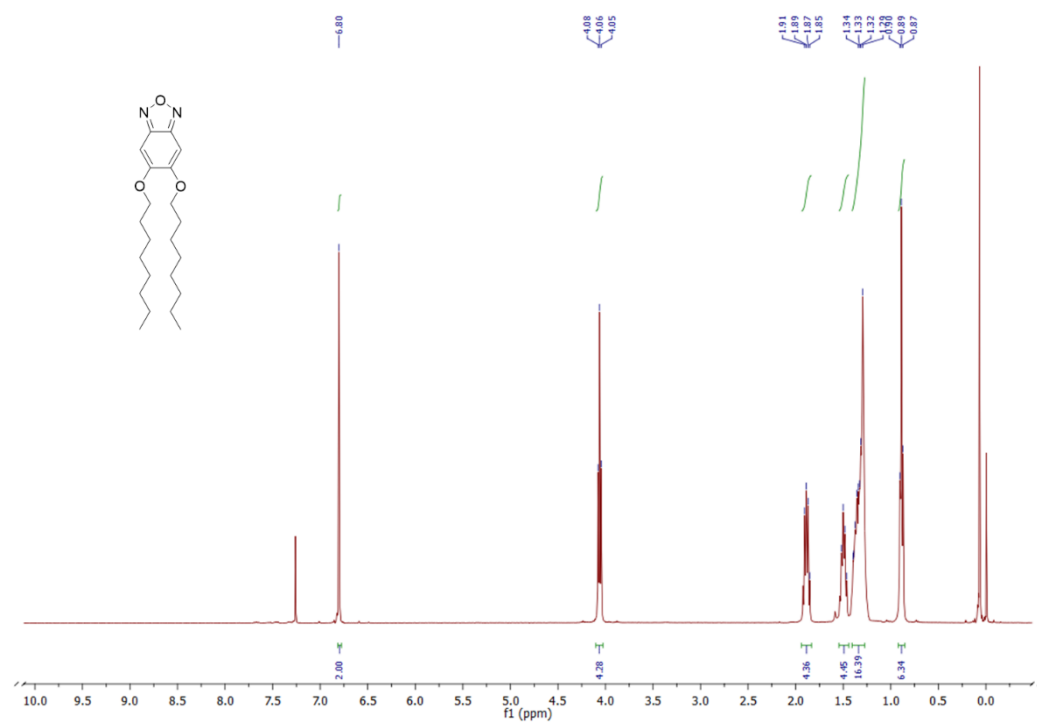


Figure A.13. ^1H NMR spectrum of compound **9** in CDCl₃

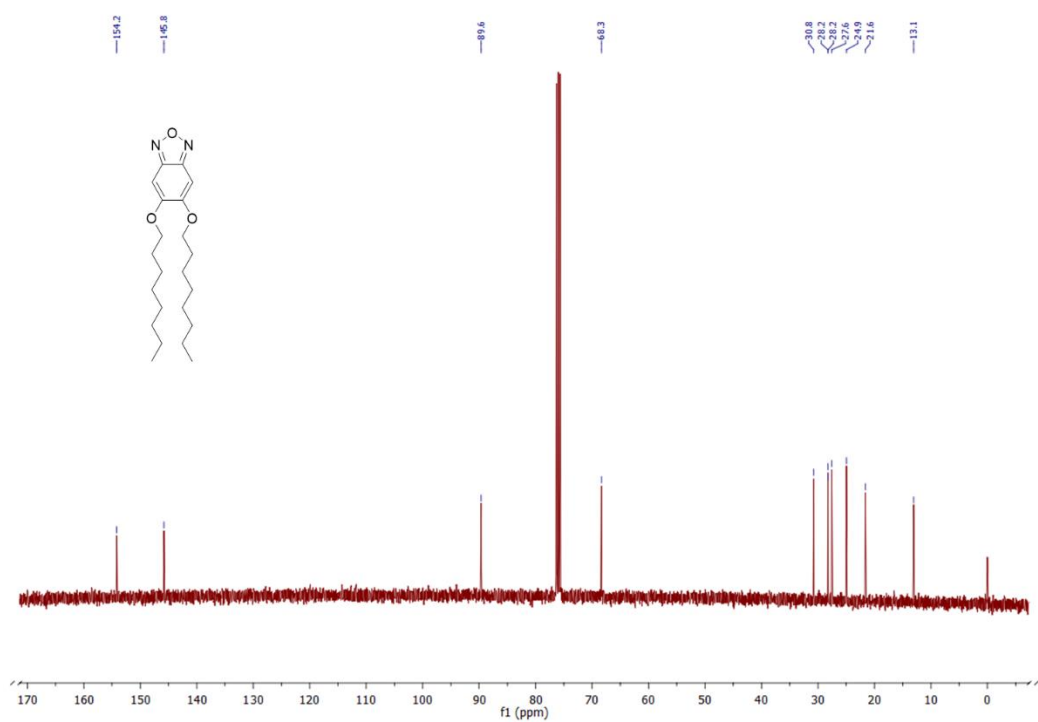


Figure A.14. ^{13}C NMR spectrum of compound **9** in CDCl_3

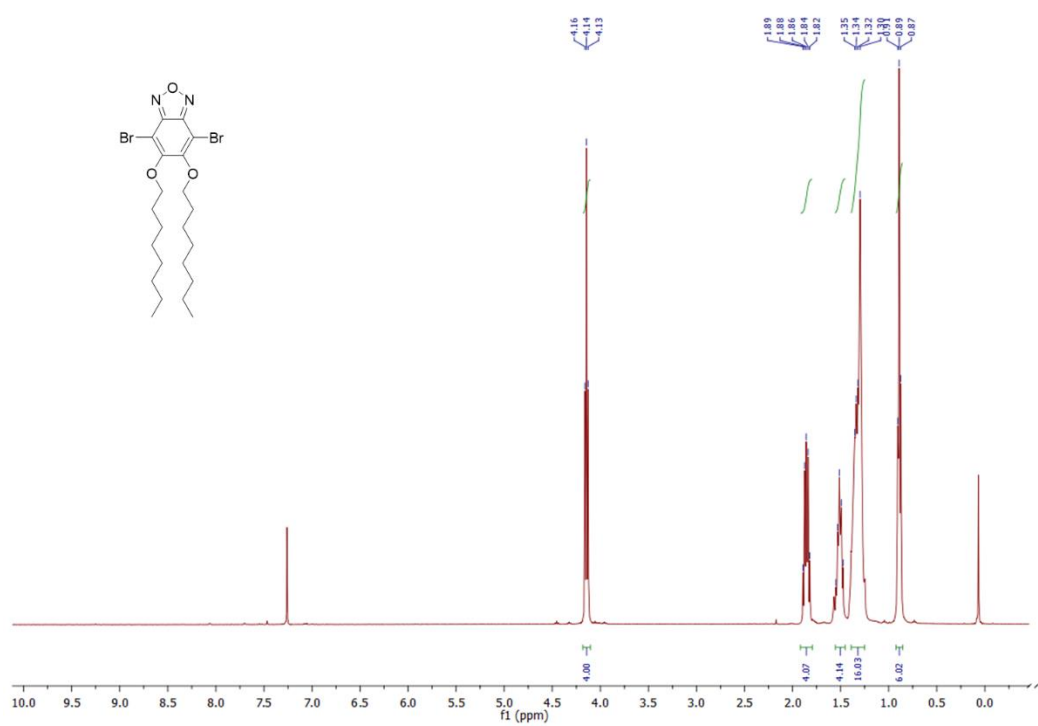


Figure A.15. ^1H NMR spectrum of compound **10** in CDCl_3

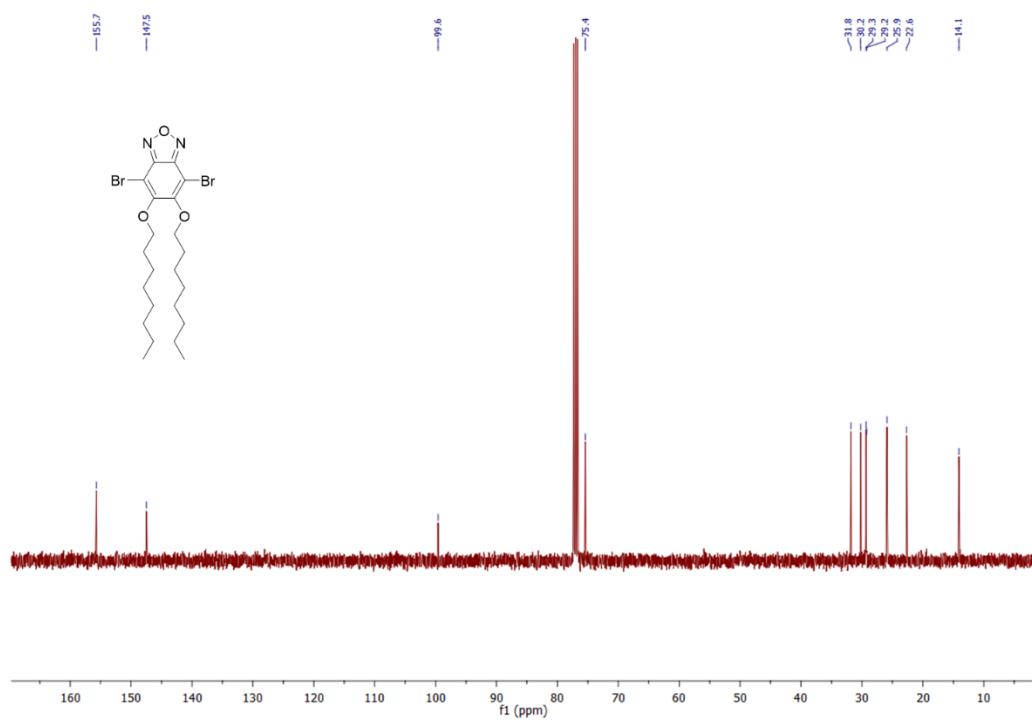


Figure A.16. ^{13}C NMR spectrum of compound **10** in CDCl₃

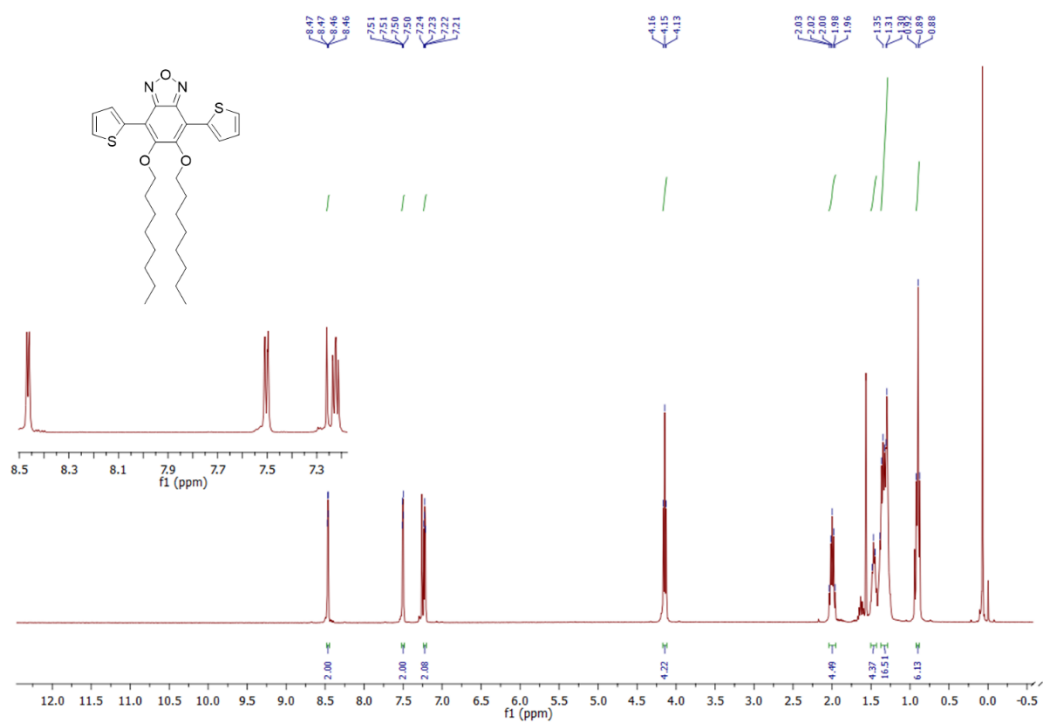


Figure A.17. ^1H NMR spectrum of compound **13** in CDCl₃

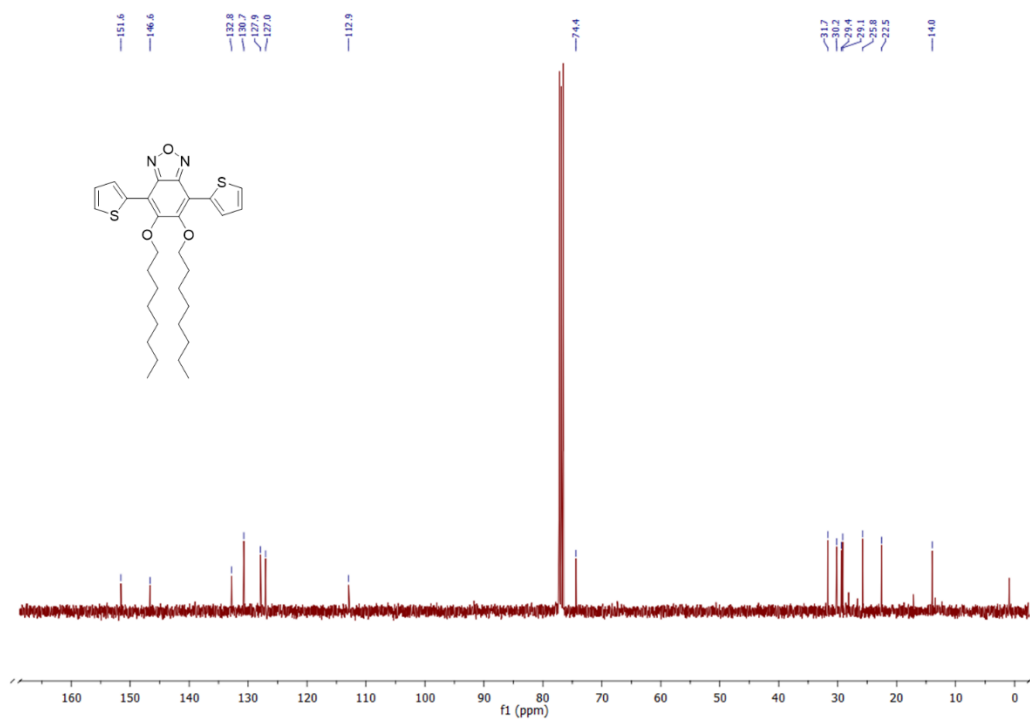


Figure A.18. ^{13}C NMR spectrum of compound **13** in CDCl_3

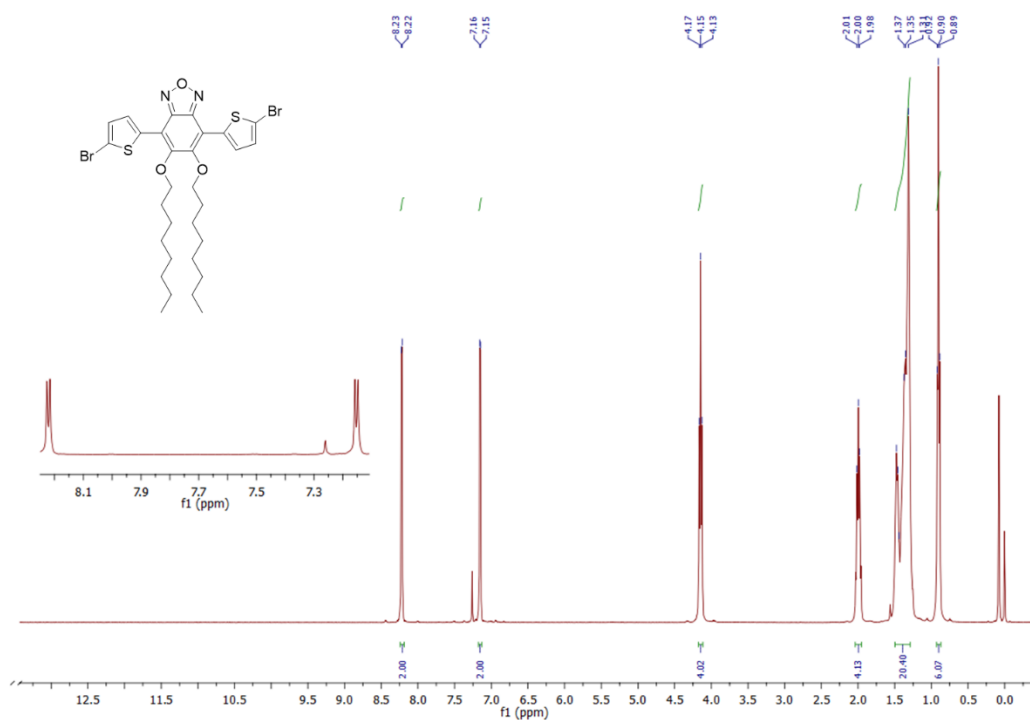


Figure A.19. ^1H NMR spectrum of compound **M1** in CDCl_3

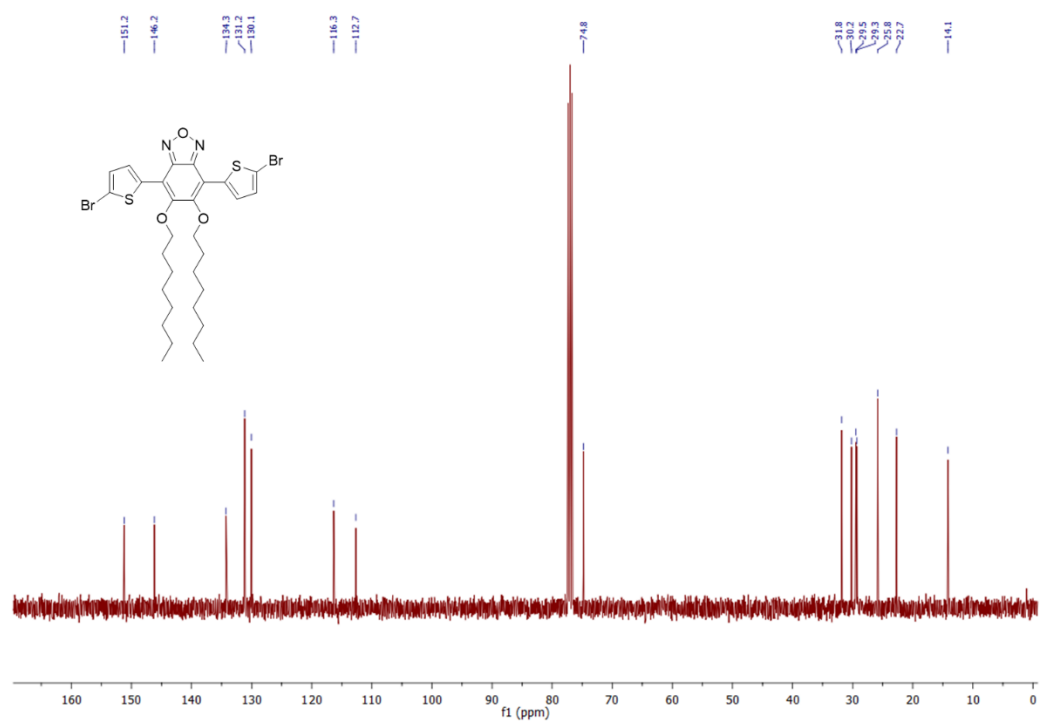


Figure A.20. ^{13}C NMR spectrum of compound **M1** in CDCl_3

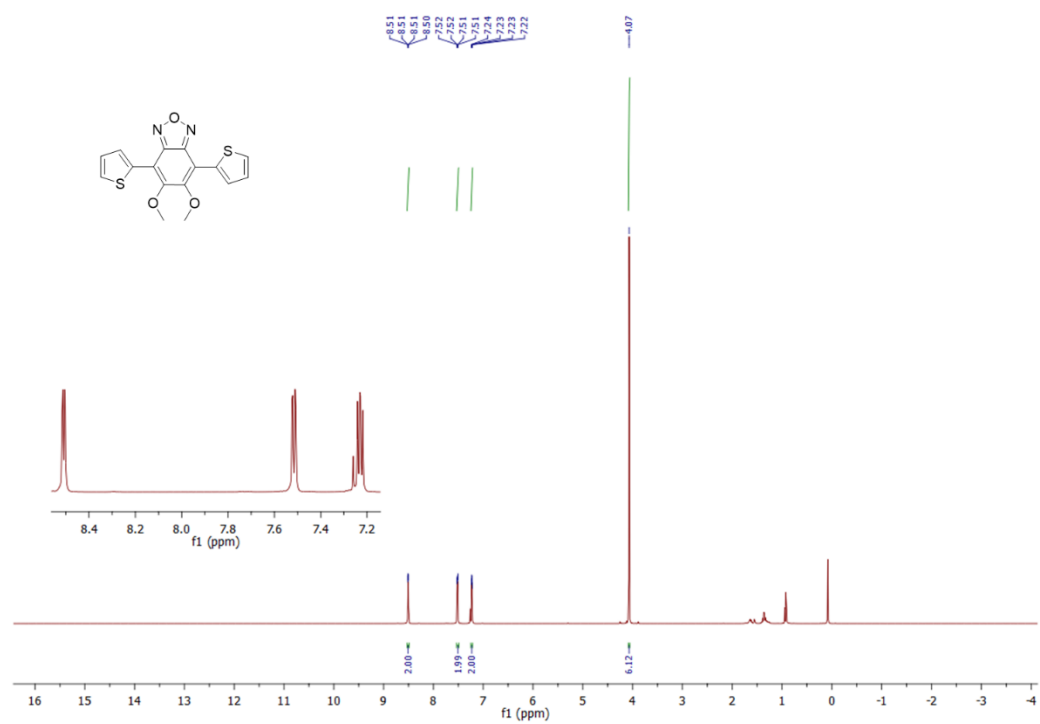


Figure A.21. ^1H NMR spectrum of compound **14** in CDCl_3

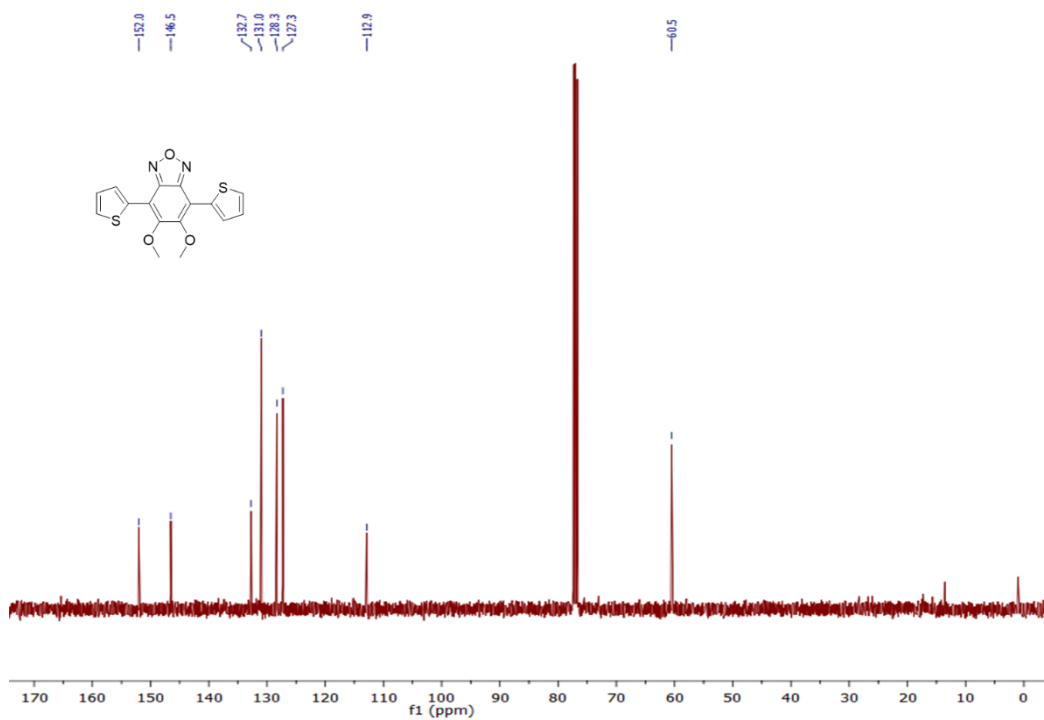


Figure A.22. ^{13}C NMR spectrum of compound **14** in CDCl_3

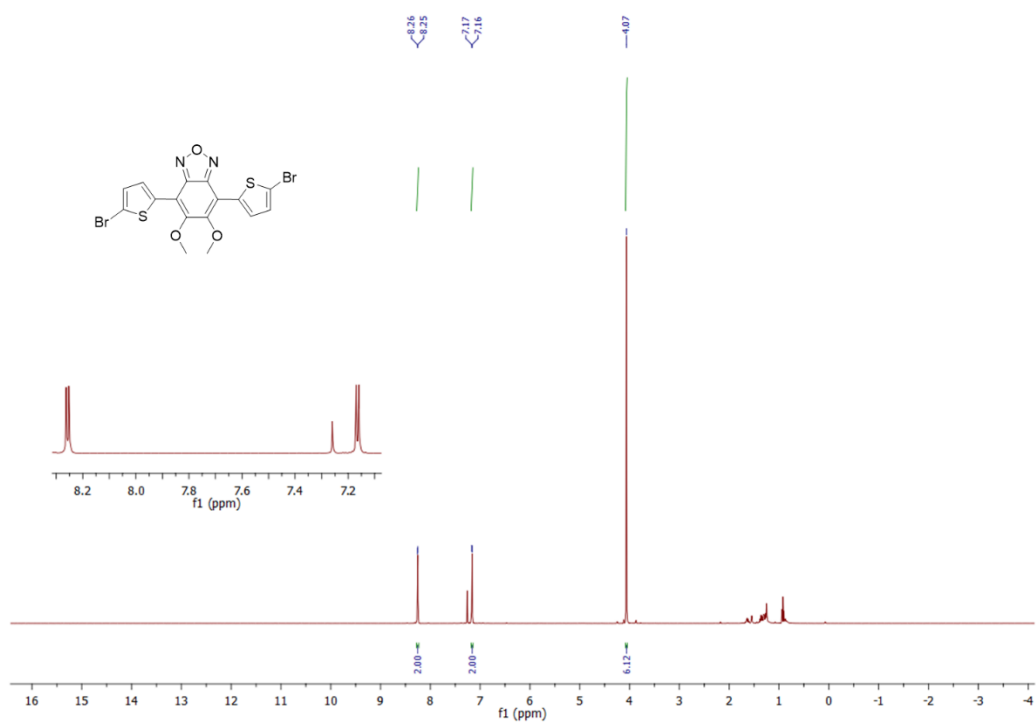


Figure A.23. ^1H NMR spectrum of compound **15** in CDCl_3

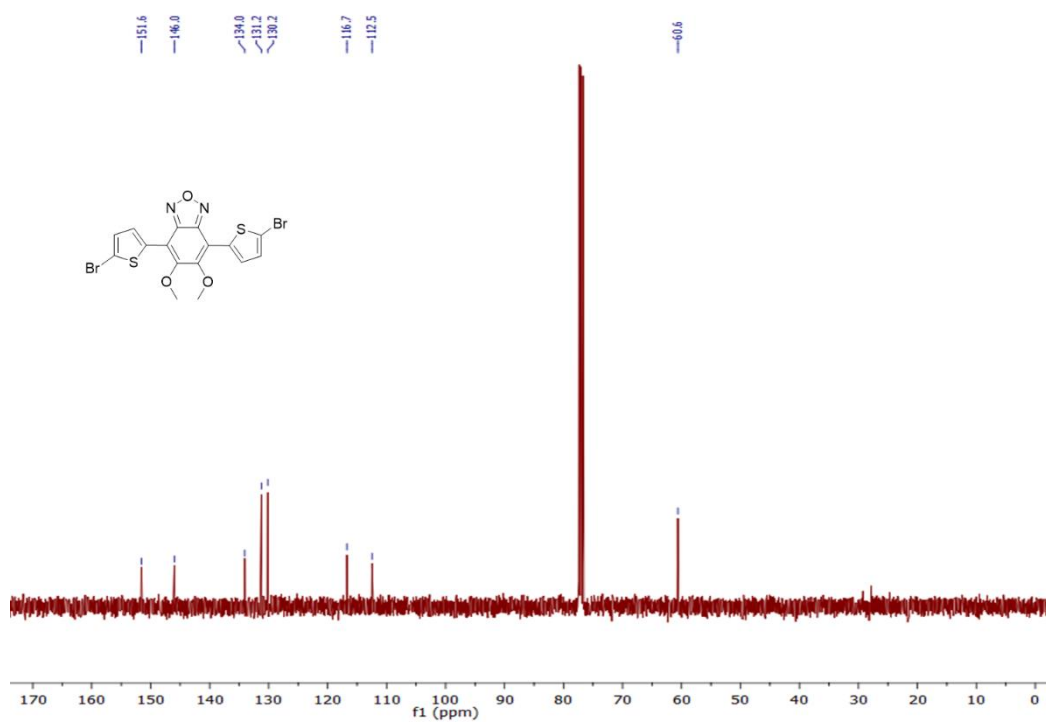


Figure A.24. ^{13}C NMR spectrum of compound **15** in CDCl_3

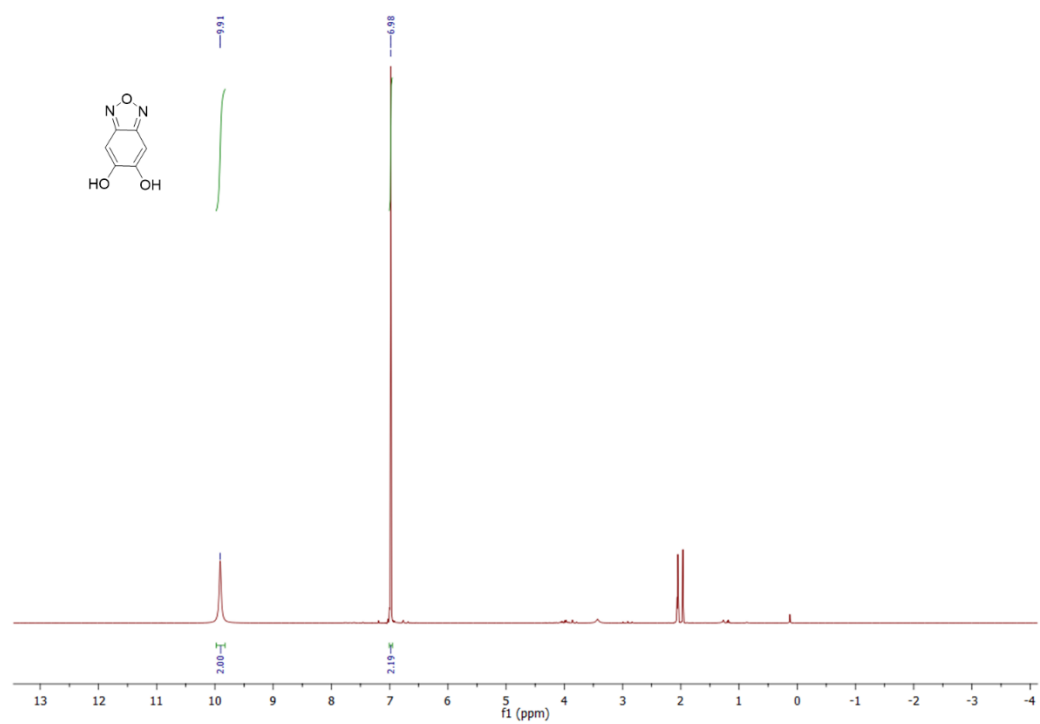


Figure A.25. ^1H NMR spectrum of compound **17** in $(\text{CD}_3)_2\text{CO}$

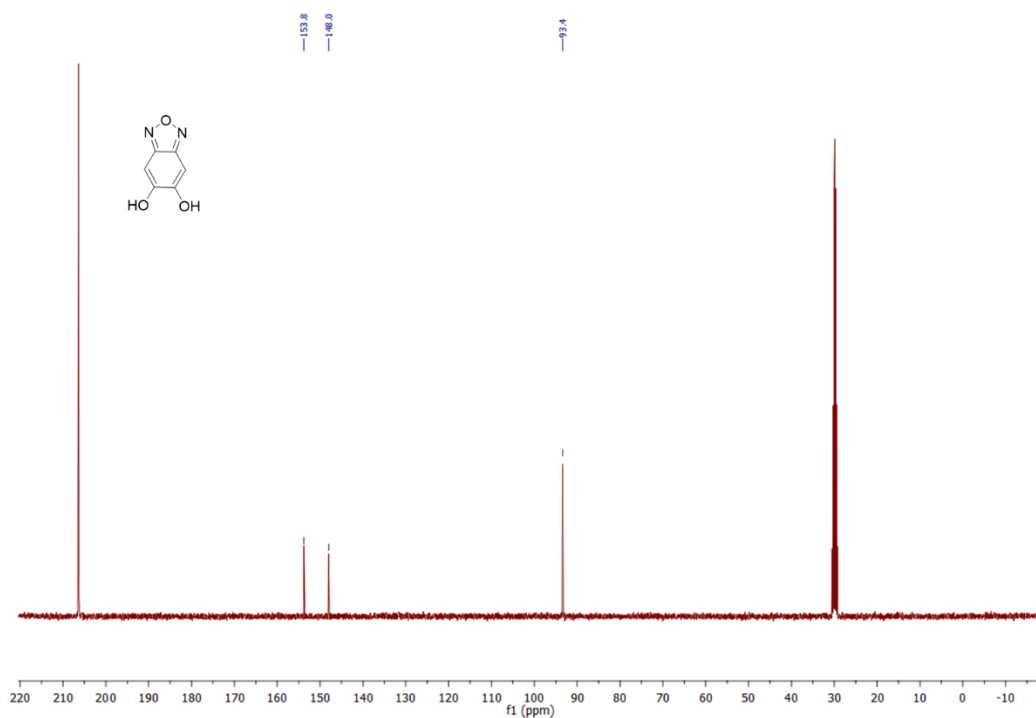


Figure A.26. ^{13}C NMR spectrum of compound **17** in $(\text{CD}_3)_2\text{CO}$

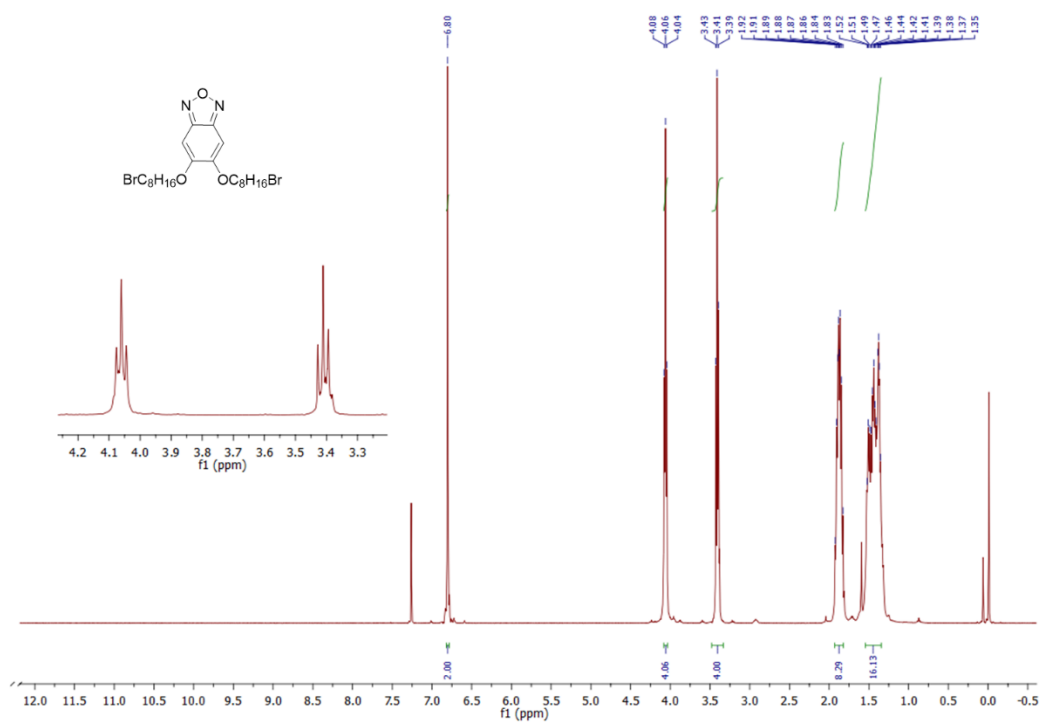


Figure A.27. ^1H NMR spectrum of compound **18** in CDCl_3

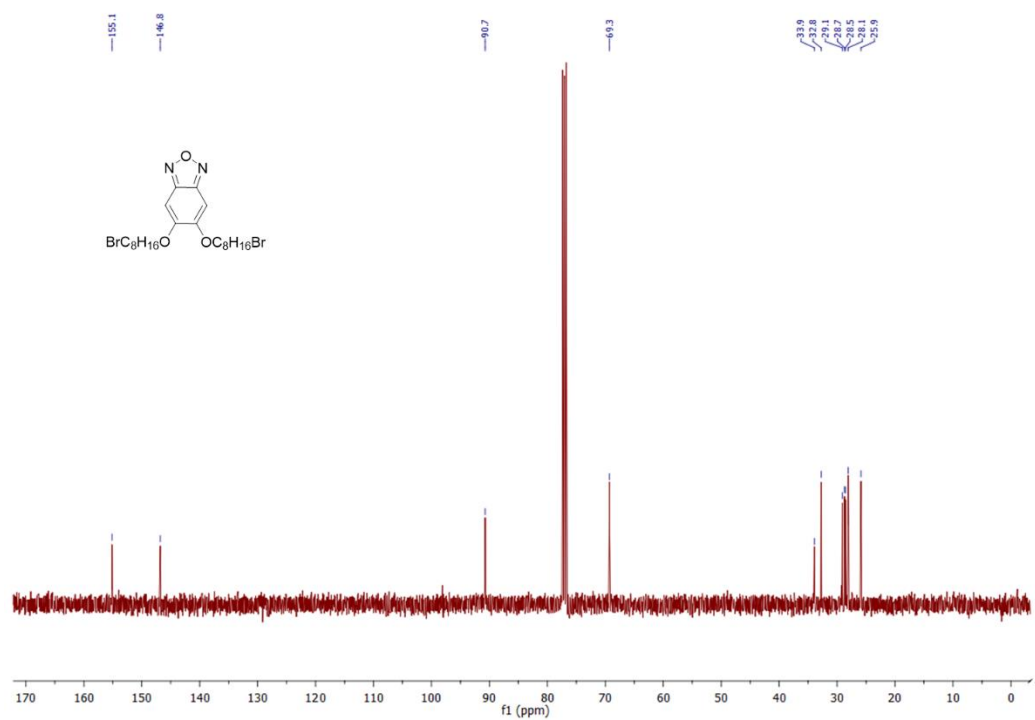


Figure A.28. ^{13}C NMR spectrum of compound **18** in CDCl_3

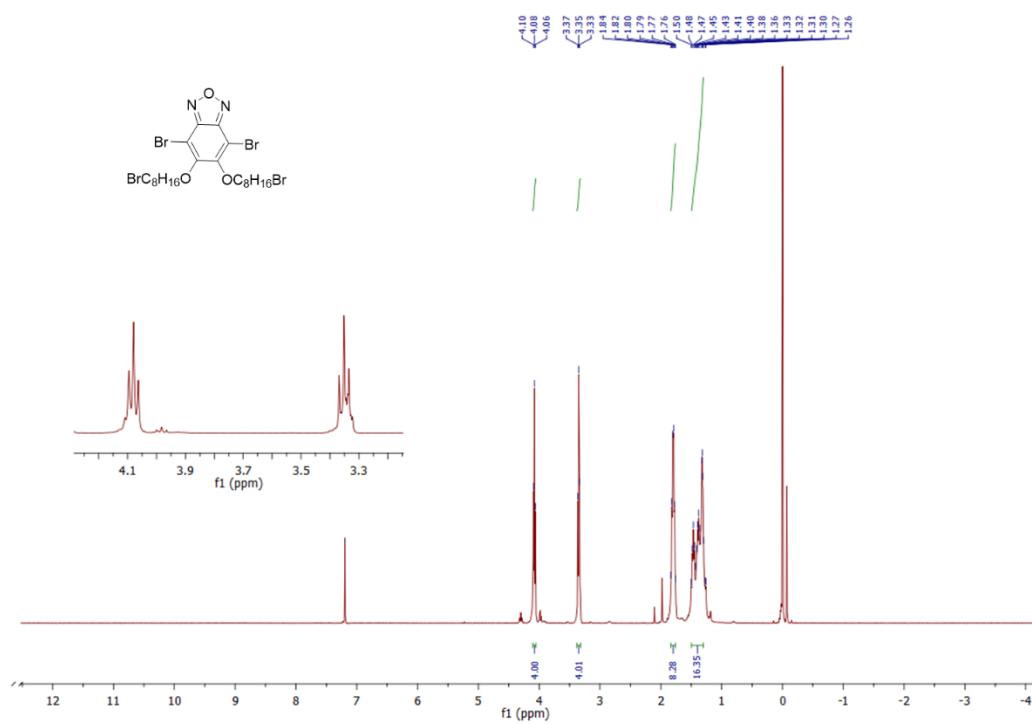


Figure A.29. ^1H NMR spectrum of compound **19** in CDCl_3

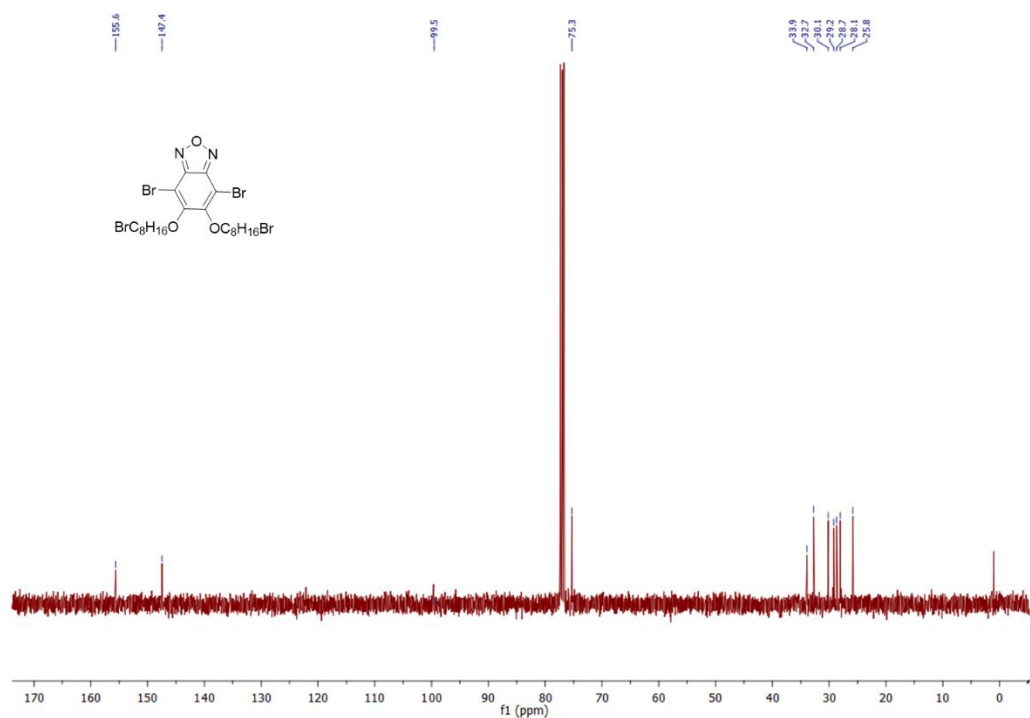


Figure A.30. ^{13}C NMR spectrum of compound **19** in CDCl_3

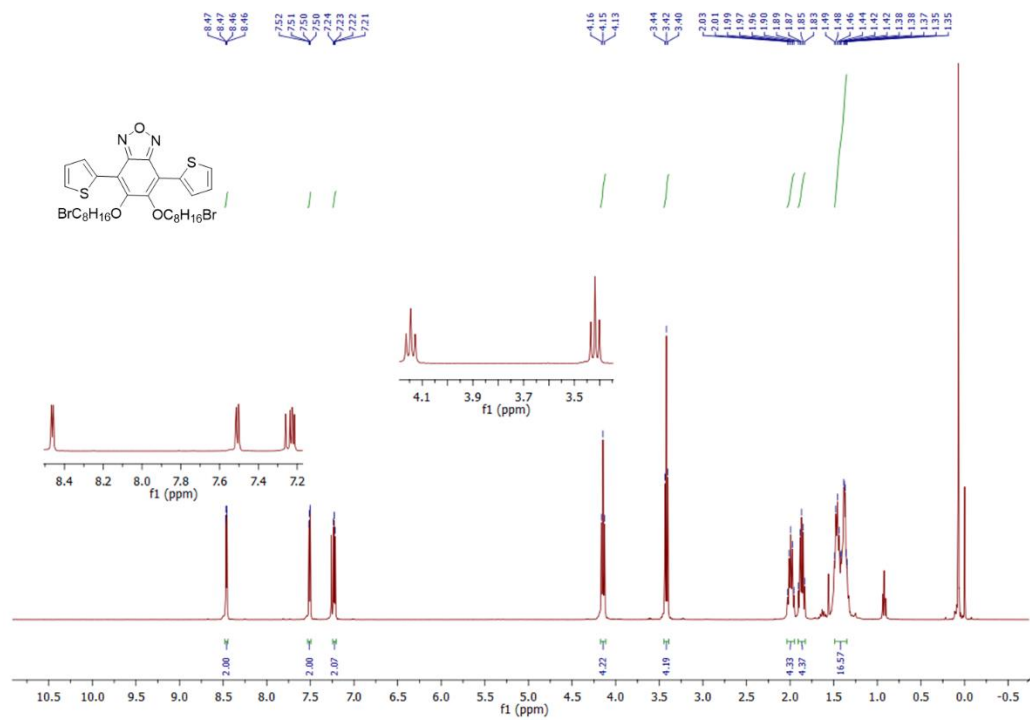


Figure A.31. ^1H NMR spectrum of compound **20** in CDCl_3

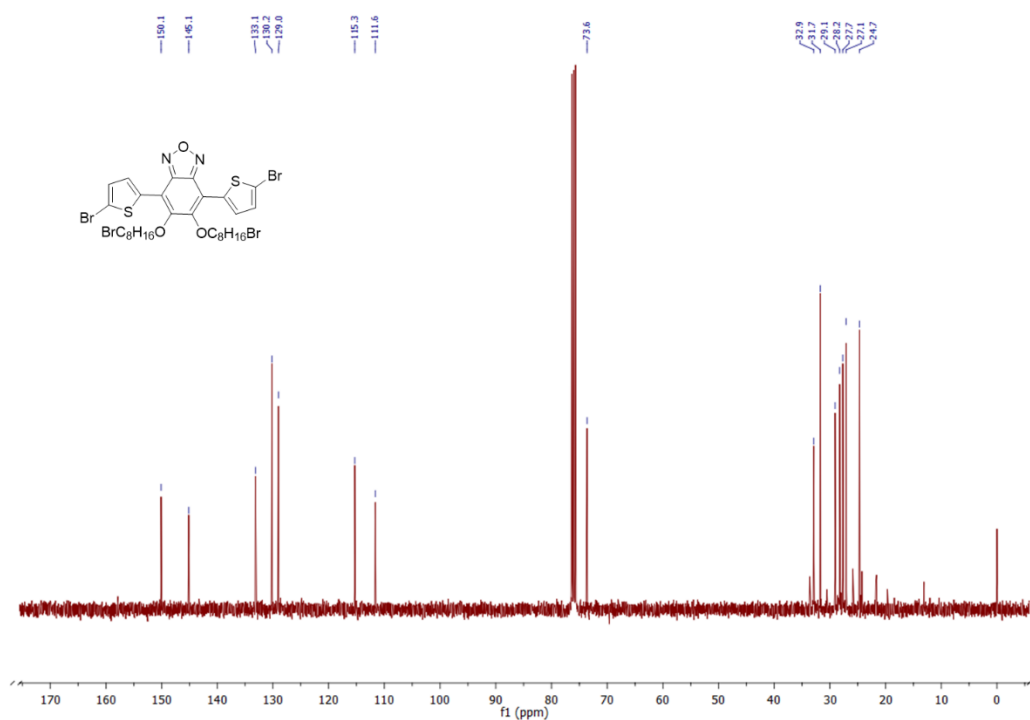


Figure A.34. ^{13}C NMR spectrum of compound **M2** in CDCl_3

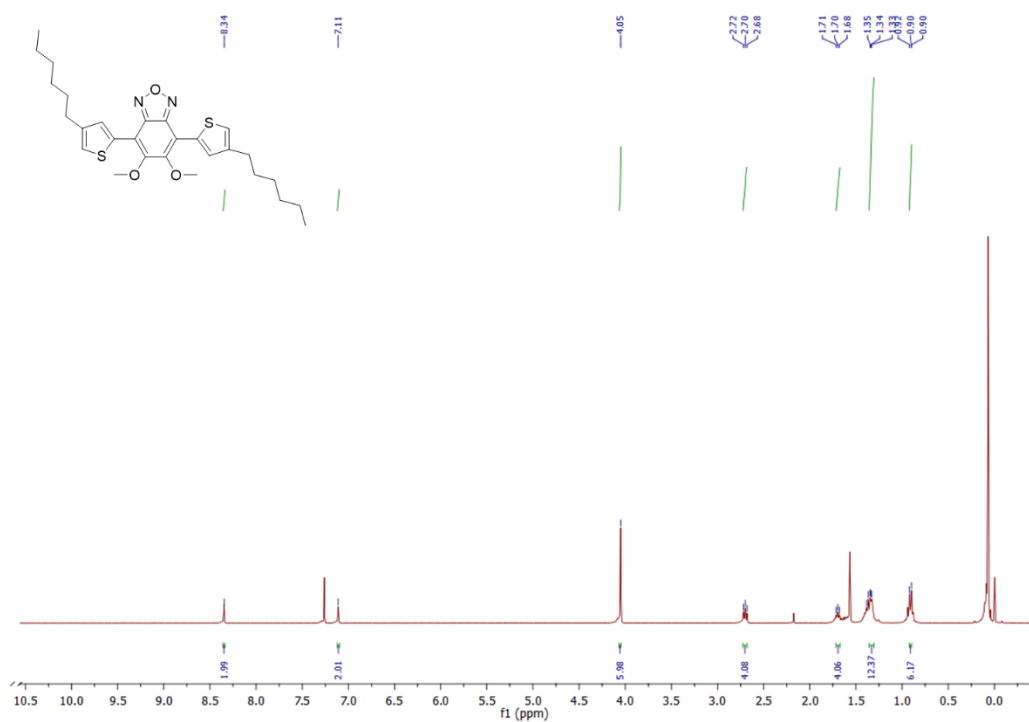


Figure A.35. ^1H NMR spectrum of compound **25** in CDCl_3

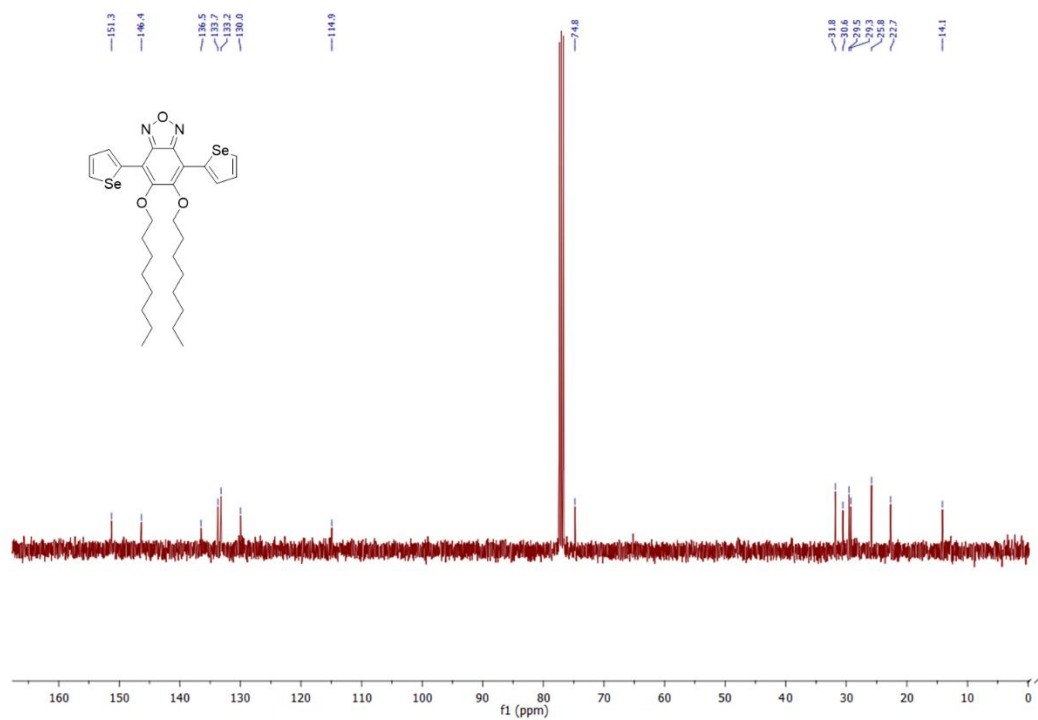


Figure A.38. ^{13}C NMR spectrum of compound **26** in CDCl_3

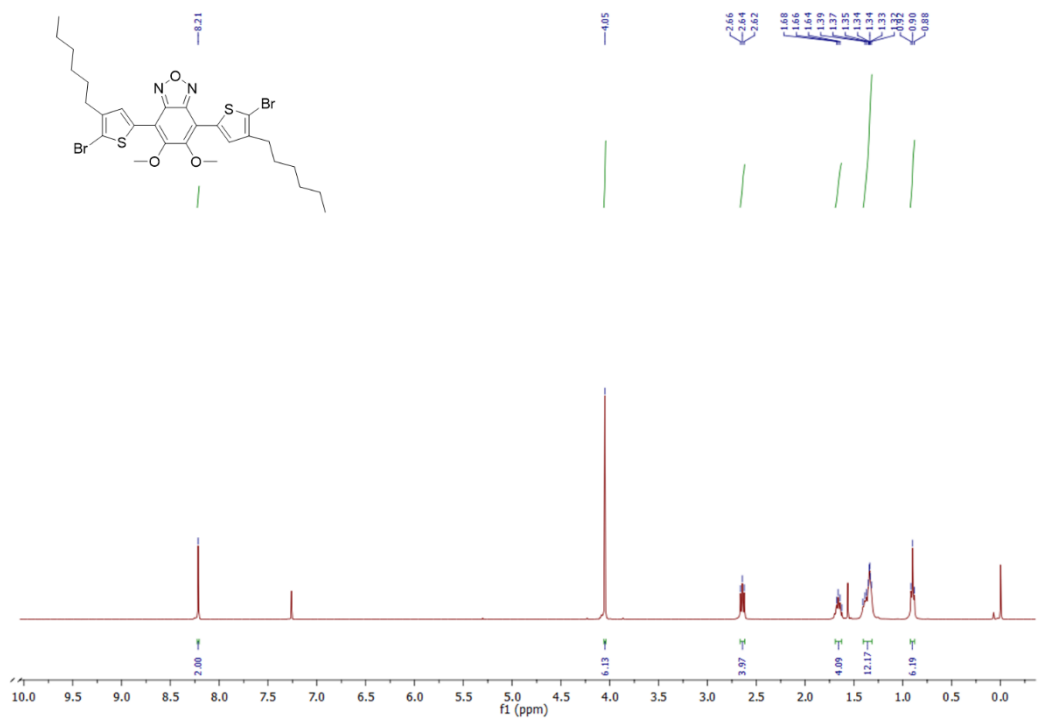


Figure A.39. ^1H NMR spectrum of compound **M3** in CDCl_3

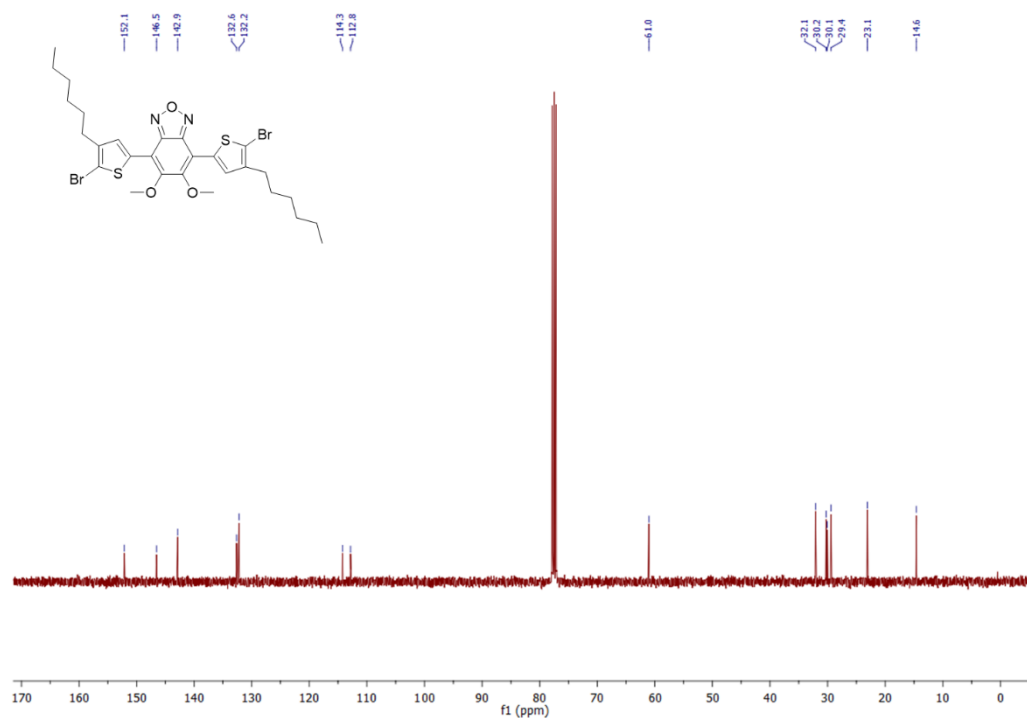


Figure A.40. ^{13}C NMR spectrum of compound **M3** in CDCl_3

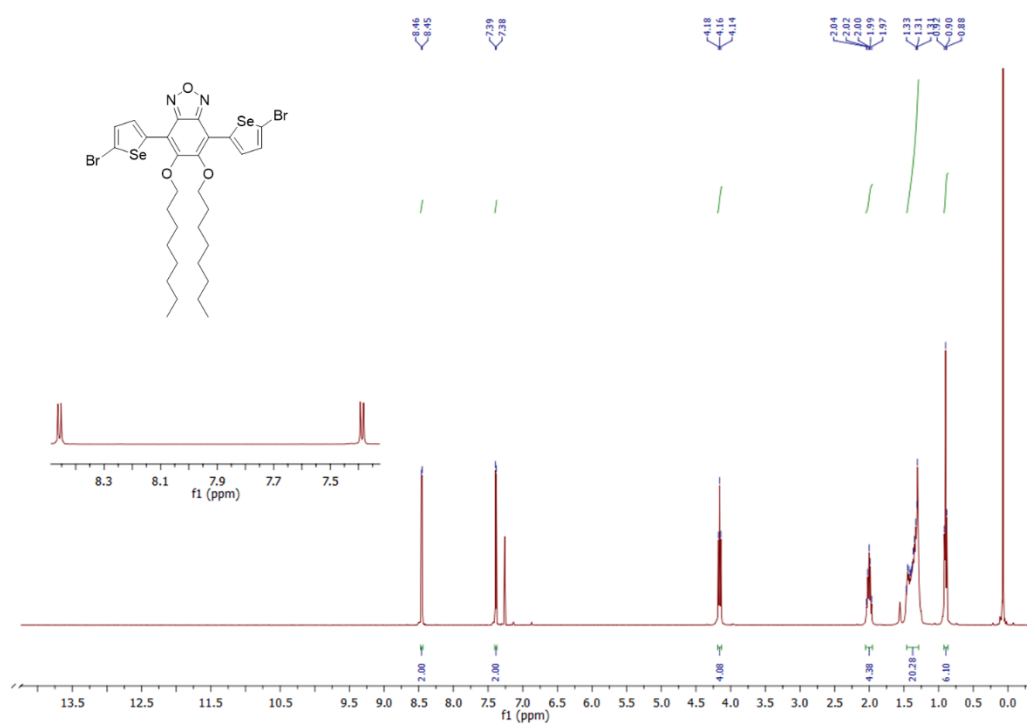


Figure A.41. ^1H NMR spectrum of compound **M4** in CDCl_3

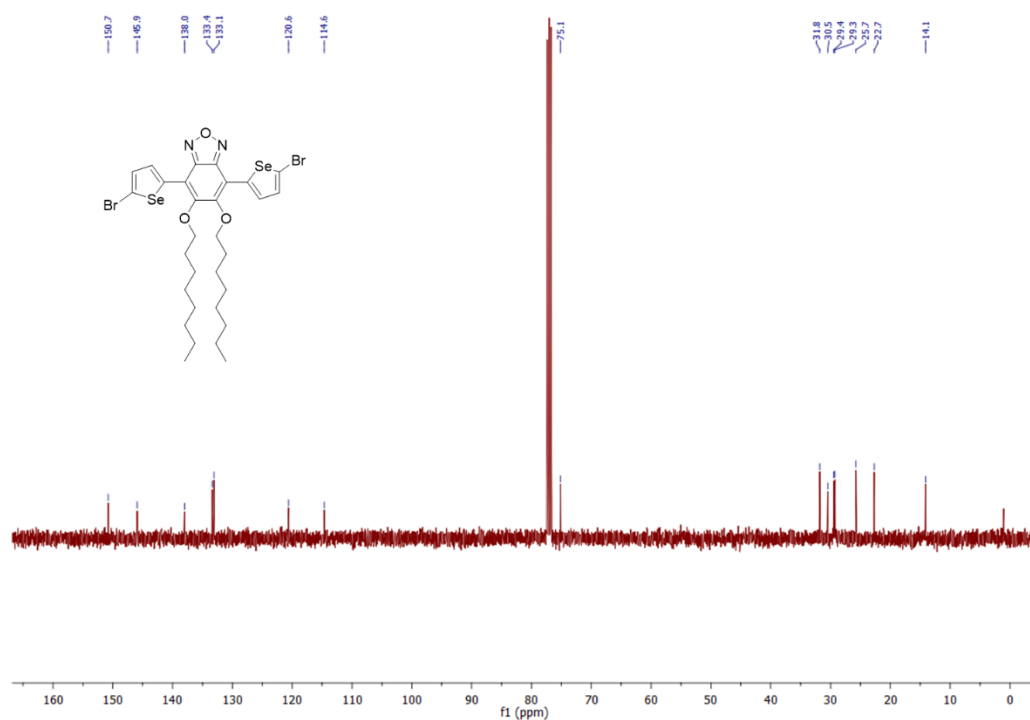


Figure A.42. ¹³C NMR spectrum of compound M4 in CDCl₃

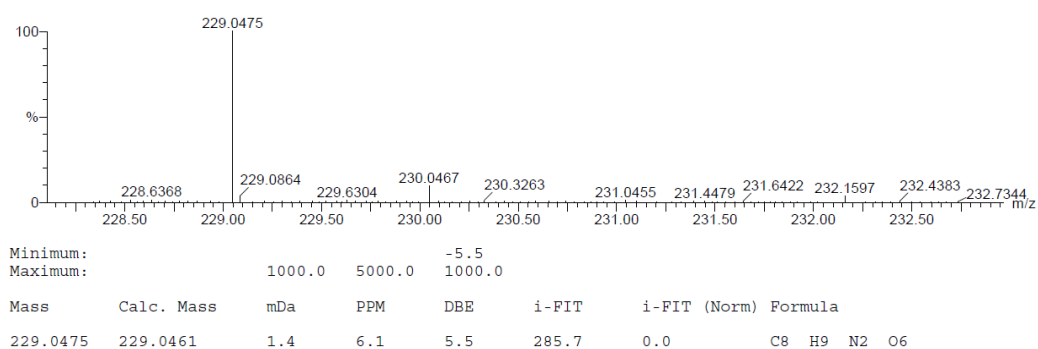


Figure A.43. HRMS spectrum of compound 2

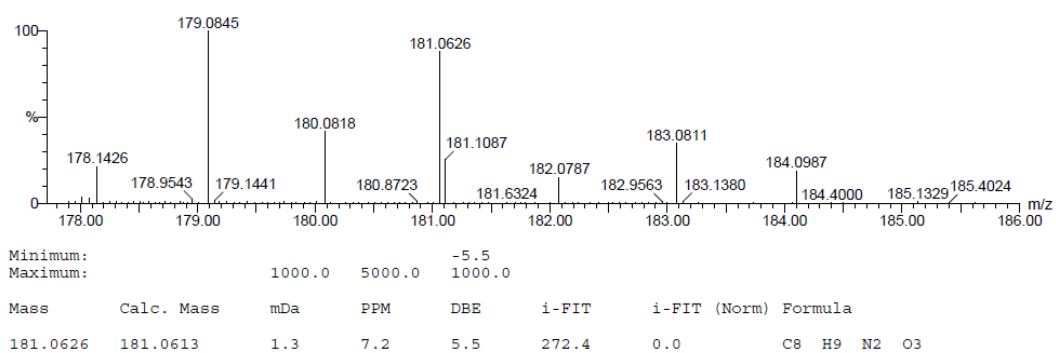


Figure A.44. HRMS spectrum of compound **3**

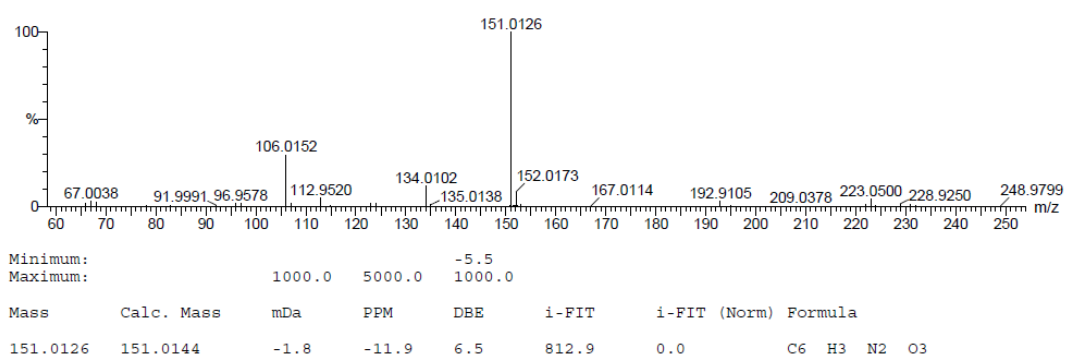


Figure A.45. HRMS spectrum of compound **17**

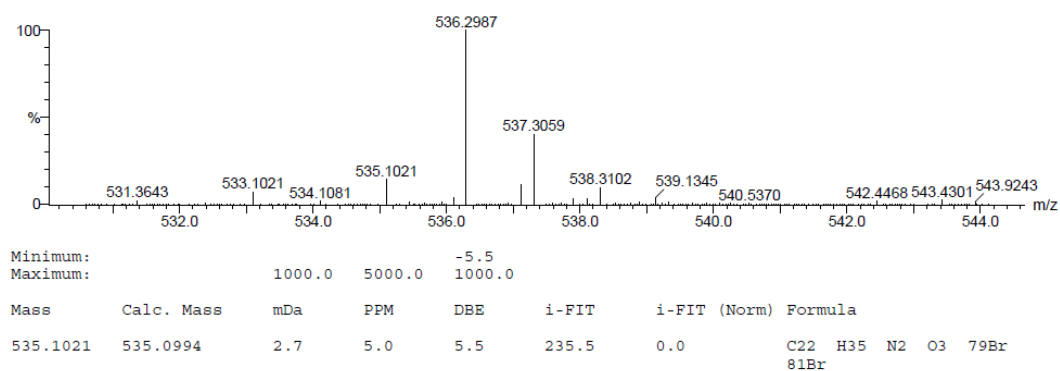


Figure A.46. HRMS spectrum of compound **18**

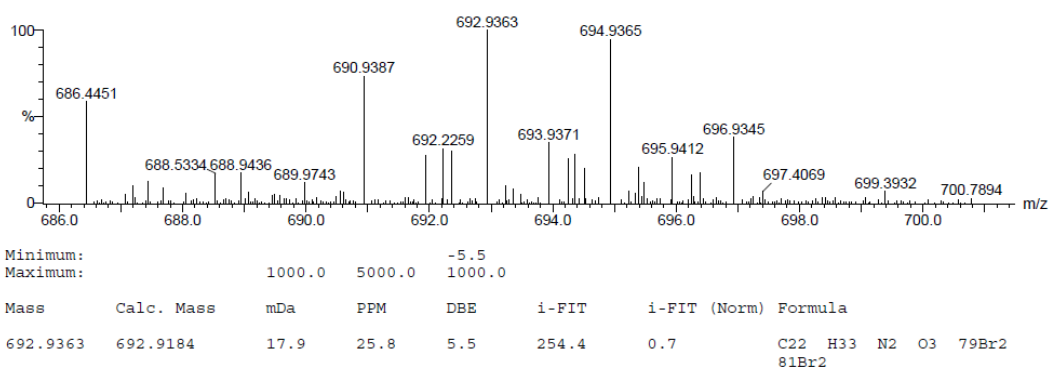


Figure A.47. HRMS spectrum of compound **19**

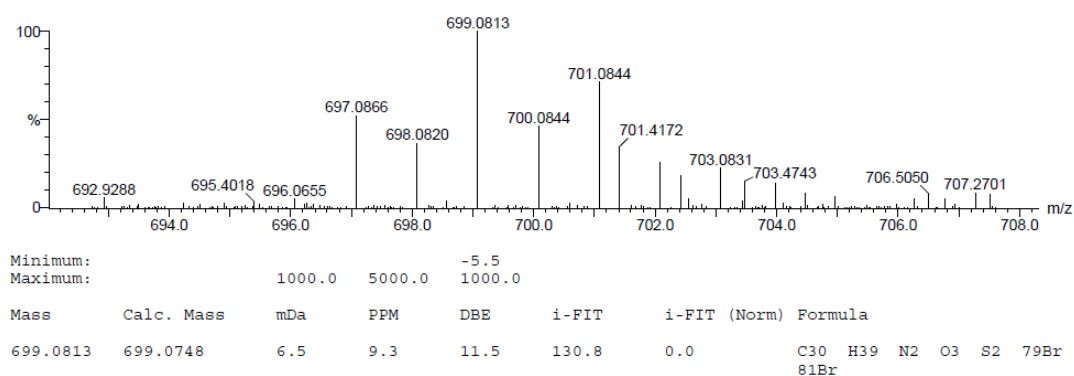


Figure A.48. HRMS spectrum of compound **20**

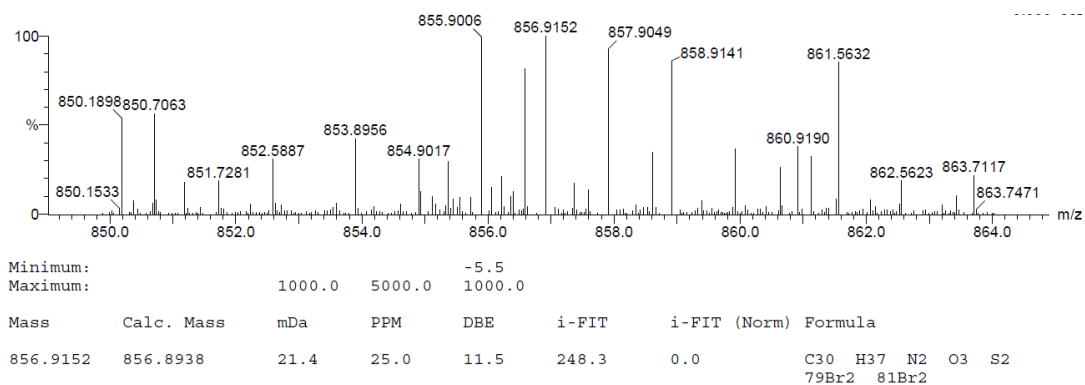


Figure A.49. HRMS spectrum of compound **M2**

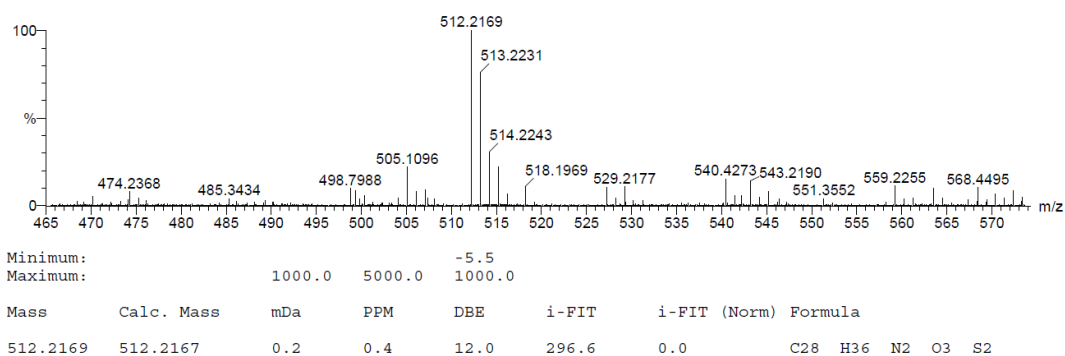


Figure A.50. HRMS spectrum of compound **25**

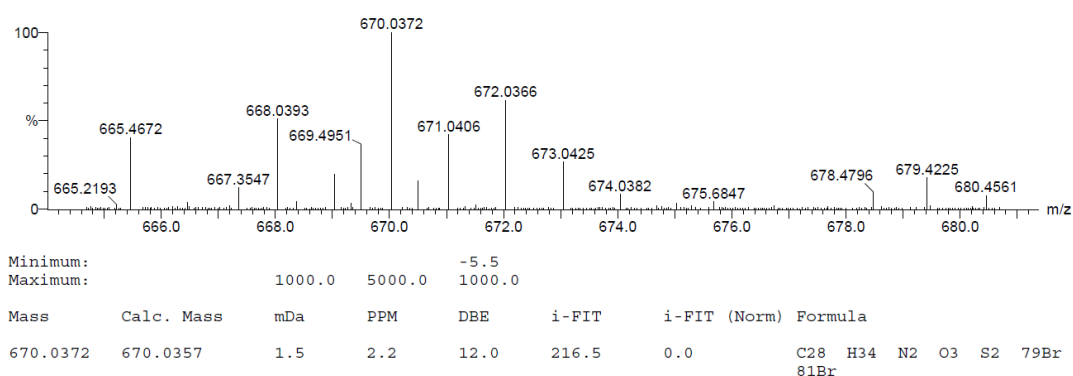


Figure A.51. HRMS spectrum of compound **M3**

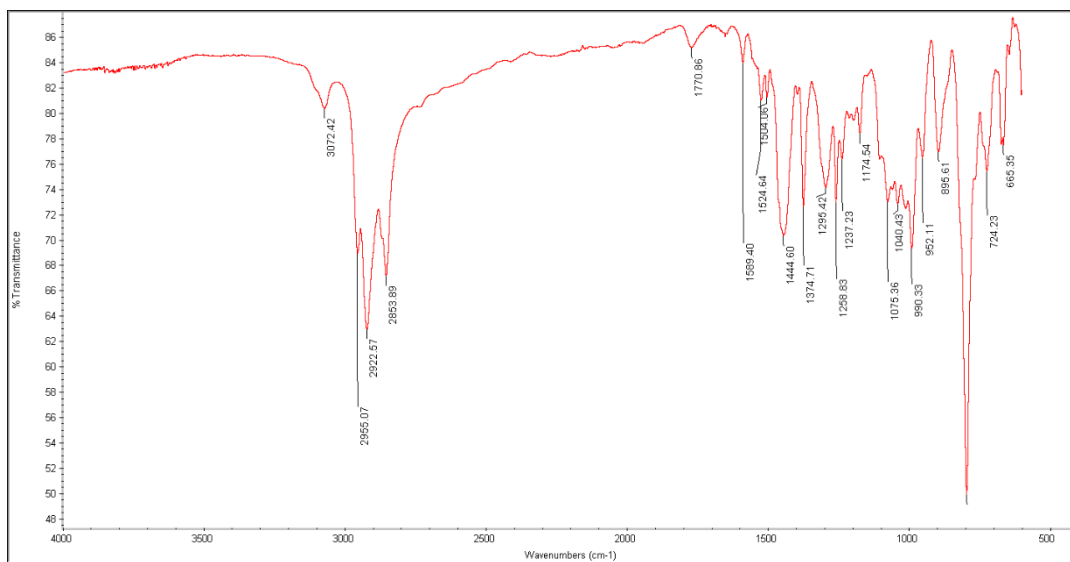


Figure A.52. IR-spectrum of **P1**

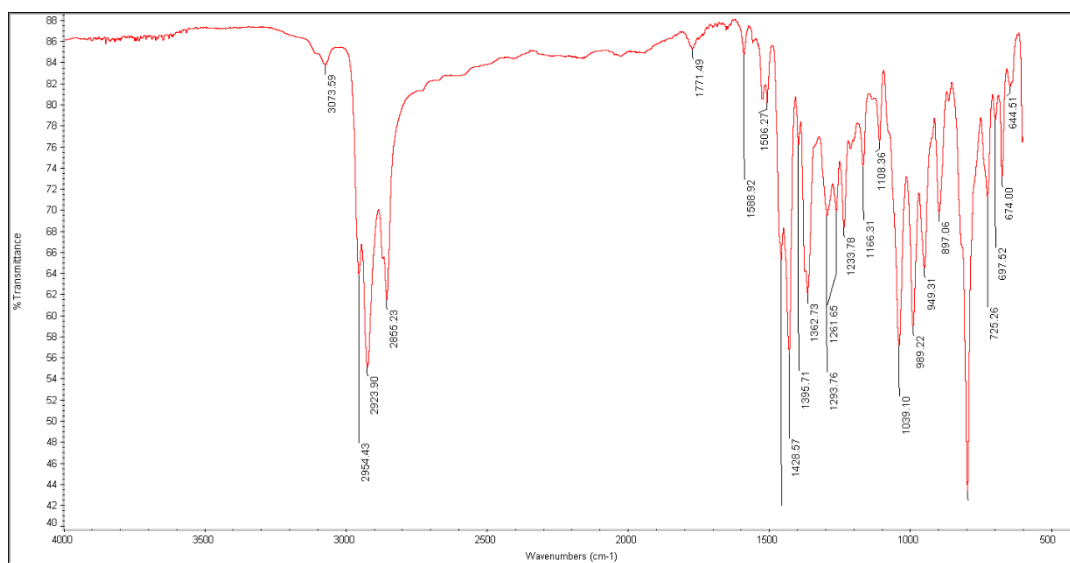


Figure A.53. IR-spectrum of **P2**

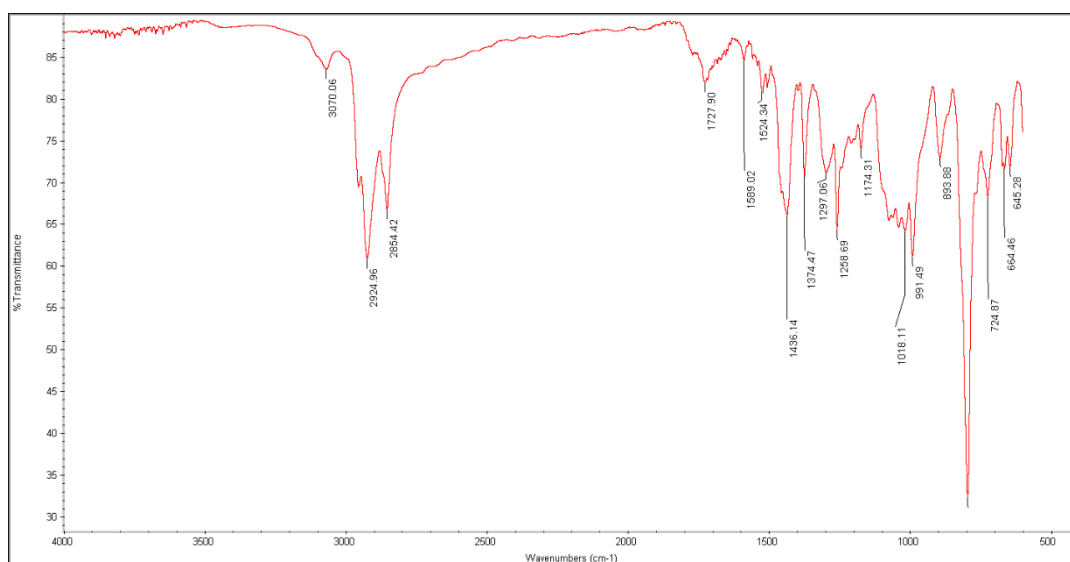


Figure A.54. IR-spectrum of **P3**

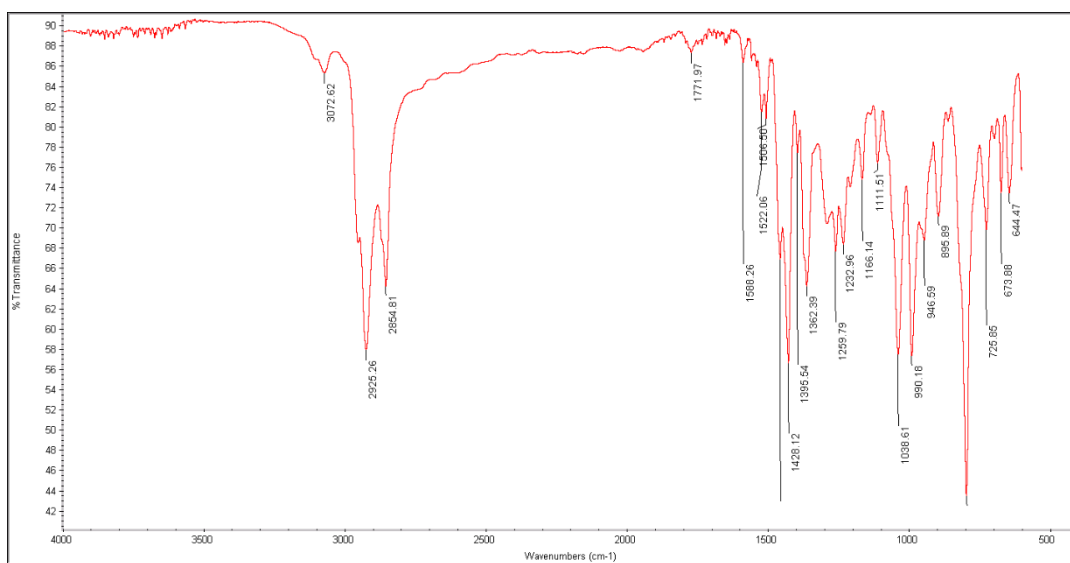


Figure A.55. IR-spectrum of **P4**

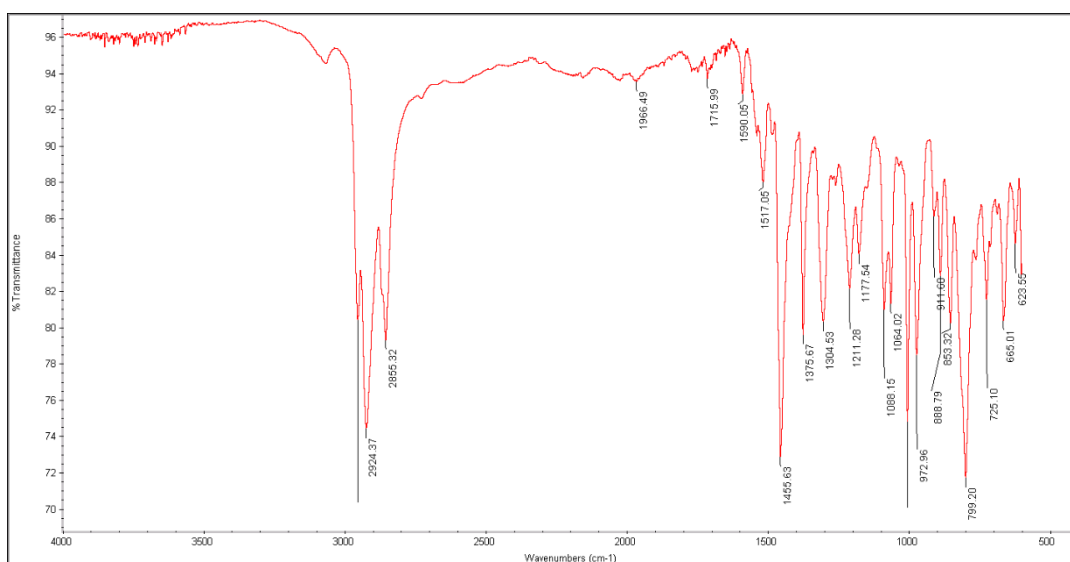


Figure A.56. IR-spectrum of **P5**

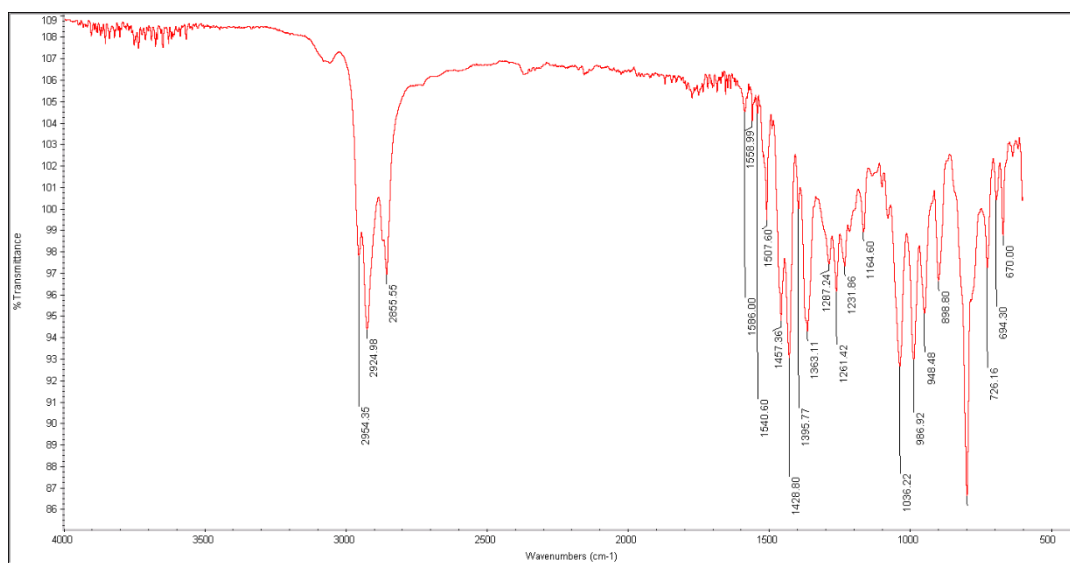


Figure A.57. IR-spectrum of P6

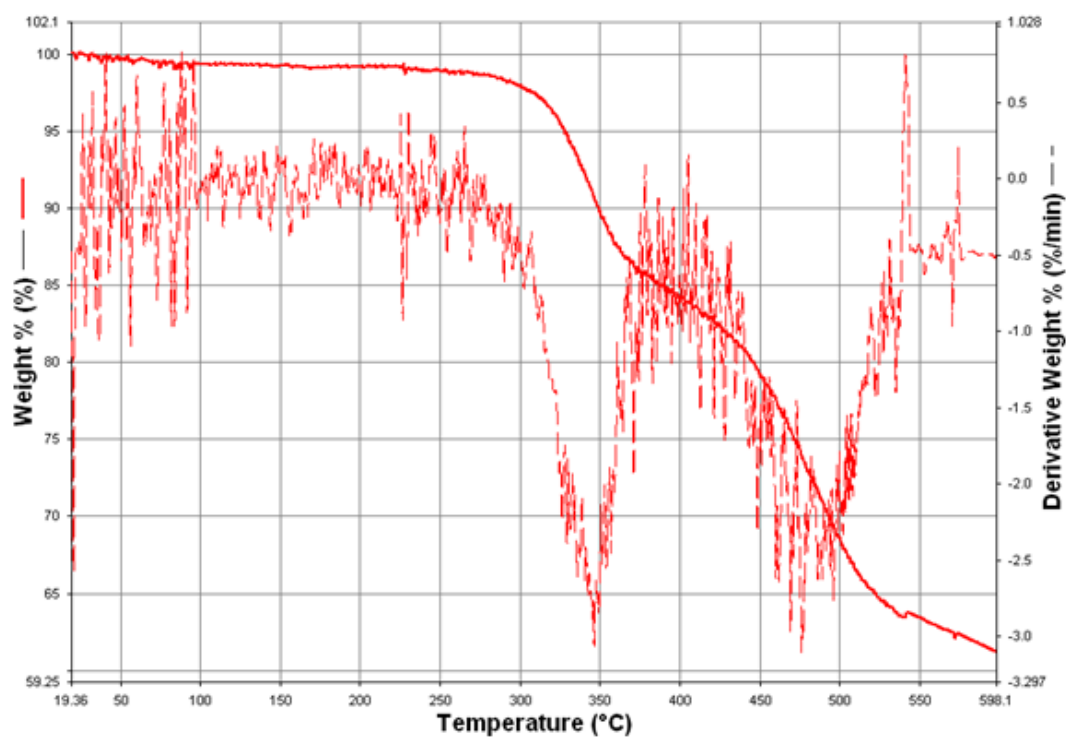


Figure A.58. Themogram of P1

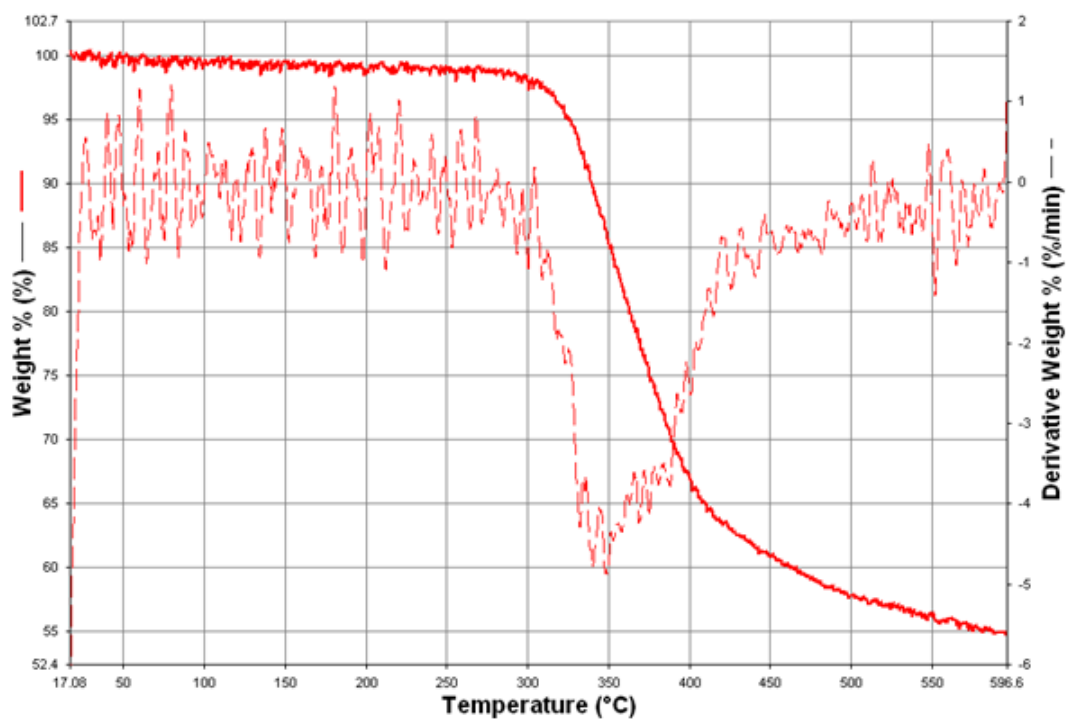


Figure A.59. Themogram of P2

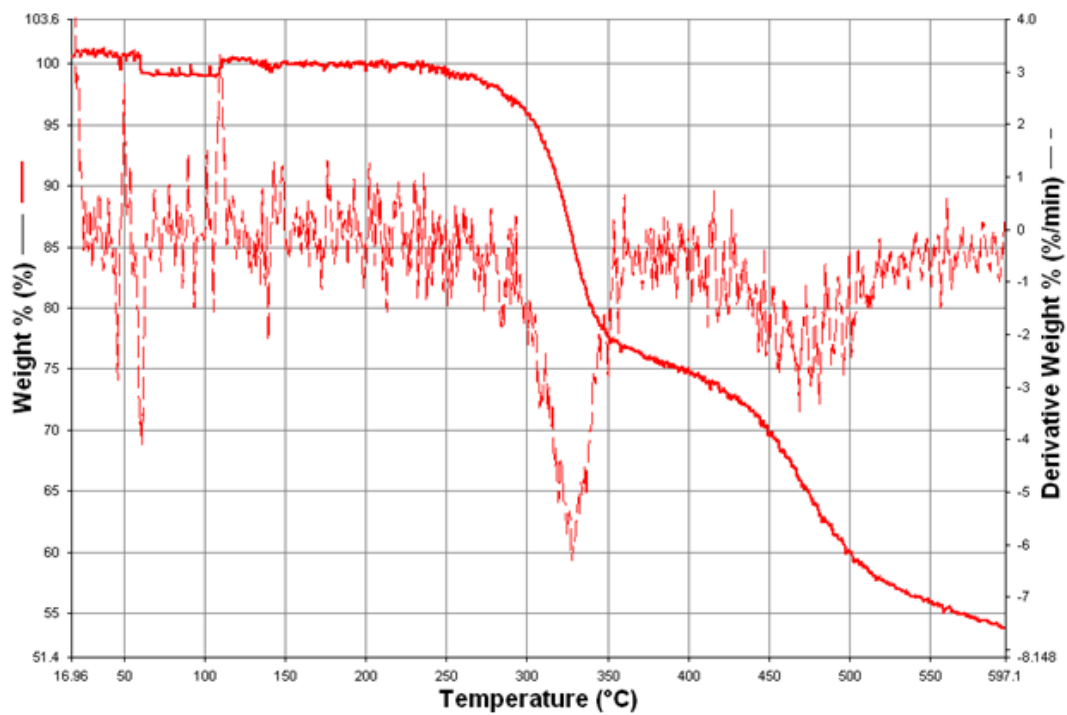


Figure A.60. Themogram of P3

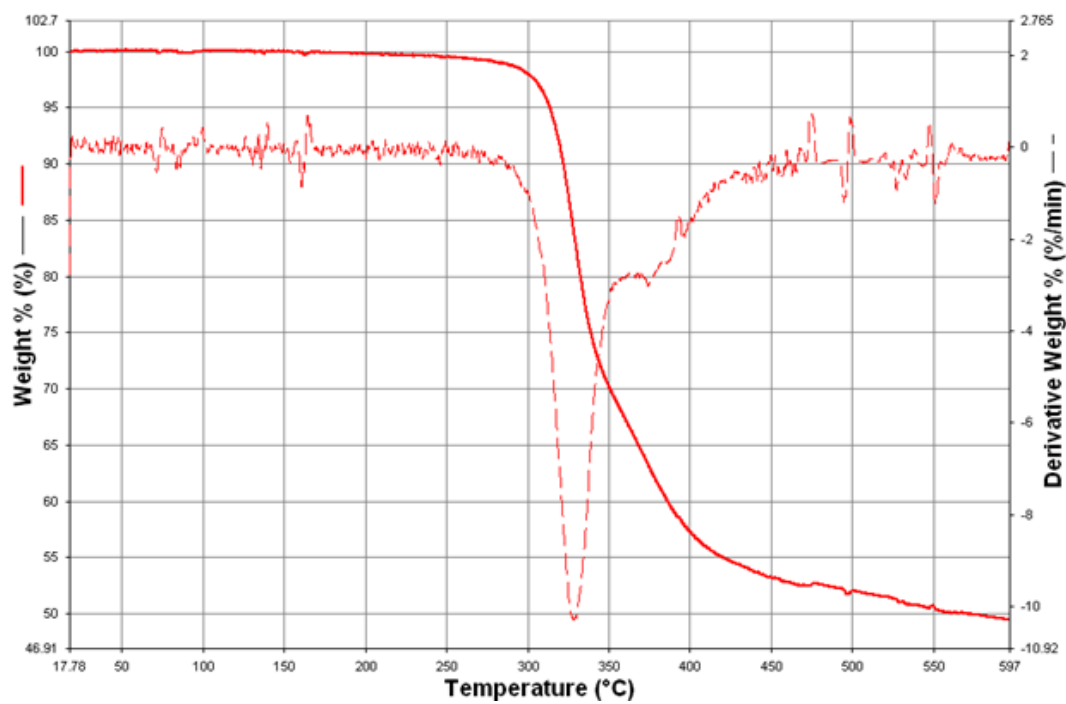


Figure A.61. Themogram of **P4**

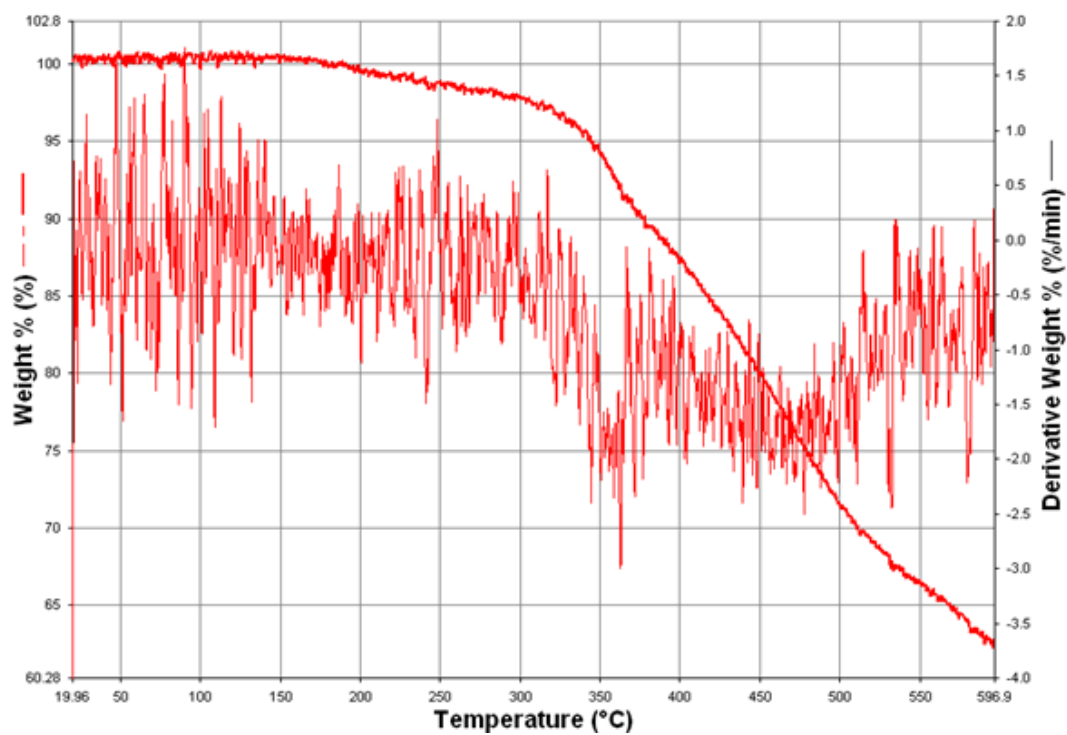


Figure A.62. Themogram of **P5**

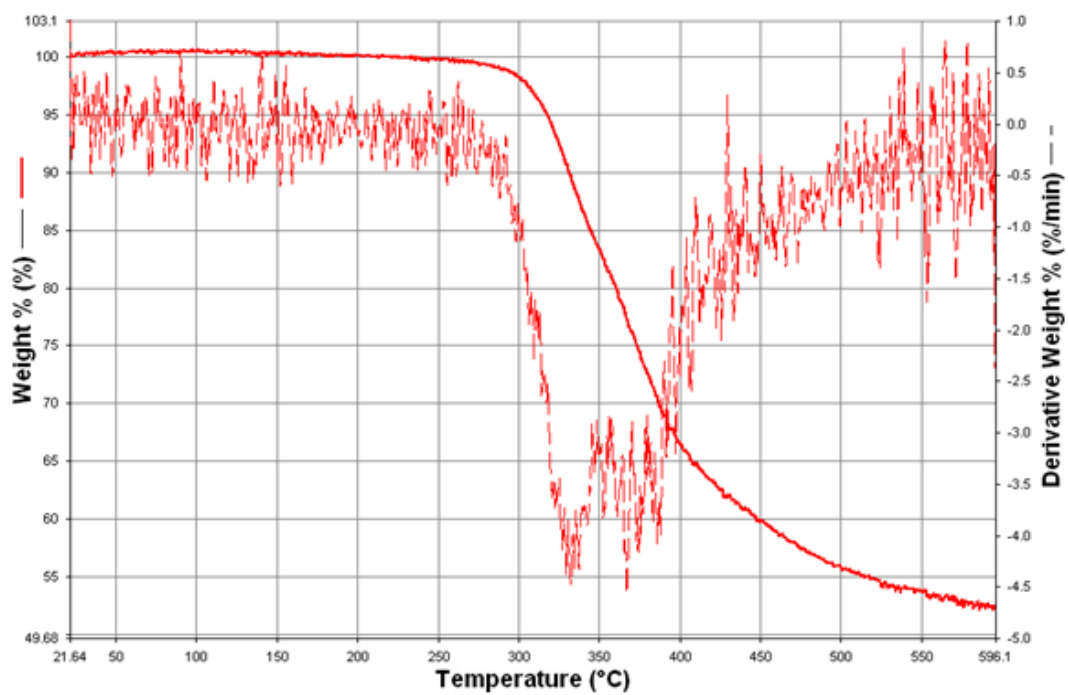


Figure A.63. Themogram of **P6**